CHARACTERIZATION AND TUNING OF QUANTUM EMITTERS IN HEXAGONAL BORON NITRIDE

Thesis by

Hamidreza Akbari

In Partial Fulfillment of the Requirements for

the Degree of

Doctor of Philosophy

CALIFORNIA INSTITUTE OF

TECHNOLOGY

Pasadena, California

2024

(Defended January 10, 2024)

Hamidreza Akbari
ORCID: 0000-0002-6073-3885

Acknowledgements

I am immensely grateful for the six remarkable years I have spent at the California Institute of Technology in the Applied Physics Department. This journey has been a transformative phase of my life, filled with learning, growth, and discovery. It is with a sense of deep appreciation that I acknowledge those who have made this journey not only possible but also a wonderful experience.

My profound thanks go to my advisor, Professor Harry Atwater. His invaluable guidance, unwavering support, and deep understanding have been pivotal in shaping my research and overall growth. Professor Atwater's mentorship has been a beacon of light through out my time at Caltech, guiding me through challenges and celebrating the milestones. His insights and wisdom have left an indelible mark on my academic and personal development.

The support of my family has been my backbone throughout this journey. I owe a heartfelt thank you to my wife, Sana, whose unwavering support during the hard times and the ups and downs has been a source of immense strength for me. To my family back in Iran, though distance kept us apart, your endless encouragement and belief in my career choices have always kept me motivated. Your virtual presence and emotional backing have been a constant source of comfort and motivation.

I extend my gratitude to the Atwater Research Group for providing an exceptionally collaborative and nurturing environment. Each member of this group has contributed significantly to my experience. I am particularly thankful to Souvik Biswas, whose

conversations about science and life enriched my understanding. Benji Vest deserves special mention for his mentorship during my first year. The scientific discussions with Pankaj Jha on quantum optics were always enlightening. I am also grateful to Anya Mitskovets, Yury Tokpanov, Ruzan Sokhuyan, Joeson Wong, and Melissa Li for the valuable chats and friendships that made my daily life at Caltech enjoyable and meaningful. My collaborations with Frank Yang, Wei-Hsiang Lin, Pin-Chieh Wu, Haley Bauser, and Yonghwi Kim have been integral to my research, providing valuable insights and contributing significantly to my work.

Lastly, my thanks go to the Caltech administration, especially the Applied Physics and Material Science Department, with a special mention of option manager Jennifer Blankenship. The support from the Office of International Student Affairs was crucial in navigating visa issues, and I am deeply appreciative of their assistance. The day-to-day help provided by the administrators of the Atwater group, including Jonathan Gross, Kam Flower, and Thomasine Murphy, was indispensable and greatly appreciated.

This journey at Caltech has been one of the most significant experiences of my life, and I am grateful to each and every one who has been a part of it. Thank you.

Abstract

Hexagonal boron nitride (h-BN) is a two-dimensional material hosting atomic defects that serve as single-photon emitters, attributed to its large bandgap. Its high stability at room temperature, substantial Debye-Waller factor, and integrability into 2D devices make h-BN a compelling choice for quantum applications involving single-photon emitters.

Initially, we investigate the properties of emitters in h-BN to comprehend the limitations of their spectral linewidth. This study includes examining the effects of the host crystal's growth method, the emitter's environment (the substrate), and temperature. As a result, we identify two primary broadening regimes: thermal broadening and spectral diffusion. Secondly, we address spectral diffusion, the predominant broadening mechanism at cryogenic temperatures, which depends on local electrical charges near the emitter. We propose a device structure comprising graphene - emitter h-BN - buffer h-BN - graphene, designed to apply a DC electric field and suppress spectral diffusion. This approach leads to a dramatic two orders of magnitude reduction in linewidth, achieving Fourier transform-limited linewidth.

Moreover, we explored the 3D dipole orientation and axial location of emitters within an h-BN crystal slab by coupling them to a phase change material. We discovered that the dipole orientation of some emitters is predominantly out-of-plane, and these emitters tend to exist close to the crystal's surfaces. This insight aids in the quest to determine the atomic structure of the emitters.

Finally, we examine the photon statistics of single-photon beams generated by h-BN emitters. We demonstrate that these beams exhibit sub-Poissonian statistics with both pulsed and continuous-wave excitation. Our findings reveal that excitation power can serve as a control to alter photon statistics, and we utilize this dependency to illustrate how photon

statistics influence the use of quantum emitters in quantum random number generation applications.

Published content and contributions

*indicates equal contribution.

- **H. Akbari**, W. H. Lin, B. Vest, P. K. Jha, and H. A. Atwater, *Temperature-Dependent Spectral Emission of Hexagonal Boron Nitride Quantum Emitters on Conductive and Dielectric Substrates*, Phys. Rev. Appl. **15**, 1 (2021). DOI: 10.1103/PhysRevApplied.15.014036.

  H.A. conceived the experiment with inputs from B.V. and H.A.A. H.A. prepared the samples with inputs from W.L. H.A. performed the optical characterization with input from B.V. H.A. performed the data analysis and prepared the manuscript.

- **H. Akbari**, S. Biswas, P. K. Jha, J. Wong, B. Vest, and H. A. Atwater, *Lifetime-Limited and Tunable Quantum Light Emission in h-BN via Electric Field Modulation*, Nano Lett. **22**, 7798 (2022). DOI: 10.1021/acs.nanolett.2c02163.

  H.A. conceived the experiment with inputs from H.A.A. H.A. helped S.B. with sample preparation. H.A. prepared the optical setup and performed the optical characterization. H.A. performed the data analysis and prepared the manuscript.

- P. K. Jha, **H. Akbari**, Y. Kim, S. Biswas, and H. A. Atwater, *Nanoscale Axial Position and Orientation Measurement of Hexagonal Boron Nitride Quantum Emitters Using a Tunable Nanophotonic Environment*, Nanotechnology **33**, (2022). DOI: 10.1088/1361-6528/ac2b71.

  P.K.J., H.A., Y.K., and H.A.A. conceived and developed the idea. H.A. performed the optical characterization of h-BN flakes and correlation measurements. P.K.J. and H.A. performed emission polarimetry of h-BN quantum emitters. All authors contributed to the data interpretation, presentation, and writing of the manuscript.

- **H. Akbari**, P. K. Jha, K. Malinowski, B. E. C. Koltenbah, H. A. Atwater, *Photon statistics analysis of h-BN quantum emitters with pulsed and continuous-wave excitation, In preparation*.

  H.A. and P.K.J. conceived the experiments with input from H.A.A. H.A. prepared the samples and performed the experiments with help from P.K.J. and K.M. H.A. and P.K.J. analyzed the data. B.E.C.K. performed the simulations. All authors contributed to the data interpretation, presentation, and writing of the manuscript.

This thesis contains excerpts from the aforementioned published/in preparation manuscripts.

Table of Contents

Acknowledgements iii

Abstract v

Published content and contributions vii

Table of Contents ix

List of illustrations xv

List of tables xxv

Chapter 1. Introduction 1

1.1 Hexagonal Boron Nitride 1

1.2 Single-photon sources 2

1.3 Applications of single-photon emitters 3

1.3.1 Quantum sensing and metrology 3

1.3.2 Random number generation 5

1.3.3 Quantum communication 5

1.3.4 Photonics quantum computing 6

1.4 Different types of single-photon emitters 8

1.4.1 Trapped atoms and ions 8

1.4.2 Defects in solids 10

1.4.3 Single dye molecules 11

1.4.4 Quantum dots 13

1.4.5 Attenuated lasers 14

1.4.6 Parametric down-conversion 16

1.5 Single-photon emitters in h-BN 17

1.6 Distinguishing features of h-BN quantum emitters 19

1.6.1 Stability at high temperatures 19

1.6.2 High Debye-Waller factor 20

1.6.3 Possibility of Fourier limited emission at room temperature 20

1.6.4 Integrability in devices 21

1.7 Indistinguishable single-photon emitters 22

1.7.1 Importance of indistinguishable single photons 22

1.7.2 Challenges in generating indistinguishable single photons 23

1.8 Scope of this thesis 23

Chapter 2. Linewidth broadening mechanisms in h-BN quantum emitters.....26

2.1 Abstract.....26

2.2 Introduction.....26

2.3 Low frequency spectral diffusion.....37

2.4 Summary and conclusion.....48

Chapter 3. 3-D dipole orientation and axial location of h-BN emitters.....49

3.1 Abstract.....49

3.2 Introduction.....49

3.3 Effect of LDOS on h-BN emitters.....52

3.4 VO_2 characterization, optical properties, and optimization.....55

3.5 h-BN emitter characterization.....62

3.6 LDOS engineering with phase change material.....67

3.7 Optical characterization of emitters.....70

3.8 Photophysics of *h-BN* quantum emitters.....77

3.9 Dipole orientation.....81

3.10 Experimental methods.....86

3.10.1 Optical characterization....86

3.10.2 Transfer of h-BN flake from VO_2 to SiO_2 substrate....87

3.11 Systematic errors and their effect on the results obtained....90

3.12 Summary and conclusions....91

Chapter 4. Stark tuning and linewidth control of h-BN emitters by electrostatic field....93

4.1 Abstract....93

4.2 Introduction....93

4.3 Effect of DC electric field on h-BN emitters....95

4.4 Study of linewidth with photoluminescence spectroscopy....99

4.5 Effect of temperature on the linewidth....105

4.6 Reproducibility of results....108

4.7 Experimental methods....110

4.7.1 Emitter preparation....110

4.7.2 Device fabrication....110

4.7.3 Optical characterization....111

4.8 Summary and conclusion....114

Chapter 5. Photon statistics of h-BN emitters 115

5.1 Abstract 115

5.2 Introduction 115

5.3 Pulsed Mandel Q 119

5.4 Comparison of h-BN quantum emitter and other light sources 120

5.5 Effect of temperature on Mandel Q 121

5.6 CW Mandel Q 123

5.7 Application of Mandel Q in Random Number Generation 126

5.8 Conclusion 129

Chapter 6. The path forward 130

6.1 Towards indistinguishable single-photon emitters in h-BN 130

6.1.1 Cross polarization filtering 131

6.1.2 Single-photon interferometry 136

6.1.3 Hong-Ou-Mandel experiment 137

6.2 High photon collection efficiency 138

6.3 Photon addition 139

6.3.1 The emitter requirements 139

6.3.2 Optical setup requirements 140

6.3.3 Detection scheme 141

Bibliography 142

Appendices 162

Appendix A: Efforts on TEM imaging of h-BN defects 162

Appendix B: Polarization and dipole orientation analysis 168

List of illustrations

Figure 1.1. h-BN crystal properties. (a) atomic structure of h-BN. This crystal consists of alternating boron and nitrogen atoms in a hexagonal lattice. (b) optical absorption measurements show the optical bandgap of h-BN to be at least 5.3 eV. (c) h-BN is widely used in 2-D devices either as electrically insulating layer or as an atomically smooth substrate. These pictures are taken from References [1–3]. 1

Figure 1.2. Schematic of HBT setup with a single-photon source and the result of $g^{(2)}$ measurement for a single-photon emitter. This picture is taken from Reference [4]. 3

Figure 1.3. h-BN quantum emitter. (a) Atomic defects in h-BN create electronic levels deeply located within the bandgap of h-BN. (b) h-BN emitters represent different emission energies and different spectral characteristics. (c) Atomic structure of h-BN emitters is yet to be determined, several candidates exist and further study is required to determine the exact atomic structure. These pictures are taken from References [2,19,20]. 18

Figure 1.4. Advantages of h-BN emitters. (a) On-chip device compatibility and tunability of the h-BN emitters. (b) Stability up to 800K. (c) possibility of Fourier limited linewidth up to room temperature. These pictures are taken from References [24,25,27]. 21

Figure 2.1. Schematic of substrate effect on spectral diffusion of single-photon emitters in h-BN. (a) h-BN emitter on insulating SiO2 substrate is prone to larger spectral diffusion due to charge traps in h-BN, SiO2, and their interface. (b) h-BN emitter on ITO substrate shows narrower linewidth as a result of fewer charge traps in h-BN, ITO, and their interface. 29

Figure 2.2. AFM measurement result of Bulk, CVD, and exfoliated flakes used for this study. 31

Figure 2.3. Schematic of homebuilt confocal microscope. 32

Figure 2.4. Quantum Emitters in bulk h-BN. (a) Microscope image and (b) photoluminescence map of a bulk h-BN crystal, the arrows show the position of two emitters understudy, scale bar corresponds to 5µm. (c) 4 K and (e) 300 K spectral of

zero phonon line of emitter1 solid line shows Lorentzian and the dashed line shows Gaussian fits (g) shows photon antibunching for emitter 1. (d), (f), and (h) show the same plot for emitter 2. 34

Figure 2.5. Polarimetry result of two emitters. Emitter 1 (left) shows some out of plane component and emitter 2 (right) shows almost completely in-plane dipole signature. 36

Figure 2.6. result of photon intensity autocorrelation measurement($g^{(2)}$). 36

Figure 2.7. Spectral resolution of the spectrometer. 37

Figure 2.8. Low-frequency spectral diffusion signature of emitters. (a) shows spectral diffusion of emitter#1 for 120 minutes, (b) shows the position of ZPL peak at each time and (c) is Fourier transform of (b). Panels (d),(e) and (f) show similar results for emitter #2. The shaded region in (b) and (e) specifies the FWHM of each emitter. 38

Figure 2.9. Correlation between average Amplitude of low frequency spectral diffusion and Inhomogeneous FWHM at 4K for 12 emitters in bulk h-BN..... 39

Figure 2.10. Temperature dependence of ZPL for emitters in bulk h-BN. Effect of temperature on lineshape for emitter 1 (a) and emitter 2 (b) from 4K to 300K. (c) shows linewidth against temperature for two emitters understudy linear fits for temperatures below and above 40K are shown, dashed lines are fits, and the dashed magenta line shows spectral resolution of the spectrometer used in this study. In (d) and (e) homogeneous and inhomogeneous components of linewidth extracted by Voigt fit are plotted as a function of temperature. The slope of power-law fit for homogeneous linewidth for emitter 1 is 1.05±0.21 and for emitter 2 is 1.54±0.38. The dotted grey line in (d) corresponds to T3 dependence of linewidth on temperature. 42

Figure 2.11. Effect of h-BN crystal and substrate type on inhomogeneous broadening. The left panel is a histogram of linewidths for emitters and the right panel is a scatter plot of linewidth against the ZPL wavelength (left axis) and histogram of the number of occurrences of a ZPL wavelength (right axis), for (a-b) CVD film on SiO2 substrate, (c-d) CVD film on ITO substrate, (e-f) exfoliated flake on SiO2 substrate, (g-h) exfoliated flake on ITO substrate, and (i-j) bulk h-BN crystal. The red dashed line shows the median of inhomogeneous linewidth for each sample. 44

Figure 2.12. Temperature dependence of zero phonon line full width at half maximum (FWHM) for various emitters in bulk h-BN, 5nm thick exfoliated h-BN on SiO2, 8nm thick exfoliated h-BN on ITO, 5nm thick CVD h-BN on SiO2, and 5nm thick CVD h-BN on ITO. The result illustrates the total FWHM for temperatures from 4K to 300K..... 47

Figure 3.1. Experimental schematic and distance-dependent modulation of relative decay rates. (a) Schematic of a quantum emitter in an atomically thin crystal of h-BN located within the thickness of a flake on a substrate which consists of a thin layer of vanadium dioxide (VO2) deposited on a sapphire crystal. (b) Relative decay rate $\beta=\gamma_{Insulating}/\gamma_{Metallic}$ as a function of distance d of a quantum emitter from the surface of VO2 when switched from the insulating to metallic state. The blue and red curves refer to quantum emitters oriented parallel and perpendicular to the surface, respectively, and the shaded regions corresponds to the typical quantum yield (QY) range of 0.6-1.0 of h-BN quantum emitters with zero-phonon line around 600 nm. For numerical simulation we considered the emission wavelength of 600 nm for the quantum emitter corresponding to the emitter A. The dashed line within the shaded region corresponds to QY = 0.79 as estimated from our experimental data. The refractive indices of the upper medium, h-BN, and that of sapphire were set to 1, 1.82, and 1.77, respectively. The refractive index of VO2 at 600 nm was set to 3.05 + 0.42i (insulating state) and 2.57 + 0.64i (metallic state) from our ellipsometry data. 53

Figure 3.2. Complex refractive index of VO2 in insulating and metallic phase. Extracted value of real (n) and imaginary (k) part of the complex refractive index of 40 nm thick layer of VO2 deposited on sapphire crystal at 30°C (blue) and 100°C (red) from our ellipsometry data..... 56

Figure 3.3. Temporal response of Peltier stage. Response of the Peltier stage as a function of time for ramp up and cooldown. Shaded region shows the ramp up region and the temperature is set to 100°C for 30 seconds and then the temperature decreases as a result of convection..... 57

Figure 3.4. Temperature-dependent reflectance spectra of a VO2 film during the heating cycle (dotted lines) and simulated reflectance curves of the film using the Bruggeman effective medium theory (solid lines). We observe gradual reflectance variations upon phase transition in VO2, where the volume fraction of metallic phase VO2 gradually evolves within the insulating phase VO2 host. 59

Figure 3.5. Optimization of VO_2 thickness. Figure of merit map (FOM) of a VO_2 film on a sapphire substrate obtained by full-wave simulations. The FOM indicates the reflectance contrasts between the insulating and metallic phases of VO_2. The results indicate that the largest optical contrasts at the zero-phonon lines when VO¬2 thickness is about 40 nm. 61

Figure 3.6. Surface characterization of VO2 film. Atomic force microscope measurement of VO2 film deposited on a sapphire substrate. This result shows that the film is uniformly grown, and the root-mean-square roughness is around 1.5 nm (2 μm × 2 μm) which is much smaller than thickness of the film which is 40 nm..... 62

Figure 3.7. Characterization of the exfoliated flake and spectra of h-BN quantum emitters. (a) Optical image of the mechanically exfoliated h-BN flake on VO2/Sapphire substrate. (b) Atomic force microscopy image of the flake shown in (a). The red dots on the traces (S-E) in (b) and (a) indicate the position of emitters A, and B with emission wavelength of 600 nm and 620 nm, respectively. (c) Line profiles along the region indicated by the trace in (b). At the location of the emitter A and B height of the flake is 310 nm and 340 nm, respectively. (d) Confocal photoluminescence (PL) map of the h-BN flake. The position of two single-photon emitters is marked by white circles. The edge of the flake in marked by white dashed line. The PL spectra of emitters A and B shown in (e) and (f), respectively, were obtained with VO2 in insulating state (blue) and metallic state (red). In these spectra ZPL and phonon sidebands (PSBs) are highlighted and the small peak around 692 nm corresponds to the emission from sapphire..... 63

Figure 3.8. Single-photon source characterization and axial location in h-BN flake. Plot of the second order photon correlation measurement, $g2(\tau)$ for the emitters A and B, in (a) and (b), respectively. The experimental data, blue squares for insulating VO2 phase and red stars for metallic VO2, were fitted to obtain the decay rates of the emitters. From the fit, we calculated the relative decay rates $\beta=\gamma_{Insulating}/\gamma_{Metallic}$ for the three emitters A and B as 0.818 ±0.108 and 0.800±0.124, respectively. For clarity, $g2(\tau)$ data obtained for metallic VO2 in (a), and (b) were shifted by 1 and 1.5, respectively. Plot of the relative decay rates β as a function of the distance (d) from the surface of VO2 and the polar angle (θ) for the emitters A and B are shown in (c) and (d), respectively. The dashed contour lines in (c) and (d) correspond to the experimental value of β obtained from (a) and (b), respectively, while the solid lines correspond to the error ($\pm\Delta\beta$) in the ratio..... 66

Figure 3.9. Radiative and non-radiative decay rates. Total (γ_{total}/γ_0), radiative (γ_r/γ_0), non-radiative (γ_{nr}/γ_0), rates of spontaneous emission of a quantum emitter as a function of distance from VO_2 surface for two dipole orientations, i.e., parallel (θ=90°) and perpendicular (θ=0°) to the surface. For numerical simulation we considered the emission wavelength λ_0 = 600 nm and the quantum yield QY = 0.79 corresponding to the emitter A. (a, b) Insulating phase of VO_2, (c, d) metallic phase of VO_2. Free-space decay rate $\gamma 0 = n\omega 03\rho 2/3\pi\varepsilon 0\hbar c3$, with c being the speed of light, n the refractive index of h-BN, ω_0 the atomic transition frequency, $\hbar$ the reduced Planck's constant, and ρ the amplitude of the dipole moment vector. The refractive indices of the upper medium, h-BN, and that of sapphire were set to 1, 1.82, and 1.77, respectively. The refractive index of VO2 at 600 nm was set to 3.05 + 0.42i (insulating phase) and 2.57 + 0.64i (metallic phase) from our ellipsometry data... 69

Figure 3.10. Experimental setup. Schematic of the homebuilt confocal microscope used to characterize h-BN quantum emitters, perform correlation measurements and emission polarimetry..... 71

Figure 3.11. Background subtraction for correlation measurements. Background subtraction for g^2 (τ) measurement of emitter B. (a) shows a PL map around the emitter, (b) shows a profile of the PL map shown by a dashed line in (a) with a Gaussian fit to it, and values for signal and background. (c) shows g^2 (τ) result before background subtraction and (d) shows g^2 (τ) result after background subtraction..... 72

Figure 3.12. Emitter C. In (a) we can see the position of this emitter in the PL map and spectra (b) and autocorrelation measurement result (c) at 30C and 100C. By comparing the ratio of decay rates to simulations at 570 nm, we extracted the axial position of this emitter as can be seen in (d)..... 74

Figure 3.13. Full-scale correlation data for the emitters A, B, C. Plot of the correlation measurement for Emitters A (a,b), Emitter B (c,d) and Emitter C (e,f) as a function of delay over the range of microseconds. The data in (a,c,e) and (b,d,f) are at room temperature and 100°C, respectively..... 77

Figure 3.14. Three-level system with corresponding decay and excitation rates..... 78

Figure 3.15. Plot of the decay rates $\gamma\_1,2$ as a function of the excitation power at the location of the emitter. We fitted the experimental data shown in (a, b) with Eqs. (S4, S5), respectively. (c) Plot of the intensity as a function of excitation power to determine the saturation count rates ($Isat$) and saturation power ($Psat$)..... 81

Figure 3.16. 3D-Orientation of h-BN quantum emitters and nanometric axial location. (a,b) Polar plots of the photoluminescence (PL) intensity of the emitter A and emitter B, respectively as a function of the emission polarization analysis angle (α). The PL data (solid spheres) were fitted to extract the azimuthal angle (φ) of the emitters and the degree of polarization (δ). From the fit, we deduce that for emitter A, φ=175.7°± 1.0°; δ= 0.461±0.023 and for emitter B, φ=109.9°± 2.9°; δ=0.473±0.070. (c, d) Calculated value of degree of polarization (δ) as a function of the polar angle (θ) of the emitters located at a distance of ~ 21 nm from the surface of VO2. The red dots in (c) and (d) corresponds to the experimental value of δ obtained from (a), and (b), respectively. The extracted value of the polar angle for emitter A and B are θ = 20.5° ±3.6° and θ = 21.2° ±4.5°, respectively. (e, f) Purple shaded region shows the range of the distance (d) and the polar angle (θ) of the emitters A and B, respectively, based on our experimental data and simulations..... 83

Figure 3.17. Emitter characterization. (a,b) Optical image of the flake on VO2/Sapphire substrate (before transfer) and SiO2/Si substrate (after transfer) respectively. The transferred flake is oriented at an angle Δφ=-12.6° with respect to its orientation on VO2/Sapphire substrate. (c) Confocal photoluminescence (PL) map of the flake on SiO2/Si substrate. Encircled (dashed white circle) highlights the region where emitters A and B are located. (d) PL spectra from the region highlighted in (c) shows the presence of emitters A and B which matched with the spectra obtained from the same location before transfer. The sharp line ~ 575 nm corresponds to Raman line of h-BN. (e,f) Polar plots of the PL intensity of the emitter A and emitter B, respectively as a function of the emission polarization analysis angle (α) on SiO2/Si substrate after the transfer. From the fit, we deduce that for emitter A, φ=164.6°± 3.0° and for emitter B, φ=94.4°± 4.0°..... 85

Figure 3.18. Transfer Process: Schematic of dry transfer process used to transfer our h-BN flake on VO2/Sapphire substrate to SiO2/Si substrate. 88

Figure 4.1. Effect of electric field on photoluminescence. (a) Schematic of the effect of electrostatic field on the single-photon emitter, top panels show the emitter located in the h-BN crystal with and without the electric field and the bottom panels show the emission spectra. Electric field locks charges located near the surface of h-BN at their place and reduces spectral diffusion. (b) Schematic of the device consisting of top and bottom graphene contacts, h-BN contatining emitter (shown as the red dot) and buffer h-BN. (c) PL map of the region containing the emitter. Each pixel is the integrated spectra from 570nm to 575nm. (d) Microscope image of the device flake edges are marked with dashed lines show location of top and bottom graphene and

buffer and emitter h-BN. (e) Normalized photoluminescence spectra of emitter ZPL at T=6.5K at voltages ranging form -10V to 10 V. D. PL map of the device, the white circle shows emitter's position. 97

Figure 4.2. FWHM and shift of ZPL peak extracted from PL measurement. 98

Figure 4.3. Integrated intensity of PL Vs Voltage applied to electrodes..... 99

Figure 4.4. Emitter characterization and near lifetime limited PLE. (a) Second order autocorrelation function for photon emission. The fit has a value of 0.14 at τ=0. (b) Time resolved photoluminescence of the emitter. The solid line corresponds to single exponential fit with time constant of 3.36ns this value corresponds to lifetime limited broadening of 47 MHz. The deviation of data from fit at t>10ns is a result of hitting the noise floor of the photodetector. (c) Normalized cryogenic (T=6.5K) PLE spectrum of the emitter at V=10V shows linewidth of 89 MHz. (d) At V=0V PLE spectra shows multiple peaks. The blue trace shows a fit with 10 Voigt functions with the same line shape as part (c), the black trace shows a single Voigt fit to assign a FWHM value equal to 8.5 GHz. 100

Figure 4.5. 9 PLE scans of the ZPL at V=0 and T=6.5K. The difference in the scans are originated by the difference in the local charges and their fluctuations..... 102

Figure 4.6. Effect of DC electric field on PLE. (a) PLE spectra of emitter at T=6.5 K for applied voltages ranging from -10V to 10V. (b) Full Width at Half Maximum (FWHM) of the peaks determined with a Voigt profile fit as a function of applied voltage, the minimum linewidth of 89MHz is achieved. (c) Measured peak position of the emitter relative to its peak position at 0V as a function of applied voltage. 104

Figure 4.7. Effect of temperature on PLE. (a) PLE traces of the emitter at V=10V for various temperatures. (b) Fitted value of FWHM of the peaks as a function of temperature with a power law fit (FWHM=ATn+C) with a best fit value of n=3.02±0.51, error bars correspond to 95% confidence interval of the fitted values, and the minimum linewidth is 89MHz at 6.5K..... 106

Figure 4.8. The left panel shows Voigt Fit (red) to the PLE data (black) traces for temperatures from 6.5K (bottom) to 120K (top), the right panel shows the fitted values for the Lorentzian and Gaussian FWHM (GHz) extracted from the Voigt fit. 108

Figure 4.9. Optical microscope image of the device, the white dashed line shows the active region of the device containing all 4 layers of top graphene, emitter h-BN, buffer h-BN and bottom graphene, the white circle shows the location of the emitter. b) PL traces of the emitter at voltages ranging from -30V to 30V, this emitter does not show a significant variation of PL linewidth and the linewidth is limited by the spectrometer resolution limit. c) PLE traces of the emitter at voltages ranging from -30V to 30V, d) effective FWHM of the PLE as a function of voltage with a minimum linewidth of 187 MHz at V=-20V. 109

Figure 4.10. AFM topography (left panel) of the device. Two traces (middle and right panel) correspond to lines shown as 1 and 2 on the topography map. These two traces are used to extract the thickness of buffer h-BN and emitter h-BN flakes. The total thickness of both h-BN together is 15.7+13.9=29.6 nm. 111

Figure 4.11. Polarimetry of the single-photon emitter performed at room temperature and without an electric field. 112

Figure 4.12. The resulst of ray tracing simulation to estimate the out of plane dipole component. 113

Figure 5.1. The schematic of Mandel Q analysis. (a) shows a stream of photon events with and without dividing into time bins, (b) is the histogram created by binning the photon stream, (c-d-e) histogram of Sub-Poissonian, Poissonian and super-Poissonian photon statistics. The value of Mandel Q depends on whether variance of the distribution is greater or smaller than the average. 116

Figure 5.2 Schematic of the experimental setup that collects photon incidents for photon statistics analysis. 118

Figure 5.3. Characteristics of h-BN emitter under pulsed excitation. (a) Microscope image of the h-BN flake containing the quantum emitter. (b) PL spectral of the emitter with a ZPL at 588nm and a sideband at 638nm. Inset shows CW $g^{(2)}$ function of this emitter. (c & g) Emission rate of the emitter as a function of time. The emitter exhibits two emissive states of on and off with 50kHz and 100kHz emission rate, respectively. (d) Result of pulsed coincidence measurement of the emitter. (e) TRPL measurement shows decay lifetime of 1.06 ns. (f) Polarization measurement shows a dipole emission pattern. (h) Single-pulse Mandel Q values for emitter in h-BN, coherent source, and thermal source. 120

Figure 5.4. Temperature dependence of h-BN emitter Mandel Q under pulsed excitation. (a) PL spectra of the emitter at 7K, (b) CW g(2) function of the emitter. (c) Result of PLE experiment on the zero phonon line of the emitter, the emission shows a narrow linewidth of 305MHz. (c) Mandel Q of emitter at different temperatures from 7K to 250K..... 122

Figure 5.5. CW Mandel Q of h-BN emitter. (a) Schematic of pulsed and CW Mandel Q. (i) Ideal case of pulsed excitation will result in one single-photon per pulse, (ii) considering losses, some of the single photons cannot be detected, (iii) pulse to pulse time scale imposes a natural time scale for binning and reporting the photon statistics. (iv) With CW excitation there is a stream of photons generated based on random excitation and decay of the emitter, (v) due to losses, some of the photons generated cannot be detected, (vi-vii) in the case of CW the freedom to choose the bin size can offset the effect of collection efficiency to some extent. (b) plot of CW Mandel Q as a function of time bin size. (c) Dependence of photon emission rate on pump power shows we are not operating near saturation. (d) CW Mandel Q Vs. pump power. This plot does not show a clear dependence of CW Mandel Q on pump power mainly due to blinking. (e) There is a strong correlation between Qmin and onset of coherence. 124

Figure 5.6. Effect of blinking on Mandel Q. (a) Emission rate of the emitter Vs. time shows clear on and off states. (b) dividing the data into on and off parts and calculating Mandel Q for each part. (c) Dependence of blinking on pump power. As the pump power changes the blinking pattern also changes and there is no clear correlation between pump power and the percentage of time that emitter is in the on state. However, for the maximum power (175μW) the emitter is mostly in the off state. (d) Dependence of minimum CW Mandel Q on pump power. As power increases, the Mandel Q decreases..... 125

Figure 5.7. Random number generation with h-BN emitters. (a) Protocol 1 of RNG. In this protocol we do not use Mandel Q and simply examine every photon detected. (b) Protocol 2 of RNG. In this protocol we bin the data with the time bin size that provides the minimum Q. (c) comparison of randomness of the bits generated by each protocol via NIST randomness test suite. Protocol 2 passes all tests while protocol 1 does not pass 4 tests. (d) Dependence of time required to generate a bit with protocol 2 with emitter pumped at various pump powers on the Mandel Q. The trend clearly shows at more negative Mandel Qs it takes less time to generate a random bit... 127

Figure 5.8. Histograms of random decimals generated binned from 0 to 106 for powers from 25-175μW..... 128

Figure 6.1. The cross polarization technique. (a) a schematic of the simplest possible the cross polarization setup with two polarizers and a 90:10 beam splitter. (b) ideal configuration of emitter dipole and excitation and detection polarizers. (c) result of rotating both excitation and detection polarizers, the color indicates the amount of output intensity..... 132

Figure 6.2. the result of experiment with blocking the beam with a mirror and rotating the QWP. Result shows a small change of polarization plane, and very small depolarization..... 133

Figure 6.3. The experiment with reflective gold sample instead of h-BN sample. the result shows that the microscope optic change the polarization to an elliptical state with a large S_3..... 134

Figure 6.4. Schematic and the result of the experiment with a full h-BN device. Result shows an elliptically polarized light similar to the gold sample however there is around 3% depolarization..... 135

Figure 6.5. The interferometry setup to measure emitter linewidth. (a) The schematic of our MZI. (b) The resulting fringes appearing on the screen..... 136

Figure 6.6. In HOM experiment if the two incoming photons are indistinguishable they interact and as a result both photons exit at the same channel..... 137

List of tables

Table 3.1. Spontaneous emission rates of emitters. Spontaneous decay rates of the emitters A, B, and C in the vicinity of VO_2 in insulating phase and metallic phase. The decay rates are estimated based on the fitting of $g_2(\tau)$ and subtracting the contribution of pump-dependent excitation rate. 75

Table 5.1. Comparison of single-photon emitter, laser, and thermal light Mandel Q 121

Chapter 1. Introduction

1.1 Hexagonal Boron Nitride

Hexagonal boron nitride (h-BN) is a van der Waals material, a type of 2-D material characterized by strong in-plane bonds and weak van der Waals interplane bonds. This structure allows atomic layers of these materials to be produced through mechanical exfoliation. The most well-known material in this category is graphene, which is composed of carbon atoms arranged in a hexagonal lattice. Similarly, h-BN is made up of boron and nitrogen atoms in a hexagonal lattice. Thanks to the robust B-N bond, h-BN remains very stable at room temperature. Its large bandgap (greater than 5.3 eV [1]) makes it useful as an atomically smooth, electrically neutral, and transparent substrate for other 2-D materials and devices.

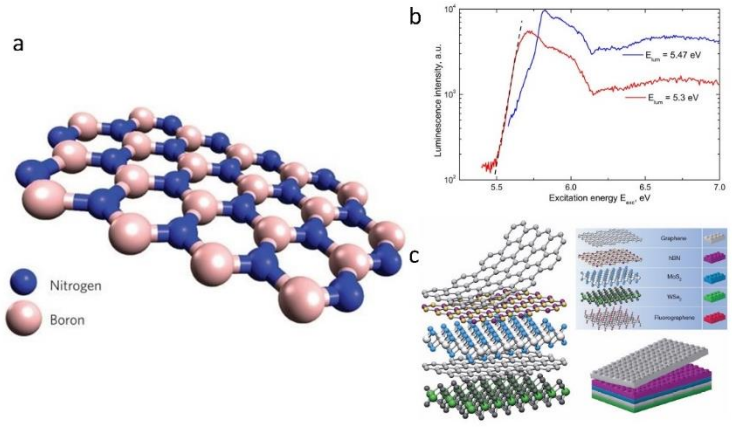

Figure 1.1. h-BN crystal properties. (a) atomic structure of h-BN. This crystal consists of alternating boron and nitrogen atoms in a hexagonal lattice. (b) optical absorption measurements show the optical bandgap of h-BN to be at least 5.3 eV. (c) h-BN is widely used in 2-D devices either as electrically insulating layer or as an atomically smooth substrate. These pictures are taken from References [1–3].

1.2 Single-photon sources

Single-photon sources (also known as single-photon emitters) are emissive species that can emit light one photon at a time. Most of the reliable single-photon sources exhibit electronic level structure of two-level systems and upon excitation to the excited state can decay to the ground state and release a single-photon [4]. However sometimes the electronic structure is more complex than a two-level system but effectively the emitter can be modeled as a two-level system. To test a source of light to identify whether it is a single-photon beam or another form of light (such as coherent light beam or a thermal light beam) a standard test can be performed on the light. In this test the beam of light is sent through a 50:50 beam splitter and a photo detector is located at each output of the beam splitter; this is known as Hanbury Brown-Twiss (HBT) configuration. Then the intensity correlation between the two detectors is measured and if the beam consists of single photons the correlation at zero time-delay should show the value zero, since the single photons cannot break down into Smaller energy packets and go through both channels, so they randomly go through either of the output channels. More precisely if the intensity correlation at various time delays is measured by introducing a delay line in either of channels the result would show a function that starts at zero at zero time-delay and gradually increases to one at large time delays. This behavior can be traced back to the exponential decay properties of the two-level system and it follows this functional form:

$$g^2(\tau) = 1 - b[(1+a)e^{-\frac{|\tau|}{T_1}} - ae^{-\frac{|\tau|}{T_2}}].$$

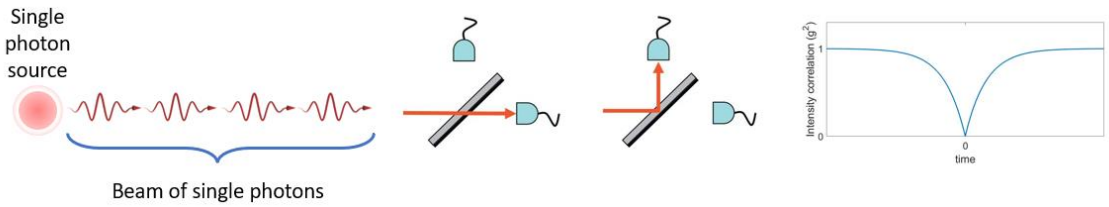

Figure 1.2. Schematic of HBT setup with a single-photon source and the result of $g^{(2)}$ measurement for a single-photon emitter. This picture is taken from Reference [4].

1.3 Applications of single-photon emitters

Single-photon emitters possess a unique set of properties that make them suitable for several applications. These properties include their high sensitivity to the local atomic environment, inherent quantum randomness, and, notably, the ability to generate non-cloneable single photons in a known quantum state. Below I explain some of the applications of single-photon sources.

1.3.1 Quantum sensing and metrology

The application of single-photon emitters in the field of quantum sensing shows a significant advancement in the field of precision measurements. Quantum sensing exploits the unique properties of quantum systems — such as superposition and entanglement — to measure physical quantities with unprecedented accuracy and sensitivity. Single-photon emitters are particularly valuable in this domain due to their ability to generate and manipulate individual photons, which are fundamental to quantum measurement techniques [5].

In quantum sensing, single-photon emitters are used to create states of light that are highly sensitive to external influences, such as magnetic fields, electric fields, temperature, or

pressure. For example, in the case of magnetic field sensing, single-photon emitters can interact with the magnetic field, resulting in changes to their properties (like polarization or phase). By detecting these changes, very precise measurements of the magnetic field can be made at an atomic scale. This technique is especially useful in fields where high sensitivity is required, such as in medical imaging (e.g., MRI), geological surveying, and navigation systems [5].

Another application of single-photon emitters in quantum sensing is in the area of photonic-based quantum metrology. This involves using quantum states of light for making highly accurate and precise measurements. For example, in interferometry, single photons can be used to measure changes in distance or displacement at scales much smaller than what is possible with classical light sources. This method has potential applications in areas like gravitational wave detection, where detecting minuscule perturbations in spacetime is essential [5].

Moreover, the quantum nature of single photons allows for the development of sensors that can overcome the limits imposed by classical physics. For instance, in classical sensing, the precision of measurements is often limited by noise. However, in quantum sensing, techniques such as entanglement and squeezing can be used to reduce or even eliminate this noise, leading to more precise measurements. This is particularly beneficial when environmental noise is a major challenge [5].

In summary, the application of single-photon emitters in quantum sensing opens up new frontiers in measurement science. By leveraging the quantum properties of single photons, it is possible to develop sensors with unprecedented sensitivity and precision. These advancements have far-reaching implications across various fields, from medical diagnostics

to fundamental physics research, showcasing the transformative potential of quantum technologies in enhancing our measurement capabilities.

1.3.2 Random number generation

In quantum random number generation (QRNG), the inherent randomness of quantum mechanical processes, like the emission and detection of single photons, is harnessed. One approach is to use momentum-polarization entangled single-photon states, which can significantly enhance the security of the generated random numbers. This method takes advantage of quantum entanglement. By utilizing entangled photons, QRNG systems can achieve a higher level of security, making them suitable for cryptographic applications and other scientific fields that require high security [6].

However, challenges exist in the practical implementation of QRNG using single-photon emitters, primarily due to limitations in detection speed. One approach to overcome this, is using the time of arrival of photons as a variable. The randomness in the time of arrival of each photon, due to the stochastic nature of quantum processes, can be used to generate random numbers. This method involves subdividing the time period into several bins, allowing the generation of multiple bits from the arrival time of a single photon. This approach improves the speed and maintains the unpredictability and security of the random numbers generated [6].

1.3.3 Quantum communication

Another application of single-photon emitters is secure quantum communication and more specifically quantum key distribution (QKD). QKD is a method for secure communication that uses quantum mechanics to ensure the confidentiality of exchanged keys. These keys are used to encrypt and decrypt messages. The core advantage of QKD lies in its ability to

detect any attempt at eavesdropping, a feature enabled by the fundamental principles of quantum mechanics such as no-cloning theorem [7,8].

The role of single-photon emitters in QKD is crucial. These emitters generate photons individually, which can then be used as quantum bits, or qubits, for transmitting information. In QKD systems like the Bennett-Brassard 1984 (BB84) protocol, single photons are prepared in different quantum states, representing the key's bits. These photons are then sent to the receiver through a quantum channel, typically an optical fiber or through free space. The security of QKD arises from the fact that any attempt to intercept and measure these quantum states by an eavesdropper will inevitably alter the states due to the no-cloning theorem in quantum mechanics. This alteration can be detected by the communicating parties [7].

The efficiency and security of QKD systems are heavily dependent on the properties of the single-photon emitters used. Ideal single-photon emitters should have a high brightness (rate of photon generation), low multi-photon emission probability, and high stability. These properties ensure the integrity of the quantum key. Furthermore, if the single-photon source can produce indistinguishable single photons, it enables the implementation of more advanced forms of QKD, such as entanglement-based protocols, which offer even higher security by using pairs of entangled photons. In these systems, measurements performed on one photon immediately affect its entangled partner, regardless of the distance between them, making it even more challenging for eavesdroppers to intercept the key without detection [7].

1.3.4 Photonics quantum computing

Single-photon emitters are an integral part of the photonics-based quantum computing technology. In photonics quantum computing, single photons are used as quantum bits

(qubits), the basic units of quantum information, offering unique advantages in terms of speed, scalability, and security [9]. It is worth noting that the field of quantum computing consists of multiple technologies such as superconducting circuits, cold atoms and ions and photonics-based quantum computers. All of these platforms present advantages and disadvantages and here our focus is mainly on photonics-based technologies.

The application of single-photon emitters in photonics quantum computing is primarily centered around their ability to generate photons individually and deterministically. This is essential for creating and manipulating qubits in a controlled manner. In quantum computing, the state of a qubit can be in a superposition of 0 and 1, unlike classical bits that are either 0 or 1. Single photons, with their quantum properties like superposition and entanglement, are ideal for representing these qubits. By controlling the polarization, phase, or path of these photons, photonics quantum computers can perform certain complex calculations at a speed that is unattainable by classical computers [9].

Furthermore, single-photon emitters contribute to the scalability of quantum computing. For a quantum computer to be practically useful, it needs to handle a large number of qubits. Single-photon emitters enable the generation of large numbers of indistinguishable photons, which can be entangled and manipulated for parallel processing. This is particularly significant in the context of quantum algorithms, where the ability to perform many calculations simultaneously (quantum parallelism) can drastically reduce the time required for complex computations, such as factoring large numbers or searching large databases [10].

The stability and coherence time of the photons emitted are also crucial. High-quality single-photon emitters ensure that the all the generated photons are indistinguishable, allowing for the execution of multiple quantum gates and operations coherently. This is essential for the

realization of quantum error correction and fault-tolerant quantum computing, which are necessary for building a reliable quantum computer [9].

1.4 Different types of single-photon emitters

There are multiple types of single photon emitters competing for several applications. Each platform has certain advantages and disadvantages that makes them useful for certain applications. In this section we go through main types of single emitters and discuss advantages and disadvantages of each platform.

1.4.1 Trapped atoms and ions

Trapped atoms and ions have emerged as prominent sources of single-photon sources in various quantum technology applications. These systems involve confining individual atoms or ions in electromagnetic fields, allowing for precise control over their quantum states. This control is essential for generating single photons with specific characteristics, such as frequency, polarization, and phase [11].

1.4.1.1 Advantages

Well-defined energy levels: One of the primary advantages of using trapped atoms and ions is their discrete and well-defined energy levels. This allows for the generation of photons with very specific wavelengths and properties, which is crucial for applications in quantum communication and quantum computing [11].

High-quality photon emission: Trapped atoms and ions can produce single photons with high purity and indistinguishability. This is particularly important in quantum computing, where the quality of qubits directly impacts the system's computational power and error rates [11].

Control over quantum states: The ability to precisely manipulate the quantum states of trapped atoms and ions enables complex quantum operations. This level of control is beneficial for creating entangled states and implementing quantum gates [11].

Isolation from environmental disturbances: Trapped atoms and ions are relatively well isolated from environmental noise and disturbances, which helps in maintaining the coherence of quantum states over longer periods. This isolation is crucial for achieving high-fidelity operations in quantum computing and precise measurements in quantum sensing [11].

1.4.1.2 Disadvantages

Complex setup and maintenance: Setting up and maintaining the trapping apparatus for atoms and ions can be complex and costly. This includes the need for ultra-high vacuum conditions, sophisticated laser cooling techniques, and precise electromagnetic field controls [11].

Scalability challenges: Scaling trapped atom and ion systems to larger numbers of qubits, which is essential for practical quantum computing, remains a significant challenge. Managing and controlling interactions between a large number of trapped particles is not straightforward [11].

Speed limitations: The operational speed of quantum systems based on trapped atoms and ions is generally slower compared to other quantum technologies, like superconducting qubits. This is due in part to the time required for cooling, trapping, and manipulating the atoms or ions [11].

1.4.2 Defects in solids

Atomic defects in solids, notably in materials like diamond, silicon carbide and h-BN, have garnered significant attention as sources of single-photon emission. These defects, often referred to as color centers, are imperfections in the crystal lattice where one or more atoms are missing or replaced by different atoms. The most well-known examples are the Nitrogen-Vacancy (NV) centers and silicon-vacancy (SiV) centers in diamond [12–14].

1.4.2.1 Advantages

Stable and bright photon sources: Atomic defects in diamond and silicon carbide are stable sources of single photons. They can emit bright and consistent light at room temperature, which is a significant advantage for practical applications [13].

Operational at room temperature: Unlike many other quantum systems that require extremely low temperatures, these atomic defects can efficiently emit photons at room temperature. This greatly simplifies the experimental setup and reduces the operational costs [12].

Long coherence times: NV centers in diamond, in particular, have long coherence times, meaning the quantum state of the emitted photons remains intact over comparatively long durations. This is crucial for quantum computing and quantum communication applications, where maintaining quantum coherence is essential [12].

Versatility in quantum applications: These atomic defects can be used in a wide range of quantum applications, including quantum computing, quantum cryptography, and quantum sensing. Their ability to be integrated into solid-state devices makes them particularly appealing for developing practical quantum technologies [14].

1.4.2.2 Disadvantages

Fabrication challenges: Creating these defects with precision can be challenging. It requires sophisticated techniques to introduce and position these atomic defects accurately within the crystal lattice [14].

Variability and quality control: There can be significant variability in the properties of the emitted photons from different defects, even within the same material. Achieving uniformity and high quality in the photon emission across multiple sites is a complex task [12].

Integration with photonic circuits: While these materials are promising for quantum applications, integrating them with existing photonic and electronic systems poses significant challenges. This integration is crucial for building scalable quantum communication networks and computing systems [14].

Sensitivity to environmental interference: Despite their stability, these defect centers can still be sensitive to environmental factors like temperature fluctuations and electromagnetic fields. This effect can manifest itself as spectral diffusion, which can affect their performance [13].

1.4.3 Single dye molecules

Organic dye molecules as single-photon emitters are attracting attention for their ease of fabrication and tunability. In these emitters the transition happens between the molecular orbitals known as highest occupied molecular orbital (HOMO) and lowest unoccupied molecular orbital (LUMO). Specific examples of these molecules include Rhodamine,

Fluorescein, and Perylene derivatives, which are known for their intense and tunable fluorescence. [15,16].

1.4.3.1 Advantages

Tunable emission properties: With a broad range of emission wavelengths, organic dyes like Rhodamine and Fluorescein can be chemically altered to customize photon emission for various applications [15].

High brightness and efficiency: These molecules often exhibit high quantum yields, translating to efficient photon emission. This is particularly beneficial for creating potent single-photon sources [15].

Compatibility with various host materials: Organic dyes can be embedded in diverse host materials, such as polymers or crystals, offering flexibility in photonic device design and fabrication [15].

Ease of synthesis and modification: Molecules like Perylene derivatives are relatively simple to synthesize and can be chemically modified to enhance their photophysical properties or integration into different devices [15].

1.4.3.2 Disadvantages

Photostability issues: Organic dyes are prone to photobleaching, which can degrade the molecules and diminish their photon emission capability over time [15].

Environmental sensitivity: These dyes are highly sensitive to environmental conditions like temperature, oxygen, and humidity, impacting their performance as single-photon emitters. Blinking is also a common feature of these emitters which manifests itself as rapid change

in the brightness of the emitter due to change in the electrical environment of the emitter [15].

Difficulty in isolating single molecules: Isolating individual dye molecules for single-photon emission can be technically challenging, requiring sophisticated techniques [16].

1.4.4 Quantum dots

Quantum dots (QDs) or artificial atoms are another popular platform of single-photon emitters. These nanoscale semiconductor crystals have unique electronic properties due to quantum confinement, allowing them to emit photons individually when excited. [17,18].

1.4.4.1 Advantages

Size-tunable emission: The emission wavelength of quantum dots can be finely tuned by adjusting their size. Smaller dots emit higher energy (bluer) photons, while larger dots emit lower energy (redder) photons. This tunability is invaluable for applications requiring specific wavelengths [17].

High quantum efficiency: Quantum dots typically exhibit high quantum yields, meaning they are very efficient at converting absorbed energy into emitted light. This efficiency is crucial for creating bright and reliable single-photon sources [17,18].

Solid-state stability: Unlike organic dyes, quantum dots are more stable and less prone to photobleaching. This stability makes them suitable for long-term applications in various environments [18].

Integration with electronics: Since quantum dots are built with semiconductors, they easily can be integrated into existing electronic and photonic devices, offering potential for creating on-chip quantum systems and devices [17].

1.4.4.2 Disadvantages

Blinking: A significant challenge with quantum dots is their tendency to exhibit "blinking" — spontaneous fluctuations in their emission intensity. This blinking can be problematic for applications requiring a consistent photon stream [18].

Toxicity and environmental concerns: Many quantum dots are made from materials like cadmium or lead, which are toxic and pose environmental and health risks. Safe handling and disposal of these materials are critical concerns [18].

Inhomogeneous broadening: Due to variations in size and shape, a population of quantum dots can exhibit inhomogeneous broadening, where the emitted photons have a range of wavelengths instead of a single, precise wavelength [17].

Fabrication complexity: Producing quantum dots with uniform size and properties is technically challenging and often requires sophisticated and expensive fabrication techniques [17].

1.4.5 Attenuated lasers

Attenuated laser beams as single-photon emitters have been used for many classic experiments in the field of quantum optics, especially in the context of quantum communication and quantum cryptography. An attenuated laser beam is essentially a

standard laser light that has been reduced in intensity to a level where, on average, one photon is emitted at a time. This approach offers a practical way to generate single photons [4].

1.4.5.1 Advantages

Ease of generation: Unlike specialized single-photon sources like quantum dots or NV centers, attenuated laser beams can be generated using conventional laser technology combined with simple attenuation methods. This makes them relatively easy and cost-effective to produce [4].

High repetition rates: Lasers can emit photons at very high rates, which means that when attenuated, they can provide single photons at high repetition rates. This is beneficial for applications like QKD, where faster photon generation can lead to higher data transmission rates.

Wavelength versatility: Lasers are available across a broad range of wavelengths, allowing for flexibility in choosing the appropriate wavelength for specific quantum applications [4].

Technological maturity: Laser technology is well-established and widely available, providing a robust and reliable platform for generating single photons.

1.4.5.2 Disadvantages

Poisson photon distribution: The emission of photons from an attenuated laser follows a Poisson distribution, meaning there is always a non-zero probability of emitting multiple photons at a time. This can be a significant drawback in quantum cryptography, as it opens a vulnerability for eavesdropping [4].

Lack of true single-photon purity: Unlike true single-photon sources, attenuated lasers cannot guarantee the emission of one and only one photon at a time. This can limit their usefulness in certain quantum computing and quantum communication protocols [4].

1.4.6 Parametric down-conversion

Parametric down-conversion (PDC) as a single-photon source is a widely-used method in quantum optics and quantum information science. This process involves using a nonlinear optical crystal to split incoming photons from a laser beam into pairs of lower-energy photons, known as signal and idler photons. When one photon of a pair is detected, the presence of its counterpart is inferred, effectively creating a single-photon source [4].

1.4.6.1 Advantages

Photon pair generation: PDC is unique in its ability to produce correlated photon pairs. This property is crucial for quantum entanglement experiments and applications in quantum communication, where entangled photon pairs play a central role.

Wavelength versatility: The wavelengths of the generated photons can be tuned by choosing appropriate crystals and pump laser wavelengths. This tunability allows for flexibility in designing experiments and applications.

High single-photon purity: The photons produced through PDC are generally of high purity and exhibit excellent quantum properties, making them suitable for precise quantum optics experiments.

1.4.6.2 Disadvantages

Inefficiency: The process of generating photon pairs in PDC is probabilistic and typically has low efficiency. A large number of pump photons are required to produce a relatively small number of photon pairs [4].

Random pair production: Photon pairs are produced randomly, not on demand. This randomness can be a significant drawback for applications requiring synchronized or timed single-photon emission. However existence of idler photons can prepare the user for the single-photon the generation time is still unknown.

Requirement for post-selection: In many cases, the presence of one photon in a pair is used to infer the existence of the other. This often requires post-selection techniques, which can be inefficient and may discard a large number of photons [4].

1.5 Single-photon emitters in h-BN

Single-photon emitters in h-BN represent a rapidly evolving and significant area of research in quantum photonics. These emitters, discovered in 2016 [2], have sparked considerable interest due to their potential applications in nanophotonics and other quantum technologies. The exploration into h-BN as a host for these emitters aligns with the broader trend of investigating two-dimensional (2D) materials for photon-based quantum information technologies. Compared to defects in bulk crystals, such as those found in diamond and silicon carbide, defects in 2D materials like h-BN promise easier addressability and control.

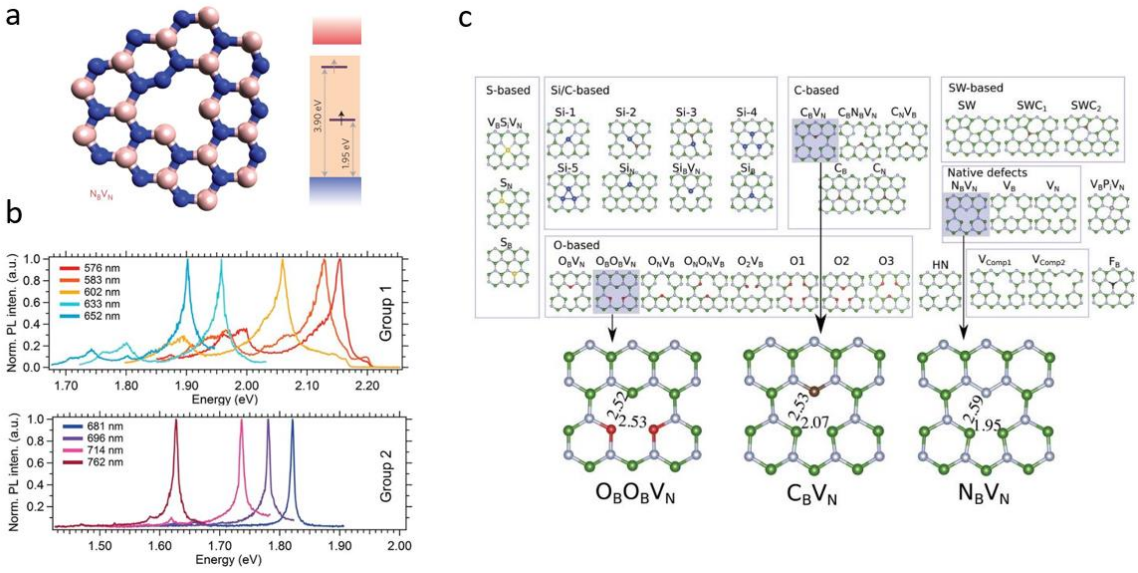

Figure 1.3. h-BN quantum emitter. (a) Atomic defects in h-BN create electronic levels deeply located within the bandgap of h-BN. (b) h-BN emitters represent different emission energies and different spectral characteristics. (c) Atomic structure of h-BN emitters is yet to be determined, several candidates exist and further study is required to determine the exact atomic structure. These pictures are taken from References [2,19,20].

One of the primary challenges in this field is the incomplete understanding of the atomic structure of these emitters [20,21]. While numerous studies have focused on the excited states and radiative properties of over 20 native defects and carbon or oxygen impurities in h-BN, a comprehensive understanding remains elusive. These investigations reveal a wide variability across quantum emitters, with significant differences in exciton energies and radiative lifetimes for different defect structures [20,22,23].

This variability underscores the complexity of the emitters' atomic structure. Although density functional theory (DFT) calculations have provided valuable insights into formation energy, symmetry, and the electronic structure of single-photon emission (SPE) defects, they fall short in addressing the excited states and radiative processes responsible for light

emission. Optical transitions at defects in h-BN, dominated by excitonic effects, require advanced first-principles calculations beyond DFT's scope [20,22].

The quest to fully understand and harness these emitters is ongoing, with researchers employing various computational and experimental approaches to elucidate the atomic and electronic structures of these emitters. This research is not just academic; it has practical implications for the development of advanced quantum technologies, potentially revolutionizing fields like secure communication, quantum computing, and high-resolution sensing. The journey to unravel the mysteries of h-BN's single-photon emitters illustrates the dynamic and exploratory nature of research at the intersection of quantum physics and materials science [19].

1.6 Distinguishing features of h-BN quantum emitters

Single-photon emitters in h-BN offer several advantages over other types of single-photon emitters, making them particularly intriguing for research. In this section, we will elaborate on some of these advantages.

1.6.1 Stability at high temperatures

Few single-photon emitters display bright emission at room temperature, as the majority of quantum emitters require cryogenic temperatures to achieve satisfactory brightness. However, h-BN emitters stand out by not only demonstrating relatively high brightness and narrow linewidth at room temperature but also maintaining stability up to 800K. The high-temperature stability of h-BN emitters offers a significant advantage for applications that operate under high temperatures and rough conditions. This property not only broadens the range of potential applications but also helps reduce the overhead costs associated with

maintaining the necessary operational environment for less temperature-stable emitters [19,24].

1.6.2 High Debye-Waller factor

The Debye-Waller factor is a critical parameter in evaluating the performance of quantum emitters. This factor measures the intensity ratio of photon emission through the zero-phonon line (ZPL) compared to the total photon emission, including phonon sidebands.

The Debye-Waller factor in h-BN quantum emitters has been observed to be greater than 80% [2], a value that is comparable to the brightest single-photon emitters (SPEs). This significant factor underscores the efficiency of these emitters in producing high-quality single photons. The high Debye-Waller factor is beneficial as it minimizes the interaction with phonons, thereby reducing the risks of decoherence and energy loss, which are critical for maintaining the integrity of quantum information transmitted through these photons [4].

The exceptional Debye-Waller factor of h-BN quantum emitters, combined with their ability to operate efficiently at room temperature and exhibit linearly polarized emission, makes them an attractive choice for a variety of quantum technologies. These include quantum cryptography, where the spectral purity and stability of the photons are crucial for secure quantum key distribution, and quantum computing, where the coherence and fidelity of quantum states are essential for effective quantum information processing [19].

1.6.3 Possibility of Fourier limited emission at room temperature

Research indicates the potential for Fourier-limited emission from h-BN emitters at room temperature. This characteristic is attributed to the decoupling of the defect from the host lattice vibrations, a phenomenon that requires further exploration. Such potential could result

in indistinguishable single-photon sources at room temperature, potentially paving the way for low-cost quantum computers operable at room temperature [25,26].

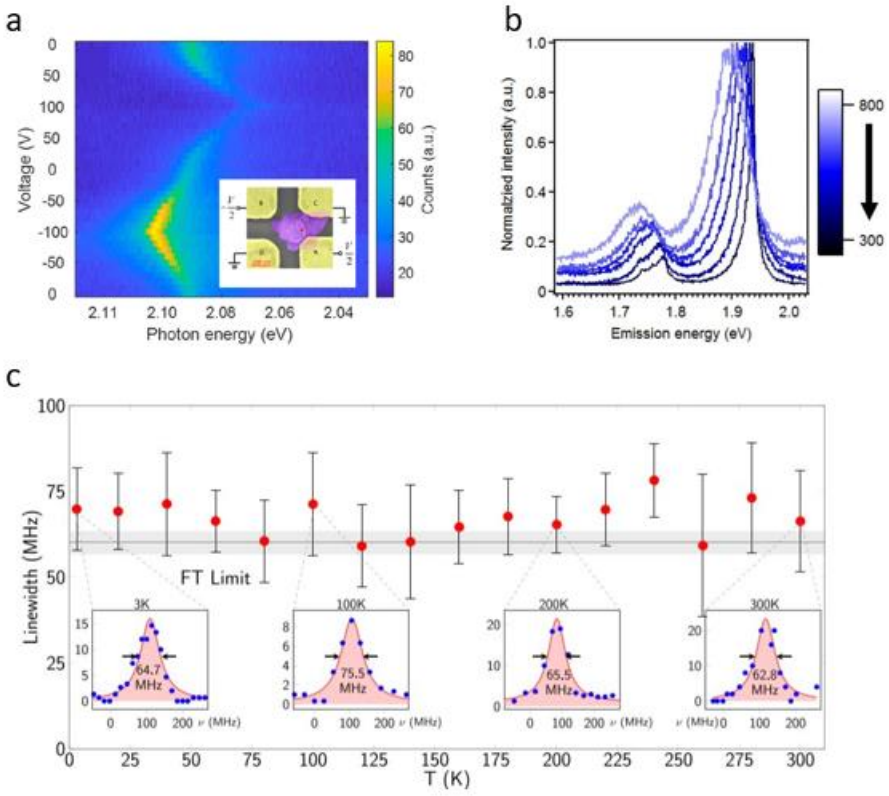

Figure 1.4. Advantages of h-BN emitters. (a) On-chip device compatibility and tunability of the h-BN emitters. (b) Stability up to 800K. (c) possibility of Fourier limited linewidth up to room temperature. These pictures are taken from References [24,25,27].

1.6.4 Integrability in devices

The two-dimensional nature of h-BN crystal makes it suitable for integration into on-chip devices. The emerging field of two-dimensional materials has explored various materials

with diverse electrical and optical properties that can be combined with h-BN to create customized 2D devices for managing different aspects of outgoing single photons.

One straightforward example involves introducing an electrostatic field by placing h-BN between two graphene layers and applying a bias voltage in a capacitor configuration to Stark-tune the energy of the emission. Additionally, there is the potential to pattern h-BN into a waveguide, enabling further control of the local density of optical states, the selection of single-photon emission modes, and the adjustment of emission rates through Purcell enhancement [27–30].

1.7 Indistinguishable single-photon emitters

Indistinguishable single photons are a fundamental concept in quantum optics and quantum information science, playing an important role in advancing technologies like quantum computing, quantum cryptography, and quantum communication. These photons are characterized by their identical properties in all quantum dimensions - including their polarization, frequency, phase, and spatial mode. This indistinguishability is crucial for various quantum phenomena and applications, particularly those based on quantum interference and entanglement [4].

1.7.1 Importance of indistinguishable single photons

Quantum interference: Indistinguishable photons can interfere quantum mechanically when they meet at a beamsplitter. This quantum interference is the cornerstone of numerous quantum computing algorithms and photonic quantum information processing techniques.

Quantum entanglement: The ability to generate entangled states, a key resource in quantum communication and computation, often relies on the indistinguishability of single photons.

Photons that are indistinguishable can be entangled more easily, enabling complex quantum networks.

Secure quantum communication: Quantum key distribution (QKD) systems, which provide secure communication channels, often utilize indistinguishable single photons. Their quantum properties ensure that any attempt at eavesdropping alters the quantum state of the photons, thus revealing the presence of an interceptor [31,32].

1.7.2 Challenges in generating indistinguishable single photons

Source consistency: One of the major challenges in generating indistinguishable photons is ensuring the consistency of the photon source. Any variation in the source, such as fluctuations in temperature or electromagnetic fields, can lead to distinguishable photons [33].

Photon synchronization: For applications involving multiple photons, such as quantum computing, synchronizing the arrival time of indistinguishable photons at a quantum gate or detector is crucial. Achieving this synchronization is technically challenging [34].

Scalability: Producing indistinguishable photons in a scalable manner remains a significant hurdle. While generating a pair of indistinguishable photons is achievable, scaling this to the levels required for practical quantum computing is an ongoing area of research [33].

1.8 Scope of this thesis

This thesis delves into the multifaceted world of single-photon emitters in h-BN, a field that stands at the forefront of quantum photonics research. At the time of this study, these emitters in h-BN were a relatively recent discovery, presenting a spectrum of challenges that needed

addressing to integrate them effectively into a range of technological applications. Our investigation is structured into several key chapters, each focusing on a specific aspect of these emitters, starting from their fundamental properties to their practical applications.

Chapter 2 is dedicated to a detailed examination of the factors influencing the linewidth of single-photon sources in h-BN. This analysis spans an array of variables, including the temperature conditions, the nature of the substrate, the thickness of the h-BN layers, and their crystalline quality. By dissecting these factors, we gain a clearer understanding of the hurdles in realizing lifetime-limited single-photon sources in h-BN, which is crucial for producing indistinguishable photons.

Moving to Chapter 3, the focus shifts to addressing the primary broadening mechanism that impedes achieving lifetime-limited emission, particularly at cryogenic temperatures. The chapter outlines a novel approach to mitigate this limitation, opening avenues for developing on-chip, lifetime-limited quantum emitters in h-BN. This advancement marks a significant leap toward harnessing the full potential of h-BN in quantum photonic applications.

Chapter 4 explores some of the less understood characteristics of h-BN quantum emitters. Here, we delve into the three-dimensional dipole orientation and pinpoint the exact axial location of these emitters within the h-BN crystal matrix, which is notably thicker than what has been conventionally studied. Our methodology involves the innovative use of phase change materials, coupled with precise engineering of the optical state's local density around the emitter. The insights gleaned from this study shed light on the fundamental origins and formation mechanisms of these emitters, a critical step in advancing our understanding of h-BN-based quantum technologies.

In Chapter 5, the thesis takes a deep dive into the intricate world of photon statistics of h-BN emitters. The focus is primarily on understanding the factors influencing the Mandel Q parameter, a key metric in photon statistics. The chapter demonstrates how an in-depth understanding of these statistical nuances can lead to groundbreaking applications, such as using h-BN emitters in random number generation, a critical component in secure communication systems.

Chapter 6 provides a forward-looking perspective, outlining the necessary advancements and research directions to unlock the full capabilities of h-BN emitters for applications that demand indistinguishable single-photon sources. This chapter not only highlights the existing challenges but also proposes innovative strategies to overcome them, paving the way for the next generation of quantum photonic devices.

In conclusion, this thesis presents a comprehensive exploration of h-BN single-photon emitters, emphasizing their immense potential in quantum photonics. Through meticulous research and innovative approaches, we demonstrate how these emitters can be optimized and potentially revolutionized, contributing significantly to the field of quantum technology.

Chapter 2. Linewidth broadening mechanisms in h-BN quantum emitters.

2.1 Abstract

We report reduction in the linewidth and suppression of spectral diffusion of quantum emitters in h-BN supported on a conductive substrate. We observe a temperature-dependent reduction the spectral emission linewidth for chemical vapor deposition (CVD)-grown, exfoliated, and bulk h-BN crystals on conductive indium tin oxide (ITO) relative to those seen on silicon dioxide (SiO_2) substrates, and show that inhomogeneous linewidth can be suppressed by 45% as a result of using a conductive substrate. We investigate the zero-phonon line profile at temperatures ranging from 4K to 300K and decompose the effects of thermal broadening and spectral diffusion at each temperature by Voigt fitting. The temperature dependence of homogeneous and inhomogeneous components of broadening is discussed.

2.2 Introduction

Single-photon emitters are essential building blocks of future quantum information technologies [35]. Many different single-photon sources have been proposed, including for example solid state lattice hosts such as epitaxially grown quantum dots [17], and atomic defects in diamond [36]. Each emitter type is characterized by spectral diffusion, i.e., temporal variations in emission energy around a nominal value, which poses a challenge to use of solid-state quantum emitters as sources of indistinguishable single photons [37,38]. Single-photon emitters in two-dimensional Van der Waals materials have garnered considerable attention due to their promising photophysical properties and the possibility for

on-chip integration [39,40]. Among them, color centers in two-dimensional dielectric h-BN are promising as a robust medium for generation of quantum light with potential for room temperature operation [19,24,41]. These color centers exhibit a Debye-Waller factor [2] >80%, a brightness on par with brightest sources of single photons [24,39,42], and linearly polarized emission [2,43], all at room temperature. These superior properties have the potential for quantum communication applications such as quantum key distribution in which a bright source of linearly polarized single photons is required [4,32].

However, several challenges for h-BN color centers exist that need to be resolved before making them suitable for quantum information and quantum sensing applications. The atomic structure of the defects underlying the color centers is under debate [20,44–48], as a result, the electronic and spin [49,50] characteristics of these emitters are still not clear, and methods to deterministically create emitters in h-BN crystals are not well developed [51–53]. Also, instabilities such as blinking [42,54,55], bleaching [56], and spectral diffusion [49,56–58] can yield interesting insights but ultimately represent significant drawbacks for use of h-BN color centers as a source of indistinguishable single photons. Recently Fourier transform limited spectral linewidths have been reported for h-BN emitters at both 4K and 300K [25,59]. This observation of Fourier transform limited linewidth has been reported to be limited to a 30 ms time window because of the spectral diffusion, limiting the achievement of indistinguishability for the spectral line in consecutive measurements.

Spectral diffusion is the temporal change in energy of emitted photons due to a change in the local electric field distribution of the emitter, and is manifested as a series of jumps of the zero phonon line (ZPL) for measurements with time resolution high enough to capture msec-μsec scale changes in the energy or as a broadening of the spectral lines when the spectrum is acquired over timescales longer than the time between spectral jumps [38,60]. This change in the local electric field is thought to be due to trapping and de-trapping of

charge at trap sites close to the position of active photon emitter or due to charges hopping from one site to another in the host lattice. The timescale of these spectral jumps in h-BN has been found to be on the order of microseconds to milliseconds [25,60]. Thermally grown silicon dioxide (SiO_2) on silicon, which is the material widely used as a substrate for graphene and other two dimensional materials [61,62] due to its low surface roughness, is an insulator prone to charge traps, which can be a source of spectral diffusion of color center emitters. Although other studies have noted the effect of substrate choice on emission in h-BN [49], the role of substrate in determining spectral linewidth has not been considered.

In this chapter, we report reduced linewidth and spectral diffusion when conductive transparent material indium tin oxide (ITO) is used as a substrate for h-BN color centers. As shown in Figure 2.1, a transparent conductive material such as ITO lacks charge traps on its surface and can provide a conductive pathway for charges trapped in h-BN to be removed in order to screen trapped and mobile charges from h-BN color centers, thereby suppressing spectral diffusion. Furthermore, ITO is transparent in the visible wavelength range but has a positive real part of its dielectric permittivity and hence does not quench luminescence emission in proximity to an emitter, unlike many other conventional metals. Spectral diffusion represents an obstacle to achievement of stable sources of indistinguishable photons. Thus developing methods to suppress spectral diffusion and increase the coherence time for h-BN single-photon emitters is an important step towards use of color centers as sources of indistinguishable photons in quantum applications based on single or entangled photons [32,63].

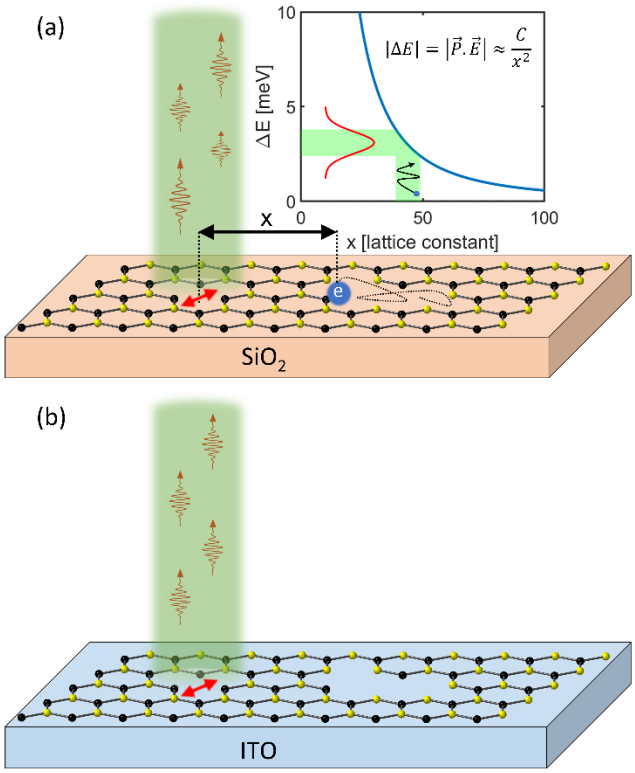

Figure 2.1. Schematic of substrate effect on spectral diffusion of single-photon emitters in h-BN. (a) h-BN emitter on insulating SiO2 substrate is prone to larger spectral diffusion due to charge traps in h-BN, SiO2, and their interface. (b) h-BN emitter on ITO substrate shows narrower linewidth as a result of fewer charge traps in h-BN, ITO, and their interface.

We start our analysis by investigating color centers in bulk h-BN. These centers reflect the intrinsic properties of h-BN emitters as they are inside the h-BN crystal and isolated from the environment. To fabricate bulk h-BN samples, we mechanically cleaved a thick flake from an h-BN crystal. AFM measurements show a thickness of 839nm.

Bulk h-BN preparation: h-BN crystals (HQ graphene) were exfoliated via mechanical exfoliation with scotch tape onto 300nm SiO_2 on Si substrate (MTI Corp.). Then the sample was annealed at 850C for 30 minutes under Argon at room pressure.

CVD h-BN preparation: CVD h-BN was grown by the method described in our previous work [64] and transferred via polymer assisted wet transfer technique [64] onto SiO_2 on Si (MTI Corp.) and ITO on Si substrate. No post processing was performed on CVD h-BN to activate emitters.

Exfoliated h-BN preparation: an h-BN crystal was annealed at 900C for 30 minutes under Argon environment and then flakes were exfoliated via mechanical exfoliation with scotch tape onto 300nm SiO_2 on Si substrate and ITO on Si substrate.

The thickness of h-BN was measured using Asylum Research Atomic Force Microscope (AFM).

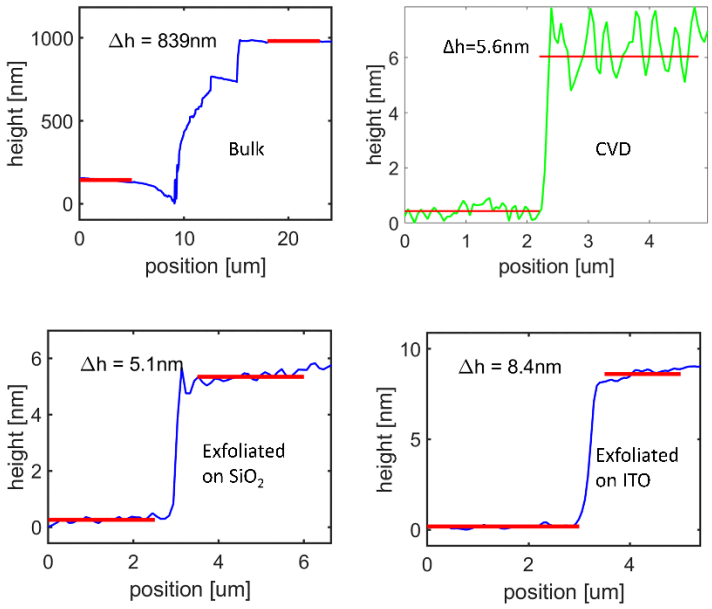

Figure 2.2. AFM measurement result of Bulk, CVD, and exfoliated flakes used for this study.

The ITO film is deposited via room-temperature RF magnetron sputtering on top of Si substrate. The deposition pressure is 3 mTorr and the applied RF power is 48W. The plasma is struck by using Argon gas with a flow rate of 20 SCCM, and Argon/Oxygen mixture gas with ratio 90/10 with a flow rate of 0.6 SCCM is used to control the resistance of the deposited layer. The thickness of ITO Film is 50nm.

Emitters were initially characterized in a homebuilt confocal microscope at room temperature and then transferred to a variable temperature microscope employing a closed-cycle helium cryostat to perform temperature-dependent emission measurements from 4K to 300K.

Room temperature characterization was done with a homebuilt confocal microscope. Emitters were pumped with a 100 μW beam of 532nm laser (Cobolt). Linearly polarized laser was passed through a quarter wave plate oriented at 45 degrees relative to the polarization axis to produce a circularly polarized light, we used circularly polarized light for excitation to excite all dipole emitters irrespective of their in-plane dipole orientation. Mapping was done with a Newport fast scanning mirror. a 100X (NA=0.95) Leica objective was used to focus the light on the sample and a tunable bandpass filter (Semrock Versa-chrome) was used to pass ZPL and we used a grating-based spectrometer (Princeton Instruments HRS300) to measure spectra.

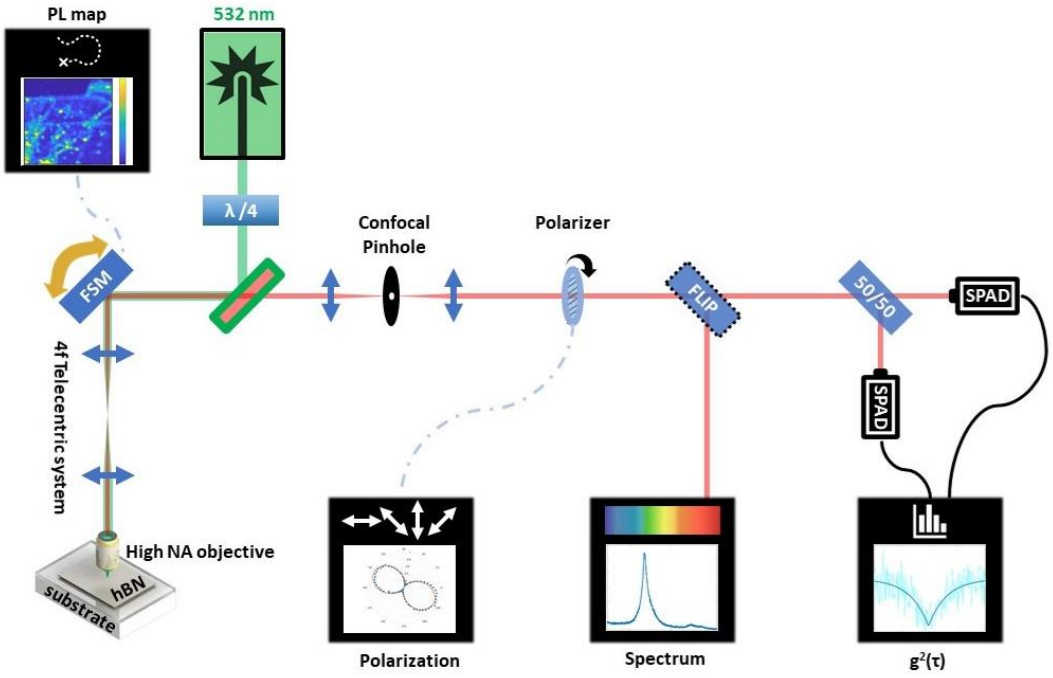

Figure 2.3. Schematic of homebuilt confocal microscope.

We used a 532 nm continuous wave laser to excite the emitters and the photoluminescence (PL) collected by a microscope objective through a tunable bandpass filter and either coupled to a spectrometer or a Hanbury-Brown-Twiss interferometer using two avalanche photodiodes to perform an intensity autocorrelation measurement. To locate and observe emitters in bulk h-BN, a photoluminescence map of the sample was acquired. The spectral and spatial features of 12 selected emitters were identified. For the rest of the discussion, we focus on two representative emitters among this group.

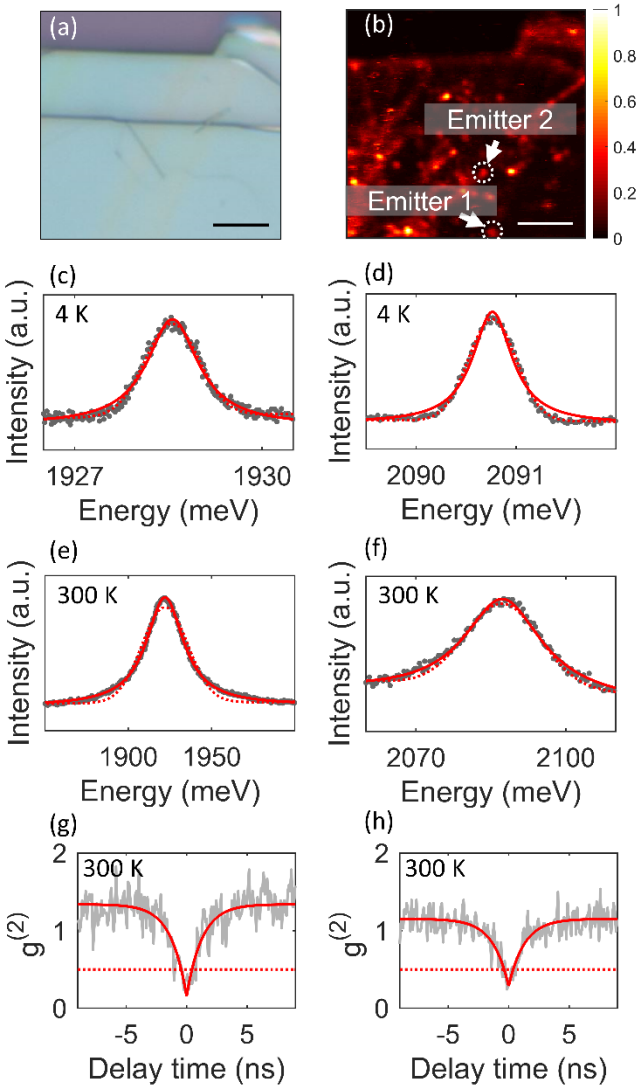

Figure 2.4. Quantum Emitters in bulk h-BN. (a) Microscope image and (b) photoluminescence map of a bulk h-BN crystal, the arrows show the position of two emitters understudy, scale bar corresponds to 5µm. (c) 4 K and (e) 300 K spectral of zero phonon line of emitter1 solid line shows Lorentzian and the dashed line shows Gaussian fits (g) shows photon antibunching for emitter 1. (d), (f), and (h) show the same plot for emitter 2.

Photoluminescence spectroscopy and intensity correlation measurements ($g^{(2)}$) of these two emitters are shown in Figure 2.4. No background subtraction was performed on $g^{(2)}$ data and the measurements were fitted by a double exponential model function:

$$g^2(\tau) = 1 - b[(1+a)e^{-\frac{|\tau|}{T_1}} - ae^{-\frac{|\tau|}{T_2}}].$$

Both photon flux statistics show a clear $g^{(2)}(0) < 0.5$, confirming that both emitters are single-photon emitters. They exhibit similar decay lifetimes (T_1 ≈1.3ns) but their bunching time scales (T_2) are different. A similar decay lifetime suggests that these emitters in principle should exhibit similar Fourier transform-limited linewidth if no extrinsic broadening mechanism is operative. The difference in the bunching shoulder can be explained by the difference in the blinking characteristics of these emitters. More importantly, we noticed that despite a nearly two-fold difference in the linewidth between these emitters both at room temperature and 4K, the lineshapes of both emitters are similar at the same temperature; namely, both emitters exhibit Lorentzian lineshape at 300K and Gaussian lineshape at 4K as shown in Figure 2.4.

Polarization measurement shown in Figure 2.5 was done by adding a wire grid polarizer (Thorlabs Inc.) before the light enters the beam splitter of HBT setup and inputs of two APDs were integrated to calculate signal. Two avalanche photodiodes (PicoQuant) were used to measure autocorrelation and a picoharp-300 module was used to register photon events in TTTR mode. g^2 data were analyzed with a custom MATLAB script and the result is shown in Figure 2.6.

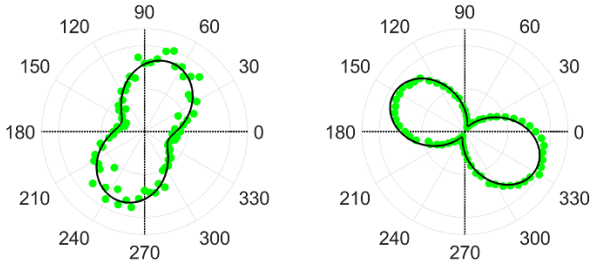

Figure 2.5. Polarimetry result of two emitters. Emitter 1 (left) shows some out of plane component and emitter 2 (right) shows almost completely in-plane dipole signature.

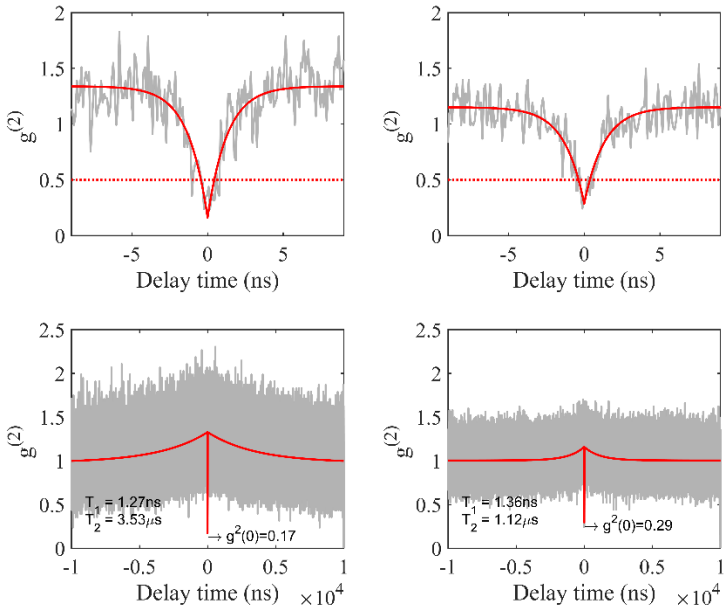

Figure 2.6. result of photon intensity autocorrelation measurement($g^{(2)}$).

Low-temperature spectroscopy was performed with an attocube attodry800 system. The sample holder stage was cooled by circulating liquid He. The sample was mounted on the cooled piezo stage using Apiezon thermal grease. A low-temperature attocube objective was used to focus 532nm fiber-coupled laser (PicoQuant) on the sample. Then the light was sent through a Raman spectrometer (Princeton instruments HRS750 spectrograph with 2400 g/mm grating) to measure PL with spectral resolution of 0.007nm at 532 nm Spectral resolution was measured by measuring linewidth of the 532nm laser.

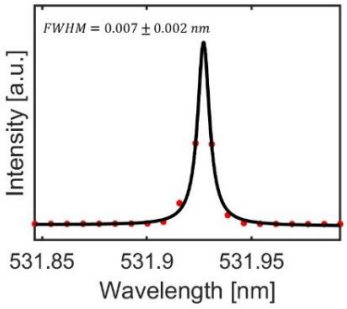

Figure 2.7. Spectral resolution of the spectrometer.

Each spectrum was acquired using 100μW laser power (measured before objective) and data acquisition time of 1 minute. For spectral stability measurements, 120 consecutive spectra were measured each for 1 minute.

2.3 Low frequency spectral diffusion

Low frequency spectral diffusion (spectral diffusion for time scales larger than 1 minute) is of the two emitters discussed is shown in Figure 2.8. At each time the peak position is detected using Voigt fitting and the trajectory of the peak is shown in panel b and e. To

analyze this trajectory, Fourier transform of the trajectory is calculated and shown in panel c and f.

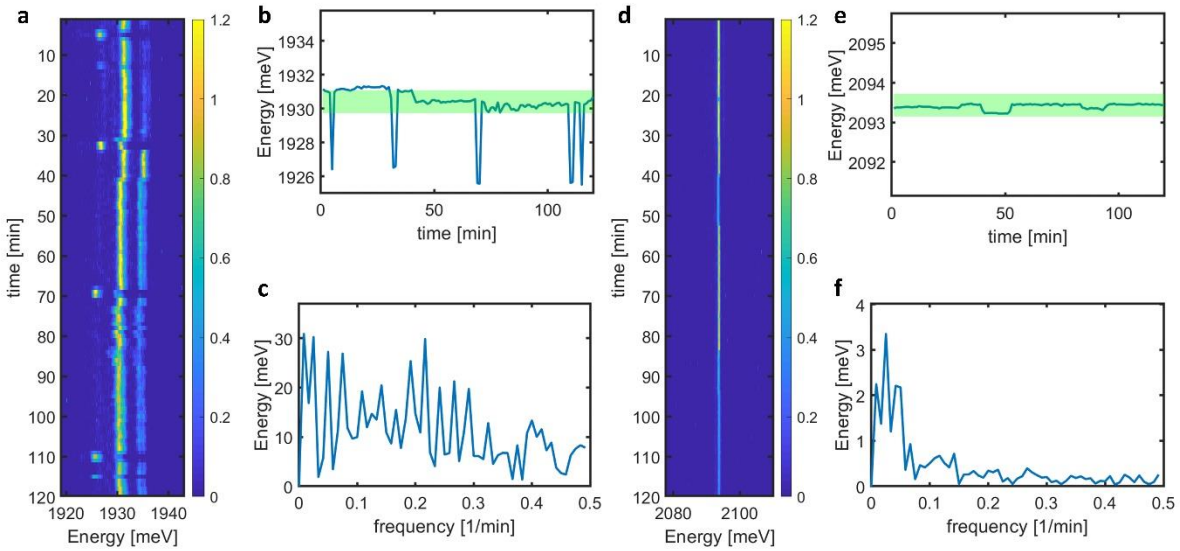

Figure 2.8. Low-frequency spectral diffusion signature of emitters. (a) shows spectral diffusion of emitter#1 for 120 minutes, (b) shows the position of ZPL peak at each time and (c) is Fourier transform of (b). Panels (d),(e) and (f) show similar results for emitter #2. The shaded region in (b) and (e) specifies the FWHM of each emitter.

Average amplitude of Fourier transform of slow spectral diffusion (w) of each emitter as a function of inhomogeneous linewidth is plotted in Figure 2.9. Except for one data point which corresponds to a defect with narrow inhomogeneous linewidth and strong spectral jumps the general trend shows increase of spectral diffusion as linewidth increases.

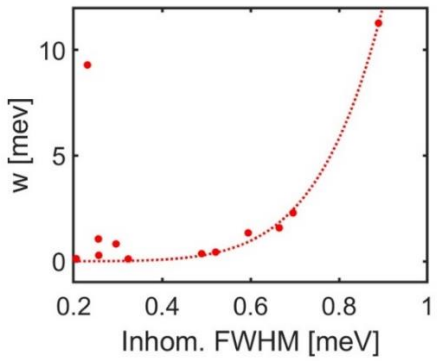

Figure 2.9. Correlation between average Amplitude of low frequency spectral diffusion and Inhomogeneous FWHM at 4K for 12 emitters in bulk h-BN.

To further investigate the effect of temperature, the ZPL was studied at temperatures 4K, 10K, 20K, 40K, 80K, 160K, and 300K and the results are illustrated in Figure 2.10. The evolution of the spectral line position and shape as a function of temperature is shown in Figures 2.10-a and 2.10-b for the two emitters. The linewidths for both emitters remain largely independent of temperature up to the transition temperature (T_{tr}) of 40K and increase significantly as temperature increases beyond T_{tr} (see Fig. 2.10-c). These observations also confirm two different modes of broadening for emitters in bulk h-BN: a temperature-independent broadening mechanism at T<T_{tr} and a temperature-dependent broadening at T>T_{tr}. a similar behavior has been observed in other quantum emitters and is attributed to spectral diffusion and thermal phonon interactions, respectively [38,60]. As an inhomogeneous broadening mechanism, spectral diffusion results in Gaussian lineshapes [38]. In contrast, thermal phonon broadening is a result of quadratic interaction between thermal acoustic phonons and the emitter and will result in a homogeneous broadening and a Lorentzian line profile [38,65]. As the temperature increases, the line profile also becomes less Gaussian and more Lorentzian. To analyze the line profile, we fit

a convolution of Gaussian and Lorentzian line-shapes to the line profile, also known as a Voigt profile:

$$I_V(\omega) = \frac{A\, Re[w(z)]}{\sigma\sqrt{2\pi}}$$

$$w(z) = e^{-z^2} erfc(-iz) \quad , \quad z = \frac{\omega - \omega_0 + i\gamma}{\sigma\sqrt{2}}$$

where A is amplitude and $FWHM_{Gaussian} = 2\sigma\sqrt{2\ln(2)}$ and $FWHM_{Lorentzian} = 2\gamma$. [60]

By fitting a Voigt profile to the measured spectral lines, we can measure the FWHM of each Gaussian and Lorentzian component of the line profile at each temperature and deduce the homogeneous and inhomogeneous FWHM. As can be seen in the Figure 2.10-e, for both emitters, the inhomogeneous broadening is independent of temperature up to T_{tr}, and at temperatures above T_{tr}, the Voigt fit does not show any significant Gaussian component and is predominantly Lorentzian. Therefore, for all temperatures investigated above T_{tr}, we set the value of the Gaussian FWHM to the measured average value of the inhomogeneous linewidth below T_{tr}, and we use a Voigt profile fit to find the Lorentzian FWHM component [38,60]. At T_{tr} =40K, the Gaussian (inhomogeneous) and Lorentzian (homogeneous) line profiles are almost equal for each emitter. We could also observe two separate peaks for emitter 1 and we attribute the weaker peak to spectral jumps at timescales shorter than the one minute exposure time of our spectral measurement, as the intensity of the second peak concerning the first peak varies significantly in time for time scales above one minute.

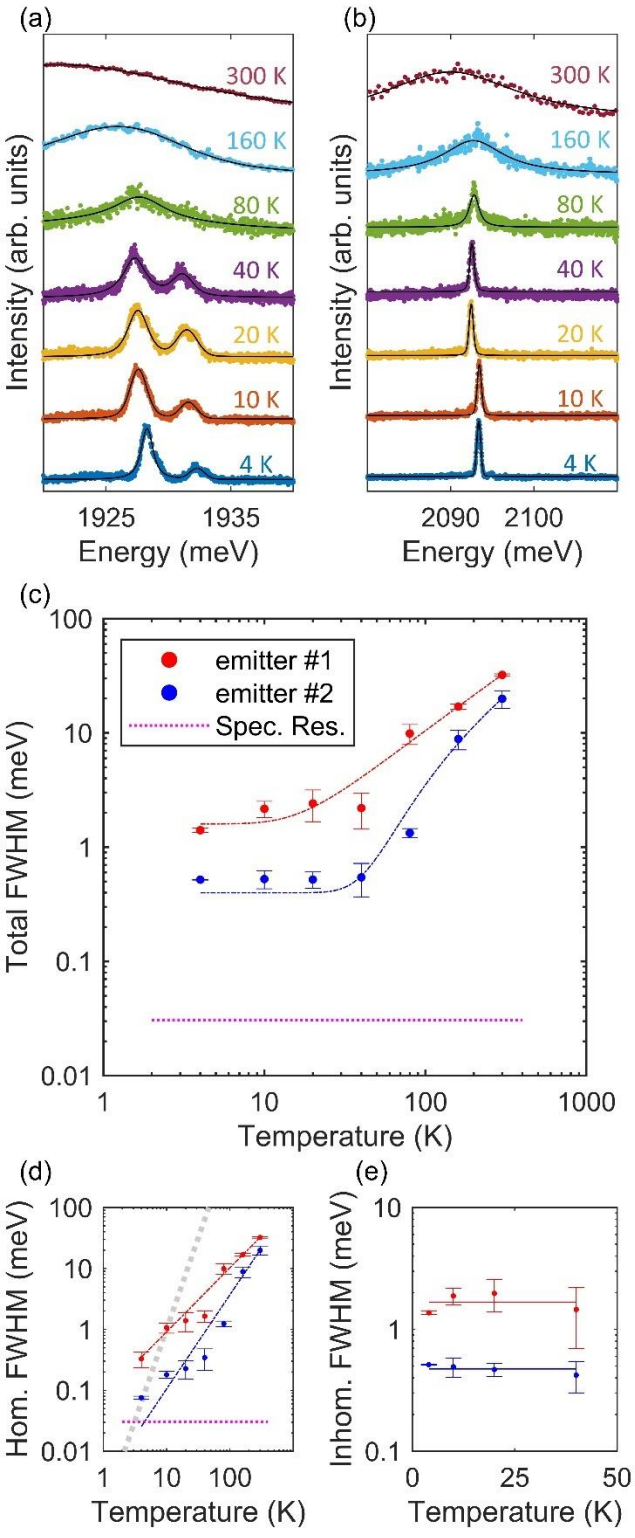
(a)
(b)
300 K
160 K
80 K
40 K
20 K
10 K
4 K
Intensity (arb. units)
1925
1935
2090
2100
Energy (meV)
(c)
emitter #1
emitter #2
Spec. Res.
Total FWHM (meV)
100
10
1
0.1
0.01
1
10
100
1000
Temperature (K)
(d)
(e)
Hom. FWHM (meV)
Inhom. FWHM (meV)
0
25
50
Temperature (K)

Figure 2.10. Temperature dependence of ZPL for emitters in bulk h-BN. Effect of temperature on lineshape for emitter 1 (a) and emitter 2 (b) from 4K to 300K. (c) shows linewidth against temperature for two emitters understudy linear fits for temperatures below and above 40K are shown, dashed lines are fits, and the dashed magenta line shows spectral resolution of the spectrometer used in this study. In (d) and (e) homogeneous and inhomogeneous components of linewidth extracted by Voigt fit are plotted as a function of temperature. The slope of power-law fit for homogeneous linewidth for emitter 1 is 1.05±0.21 and for emitter 2 is 1.54±0.38. The dotted grey line in (d) corresponds to T3 dependence of linewidth on temperature.

In Figure 2.10-d the homogeneous linewidth is plotted as a function of temperature in a log-log plot and the result for both emitters can be fitted by a line that corresponds to a power-law dependence of linewidth on temperature where the power is the slope of the fit line. We observe here a nearly linear dependence of the linewidth on temperature for both emitter #1 and emitter #2. This observation contrasts with other studies for h-BN and diamond quantum emitters which observed a power law dependence of third power form [38,60,66,67]. We speculate that this difference in observed power-law temperature dependence between the emitters investigated in the present study and previous work may be the result of different emitter color center structural and electronic configurations, a consequence of the diversity of defects seen in h-BN [25,68]. A similar linear dependence of linewidth on temperature is observed for excitons in 2D transition metal dichalcogenides [69–71]. Using a similar approach to model h-BN, the total linewidth γ_{total} of the ZPL can be written as the sum of an inhomogeneous contribution and a homogeneous contribution, cast in the form:

$$\gamma_{total} = \gamma_{inhom.} + \frac{b}{\exp\left(\frac{\theta}{kT}\right) - 1}$$

$$\approx \gamma_{inhom.} + \frac{kb}{\theta}.T$$

where 'θ' is the acoustic phonon energy and 'b' is a constant factor. As can be seen above, in a regime where the phonon energy is small compared to kT, a linear dependence of linewidth on temperature can be expected. Also recently a study [72] on exciton-phonon interaction in h-BN shows a similar linear trend in exciton-phonon scattering rate in h-BN.

We investigated the low-frequency spectral diffusion characteristics of these two emitters. Emitter 1, which has a broader linewidth, also exhibits larger spectral instability. Emitter 2, which has a narrower linewidth, exhibits fewer spectral jumps per unit of time, as can be seen from the Fourier transform of the time evolution trace of the peak position of emitter ZPL; emitter 1 has stronger spectral instabilities compared to emitter 2. We also confirmed this result for the other 10 emitters and this revealed a correlation between the inhomogeneous linewidth and the average of the Fourier transform of the measured spectral diffusion. This observation also suggests that the origin of inhomogeneous broadening in our measurements is most likely spectral diffusion.

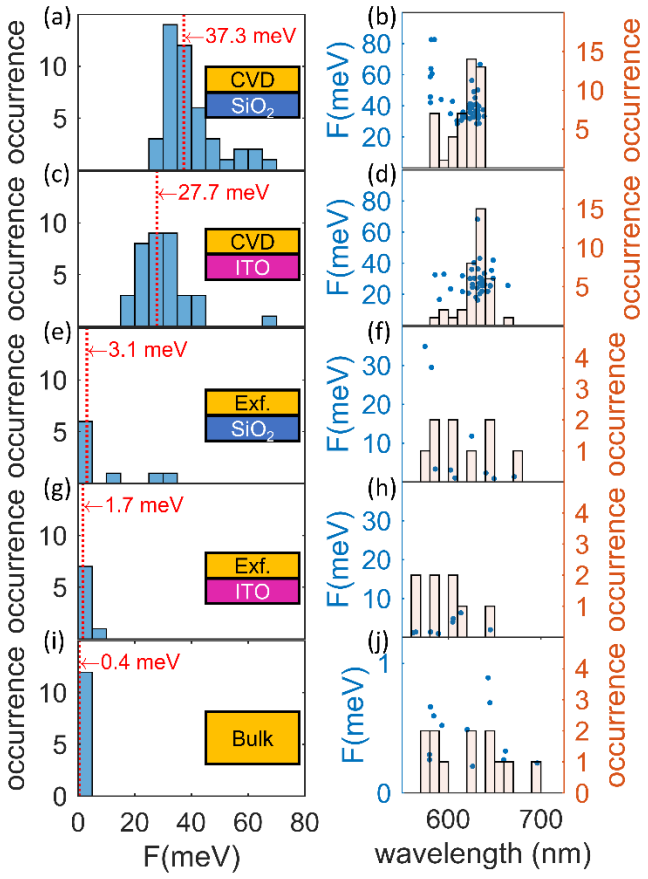

Figure 2.11. Effect of h-BN crystal and substrate type on inhomogeneous broadening. The left panel is a histogram of linewidths for emitters and the right panel is a scatter plot of linewidth against the ZPL wavelength (left axis) and histogram of the number of occurrences of a ZPL wavelength (right axis), for (a-b) CVD film on SiO2 substrate, (c-d) CVD film on ITO substrate, (e-f) exfoliated flake on SiO2 substrate, (g-h) exfoliated flake on ITO substrate, and (i-j) bulk h-BN crystal. The red dashed line shows the median of inhomogeneous linewidth for each sample.

Since in h-BN emitters, inhomogeneous broadening is the limiting factor to reach Fourier transform-limited linewidths at cryogenic temperature, we also performed a statistical

analysis of the inhomogeneous broadening. For the bulk h-BN sample, we can see that the minimum inhomogeneous FWHM is 0.21 meV (while the spectral resolution limit for our apparatus is 0.03 meV) and the median value is 0.41 meV.

Bulk h-BN has shown to have stable emitters with relatively narrow linewidths, however, to explore the full potential of the two-dimensional nature of h-BN, and to form layered heterostructures, emitters in samples with thicknesses of a few atomic layers are of considerable interest. A drawback of emitters hosted in a few atomic layer h-BN sample is susceptibility to the environment and this environmental effect can manifest itself as increased spectral diffusion and a decreased coherence time. Therefore, our investigation focused on h-BN layers less than 10nm thick. Chemical vapor deposition (CVD) is a widely employed method to grow thin films of h-BN and provides the ability to grow h-BN with an arbitrary number of layers on a scale of millimeters to centimeters. Another method for synthesis of few-layer h-BN crystal is by mechanical exfoliation, but this method does not provide large films of h-BN and lack precise control over the thickness of the exfoliated flakes, as one usually relies on trial and error to achieve the desired thickness. Nonetheless, this method can sometimes result in two-dimensional flakes with larger grain sizes.

To test the effect of measurement environment and h-BN crystal morphology on inhomogeneous broadening we transferred 5nm thick CVD-grown h-BN film – from the copper growth substrate onto SiO_2 and ITO substrates using wet transfer techniques (for details about the growth method, see [64]). We also exfoliated a 5nm thick h-BN onto SiO_2 substrate and an 8 nm thick h-BN onto the ITO substrate using exfoliation. We observed that for CVD h-BN, linewidths at 4K are almost one order of magnitude larger than those observed in the exfoliated samples with the same thickness and two orders of magnitude larger than emitters in bulk h-BN We attribute this difference in the linewidth of CVD and exfoliated samples to smaller grain sizes in the CVD films, which are expected to harbor a

larger charge trap density than in h-BN bulk crystals. Comparing different substrates, for CVD h-BN-atop-ITO samples, we observed a 27% reduction of the inhomogeneous FWHM compared to CVD h-BN-atop-SiO_2 from 37.3meV to 27.7meV, and for exfoliated h-BN-atop-ITO samples, we observed a 45% reduction of inhomogeneous FWHM compared to exfoliated h-BN-atop-SiO_2 from 3.1meV to 1.7meV. This observation confirms our hypothesis that using a conductive substrate suppresses spectral diffusion, which is attributed to conductive pathways for transport of charge away from the vicinity of the emitter, as depicted in Figure 2.1. Furthermore, no correlation between inhomogeneous broadening and the position of the ZPL wavelength was observed, which indicates that the inhomogeneous broadening mechanism is independent of defect structure and emission wavelength for both exfoliated and CVD h-BN.

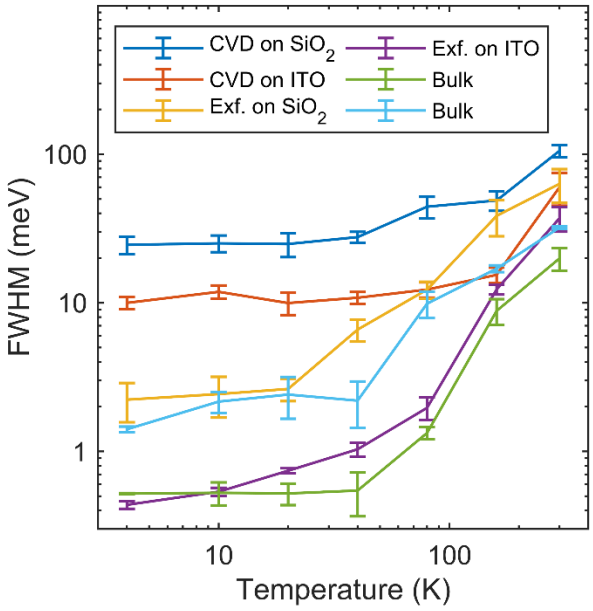

Figure 2.12. Temperature dependence of zero phonon line full width at half maximum (FWHM) for various emitters in bulk h-BN, 5nm thick exfoliated h-BN on SiO2, 8nm thick exfoliated h-BN on ITO, 5nm thick CVD h-BN on SiO2, and 5nm thick CVD h-BN on ITO. The result illustrates the total FWHM for temperatures from 4K to 300K.

For a better understanding of the effect ambient temperature, we observed emitters from each type of h-BN crystal morphology and substrate type studied here, and measured the emitter temperature-dependent linewidth for CVD and few-layer exfoliated h-BN on SiO_2 and ITO substrates. Unlike bulk h-BN, the transition from spectral diffusion-broadened to thermally broadened linewidth in CVD h-BN does not happen at T_{tr} =40K but it happens around T_{tr} =160K (see solid red and dark blue lines). This is a direct consequence of the larger spectral diffusion observed in CVD h-BN. For a few-layer exfoliated h-BN, we observed a larger change in the FWHM with temperature, and a transition temperature below 40K, despite a larger inhomogeneous linewidth (yellow and purple curves). We suggest that this

may be due to the proximity of emitters to the h-BN flake surface, and acoustic coupling to the substrate.

2.4 Summary and conclusion

In summary, we have studied the photodynamics of h-BN single-photon emitters in a diverse array of sample environments. We find both a temperature dependent and temperature independent regime for emitter linewidth that we attribute to thermally generated phonon interactions and spectral diffusion, respectively, as two mechanisms responsible for zero-phonon line emission broadening in h-BN emitters. We suggest that among these two regimes, spectral diffusion-limited linewidth is dominant at cryogenic temperatures and is independent of temperature, while thermal phonon interaction is dominant at temperatures close to room temperature and increases with a power-law dependence on temperature with power close to unity. Importantly, we find that the sample morphology and thickness, in the various configurations we investigated, affects the inhomogeneous linewidth, suggesting that the linewidth depends on both the local structure of h-BN and the surrounding environment in the crystal. In particular, we show that increasing the carrier density in the local environment of the emitter, achieved using a conducting substrate, significantly reduces the inhomogeneous linewidth. This last point is of interest for all applications that aim at spectral stability of color center based single-photon sources.

Chapter 3. 3-D dipole orientation and axial location of h-BN emitters

3.1 Abstract

Color centers in *h-BN* have emerged as promising candidates for single-photon emitters (SPEs) due to their bright emission characteristics at room temperature. In contrast to mono- and few-layered *h-BN*, color centers in multi-layered flakes show superior emission characteristics such as higher saturation counts and spectral stability. Here, we report a method for determining both the axial position and three-dimensional dipole orientation of SPEs in thick *h-BN* flakes by tuning the photonic local density of states using vanadium dioxide (VO_2), a phase change material. Quantum emitters under study exhibit a strong surface-normal dipole orientation, providing some insight on the atomic structure of *h-BN* SPEs, deeply embedded in thick crystals. Next, we optimized a hot pickup technique to reproducibly transfer the *h-BN* flake from VO_2/Sapphire substrate onto SiO_2/Si substrate and relocated the same emitters. Our approach serves as a practical method to systematically characterize SPEs in *h-BN* prior to integration in quantum photonics systems.

3.2 Introduction

Over the past few decades, point defects [73] that introduce electronic states with optical transitions, also known as color centers, have garnered great interest for quantum photonics applications, such as quantum computation and quantum information [74,75], quantum cryptography [76], and quantum sensing [5]. Wide-bandgap materials, such as

diamond [77], silicon carbide [78], gallium nitride [79], and zinc oxide [80] offer promising platforms for hosting quantum emitters with emission in the visible to near-infrared spectrum. However, these materials suffer from one or more intrinsic challenges such as a requirement for cryogenic temperatures, decoherence of emitted photons, optical coupling losses, and challenges associated with chip-based photonic integration. These problems have driven researchers to seek new candidate materials with fewer disadvantages [39,81].

Recent discoveries of quantum light emission from two-dimensional van der Waals (vdW) layered materials [2,82–86] have introduced promising candidates for single-photon emitters (SPEs). In contrast to bulk materials, vdW materials offer easier integration with photonic structures and minimal loss due to refractive index mismatch [40,41]. Among several candidate vdW host materials, *h-BN* has received particular attention due to its ability to offer a bright source of quantum light at room temperature. Remarkably, quantum emitters in *h-BN* have shown high (>80%) Debye-Waller factor [2], a brightness comparable to the brightest SPEs [39,41], polarized emission [2,43], giant stark shift [27,28], magnetic-field dependent quantum emission [50,87], correlated cathodoluminescence and photoluminescence emission [46], and near transform-limited optical linewidth [25], all reported at room temperature. To this date, the atomic structure of *h-BN* quantum emitters is not clear; the most common approach to deduce the atomic structure of these emitters has been to compare the energy of the zero-phonon line (ZPL) and phonon-assisted emission to the first-principles calculations [20]. Furthermore, to understand and quantify the intricate details of the emitter atomic structure, in particular spin-manifold, optically detected magnetic resonance (ODMR) technique has been recently reported [50]. Accurate information of 3D orientation of emitting dipole would provide invaluable insight into the underlying symmetry properties of the defect center,

which can complement the aforementioned approaches and help in identifying the atomic origin of emitters.

Quantum emitters in multi-layered flakes, in contrast to mono- and few-layered flakes, show superior emission characteristics such as higher saturation counts and spectral stability due to reduced environmental screening effects [88]. Efficient coupling of these quantum emitters with nanophotonic structures would require precise information about their axial position and 3D dipole orientation. Determining, both, the 3D dipole orientation and axial position of a quantum emitter in any multi-layered *h-BN* poses as a coupled problem because the polarization characteristics of detected photons is strongly influenced by either dipole orientation or axial position.

In this chapter, we demonstrate nanometer-scale axial location of *h-BN* quantum emitters in a multi-layered flake by leveraging highly sensitive, distance-dependent modulation of the spontaneous emission lifetime of these quantum emitters when in close proximity to a tunable phase-change material, vanadium dioxide (VO_2). Specifically, we modify the local density of optical states (LDOS) by inducing an insulator-to-metal transition in VO_2 which in turn modulates the emission rate of quantum emitters near the *h-BN*/VO_2 interface. This method, taken together with emission polarimetry to determine the three-dimensional (3D) orientation of the quantum emitter, gives comprehensive information about emitters axial position and orientation, which could be used to distinguish possible candidates based on atomic structure of the emitter. Furthermore, we have optimized a polymer-assisted hot pickup and transfer process to reliably transfer *h-BN* flakes from VO_2 substrate onto other device substrates (here, we use SiO_2/Si substrate as target), following which, the emitters under investigation were relocated. Measurement of *h-BN* emitter location and 3D orientation with nanometer-scale resolution in multi-layered flakes together with advances in precise transfer and stacking of 2D materials [89]

and metal contacts [90] offer opportunities for both fundamental physics advances [91] and quantum photonic technologies [32,92].

3.3 Effect of LDOS on h-BN emitters

The experimental configuration is shown in Figure 3.1-a. A quantum emitter is located at a distance d, within the thickness of an *h-BN* flake, from the surface of a substrate that consists of a thin layer of VO_2 on sapphire. Photoluminescence excitation and detection were performed with optical pumping of quantum emitters by laser excitation from the top. The excitation wavelength was set to 532 nm. The excited quantum emitter emission decay rate depends on its interaction with the optical environment [93]. By optical environment we mean the substrate beneath and the air above the *h-BN* flake. We model this interaction by treating the quantum emitter as an oscillating point dipole source oriented along the direction (θ, φ). For an emitter in an unbounded, homogeneous, and lossless medium with a refractive index n, the spontaneous decay rate is enhanced by a factor n compared to the free space. This result also holds true for bounded geometry as long as the emitter is at a distance $d \gg \lambda$ from any interface. When $d \ll \lambda$ the decay rate strongly depends on d, the dipole orientation (θ, φ), and the refractive index contrast across the interface [94–96]. In this work, we manipulated the optical environment of a quantum emitter located in the vicinity of the *h-BN*/VO_2 interface using VO_2 whose complex refractive index exhibits a sharp change when VO_2 is thermally switched from the insulating to metallic state, which occurs at near room temperature $T_c \sim 340$ K [97].

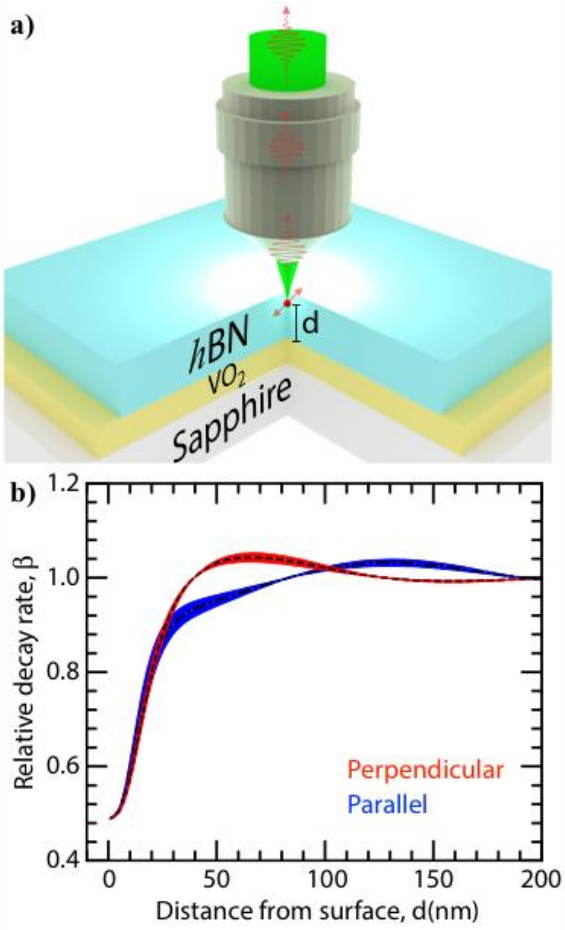

Figure 3.1. Experimental schematic and distance-dependent modulation of relative decay rates. (a) Schematic of a quantum emitter in an atomically thin crystal of h-BN located within the thickness of a flake on a substrate which consists of a thin layer of vanadium dioxide (VO2) deposited on a sapphire crystal. (b) Relative decay rate $\beta = \gamma_{Insulating}/\gamma_{Metallic}$ as a function of distance d of a quantum emitter from the surface of VO2 when switched from the insulating to metallic state. The blue and red curves refer to quantum emitters oriented parallel and perpendicular to the surface, respectively, and the shaded regions corresponds to the typical quantum yield (QY) range of 0.6-1.0 of h-BN quantum emitters with zero-phonon line around 600 nm. For numerical simulation we considered the emission wavelength of 600 nm for the quantum emitter corresponding to the emitter A. The dashed line within the shaded region corresponds to QY = 0.79 as estimated from our experimental data. The refractive indices of the upper medium, h-BN, and that of sapphire were set to 1, 1.82, and 1.77, respectively. The refractive index of VO2 at 600 nm was set to 3.05 + 0.42i (insulating state) and 2.57 + 0.64i (metallic state) from our ellipsometry data.

Figure 3.1-b shows the calculated relative decay rate $\beta = \gamma_{Insulating}/\gamma_{Metallic}$ of an emitter as a function of distance *d* when the emitter is oriented perpendicular ($\theta = 0°$) and parallel ($\theta = 90°$) to the *h-BN*/VO_2 interface. Here, $\gamma_{Insulating}$ and $\gamma_{Metallic}$ is the total (radiative and non-radiative) decay rate of the emitter when VO_2 is in insulating (30 ℃) and metallic (100 ℃) state, respectively. In these simulations, we considered a flake thickness of 310 nm and an emission wavelength of 600 nm, corresponding to one of the quantum emitters in our experiment, shown in Figs. 3.7-d and 3.7-e. The refractive indices of the upper medium, *h-BN*, and that of sapphire were set to 1, 1.82 [98], and 1.77, respectively. The complex refractive index of VO_2 at 600 nm was extracted from our ellipsometry data and was set to 3.05 + 0.42i and 2.57 + 0.64i for VO_2 in insulating and metallic state, respectively. The thickness of the VO_2 layer on sapphire was set to 40 nm. In general, the photoluminescence quantum yield (PLQY) of *h-BN* quantum emitters varies in the range 0.6–1.0 (10,19) and a recent experiment has shown average PLQY in the range 0.6–0.8 for quantum emitters with zero-phonon line (ZPL) around 600 nm. The shaded area in Figure 3.1-b, corresponds to this PLQY range. The dashed line within the shaded regions corresponds to a PLQY = 0.79 estimated from our experimental data. As can be seen in our simulation results, the relative modulation of decay rates for both orientations is clearly evident within first ~50 nm that quickly fades away at distances ~100 nm and above. We use this highly sensitive, distance-dependent decay rate of quantum emitters in the vicinity of the *h-BN*/VO_2 interface to localize their position along the axial direction.

3.4 VO_2 characterization, optical properties, and optimization

We performed visible ellipsometry measurement to extract real and imaginary parts of refractive index of VO_2 at 30°C and 100°C. We clearly observe the switching of the optical constants of the VO_2 film when reaching the temperature triggered phase transition. It is worth noting that, *n* decreases in the wavelength range, while *k* increases as VO_2 undergoes an insulator-to-metal transition. To date, quantum emitters in *h-BN* exhibit ZPL emission in the range 550-800 nm; thus, VO_2 is well-suited to modify the optical environment of *h-BN*-based quantum emitters.

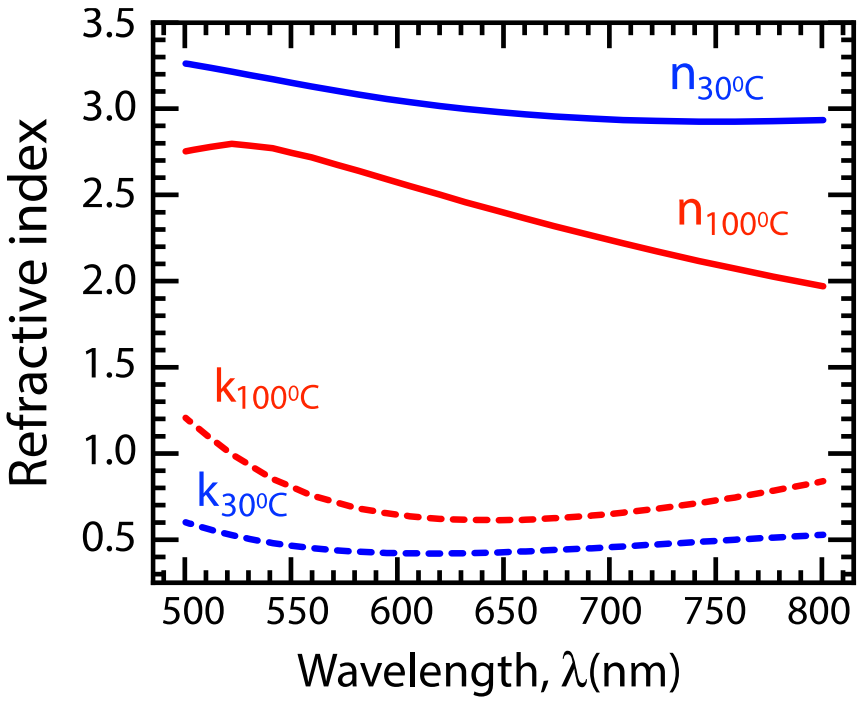

Figure 3.2. Complex refractive index of VO2 in insulating and metallic phase. Extracted value of real (n) and imaginary (k) part of the complex refractive index of 40 nm thick layer of VO2 deposited on sapphire crystal at 30 °C (blue) and 100°C (red) from our ellipsometry data.

We also measured the response of the Peltier element to measure how long it takes to reach the stabilized temperature. From room temperature to 100 °C it takes less than 100 seconds but from 100°C to room temperature it takes around 1000 seconds, hence each time we waited 5 minutes when we were heating up and waited an hour when we were cooling down. We employed the Bruggeman effective medium approximation to estimate the intermediate optical constants as a function of volume fraction of the metallic phase of the VO_2 layer [99]. The legend R (0.00) denotes the purely insulating phase VO_2, while the legend R(1.00) represents the purely metallic phase VO_2. The estimated optical constants

were used in full-wave simulations to monitor the reflectance values at normal incidence. The full-wave simulation results are consistent with the measured spectra, which validates the refractive index and the thickness of the VO_2 film that we characterized.

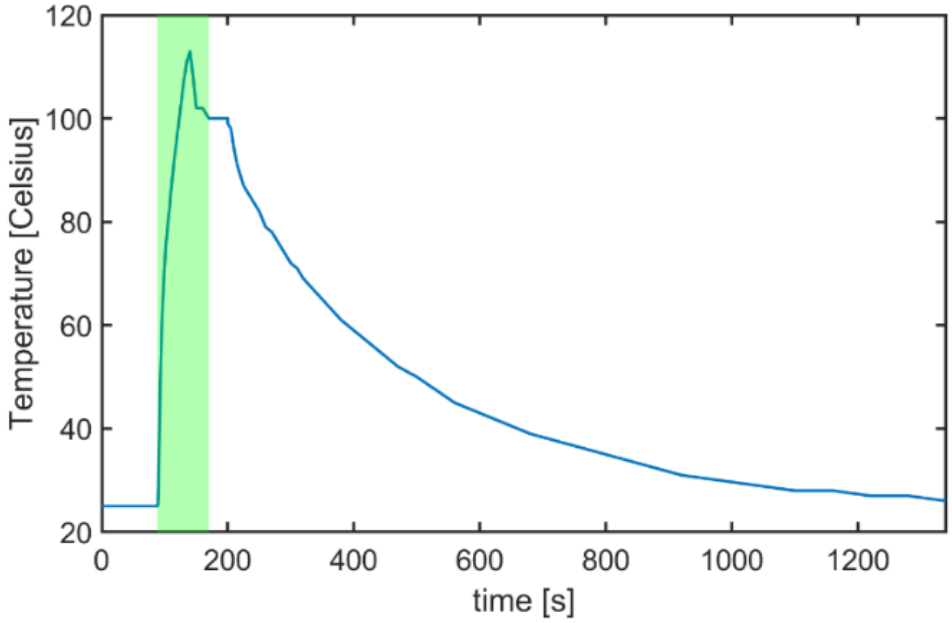

Figure 3.3. Temporal response of Peltier stage. Response of the Peltier stage as a function of time for ramp up and cooldown. Shaded region shows the ramp up region and the temperature is set to 100℃ for 30 seconds and then the temperature decreases as a result of convection.

In order to characterize the optical properties of the VO_2 film grown on a sapphire substrate, we measured reflectance spectra in the visible range. The temperature-dependent reflectance curves were measured by using a microscope spectrometer with an external heating stage. Figure 3.4 shows the temperature-dependent reflectance modulation in the 30–100°C range of the 40-nm–thick VO_2 film for the heating cycle. We observed a gradual reflectance change as a result of the insulator-to-metal transition when we slowly changed

the substrate temperature. The temperature-dependent curves represent a gradual decrease of the reflectance as the VO_2 film becomes a lower index and a more lossy metallic state.

Numerical simulations were performed using the commercial finite element software COMSOL Multiphysics for frequency domain electromagnetic full-field calculations. The simulation domain was truncated using perfectly matched layers. We modelled a quantum emitter as an electric point dipole source and calculated the spontaneous emission rate by probing the field at the location of the dipole. The non-radiative contribution to the decay rate was calculated by probing the heat generated in the lossy material (VO_2). The complex refractive index of VO_2 at the ZPL of emitters A, B, and C were taken from our ellipsometry data. The refractive index of *h-BN* was set to be 1.82 at 600 nm, and a weak linear variation was employed to calculate refractive index at 570 nm and 620 nm as 1.84 and 1.81, respectively.

We performed full-wave electromagnetic simulations using finite difference time domain methods to estimate the optimal thickness for a VO_2 film in order provide the largest optical contrast in the photoluminescence wavelength range.

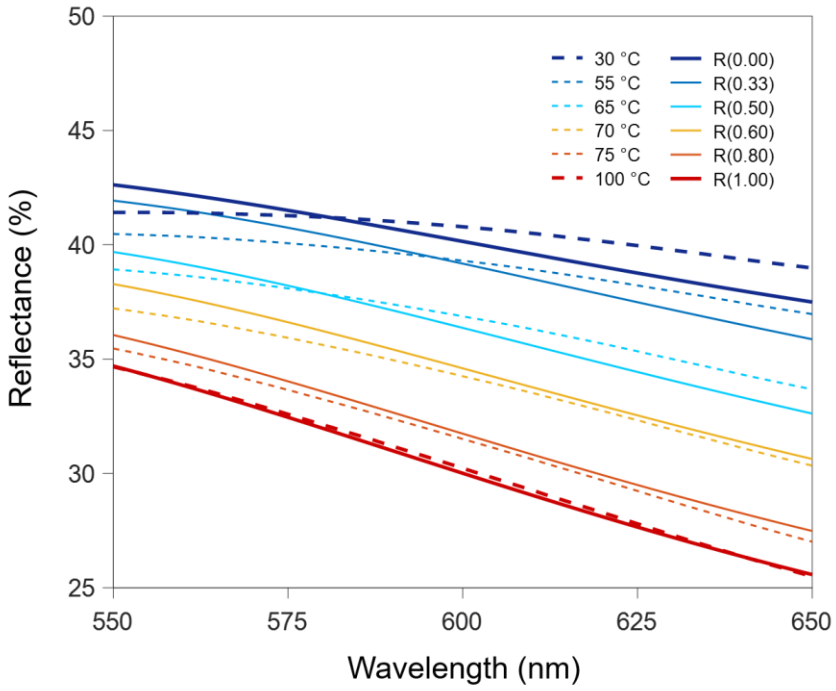

Figure 3.4. Temperature-dependent reflectance spectra of a VO2 film during the heating cycle (dotted lines) and simulated reflectance curves of the film using the Bruggeman effective medium theory (solid lines). We observe gradual reflectance variations upon phase transition in VO2, where the volume fraction of metallic phase VO2 gradually evolves within the insulating phase VO2 host.

We used a commercial Lumerical finite-difference time-domain software package to obtain the reflectance spectra of the VO_2 film on a sapphire substrate. The reflectance maps of the thin film structure were monitored by varying the thickness of the VO_2 film for both insulating and metallic phases. Finally, the thickness of VO_2 film was optimized based on the FOM equation shown below. Figure 3.5 represents the simulated FOM map, which indicates that about 40-nm-thick VO_2 film shows the largest reflectance contrast at the zero-phonon lines of our exfoliated *h-BN* flake. Based on this analysis, we grew 40-nm-thick VO_2 films as explained in Section S8.

$$FOM = \frac{|R_{Metallic} - R_{Insulating}|}{R_{Metallic} + R_{Insulating}}$$

Here, $R_{Metallic}$: metallic phase reflectance and $R_{Insulating}$: insulating phase reflectance.

A 40-nm thick vanadium dioxide (VO_2) film was formed on a cleaned c-plane single side polished sapphire substrate by pulsed laser deposition. A high-power pulsed laser beam vaporizes a vanadium target which deposits a thin film on the sapphire substrates in the presence of 5 m-Torr oxygen gas at an elevated temperature (650°C). First, we confirmed that the surface of the VO_2 film grown on the sapphire substrate was uniform and continuous with root mean square roughness of around 1.5 nm that were measured by atomic force microscopy. The measurement result shows the morphology of the VO_2 film which consists of smooth and continuous small grains.

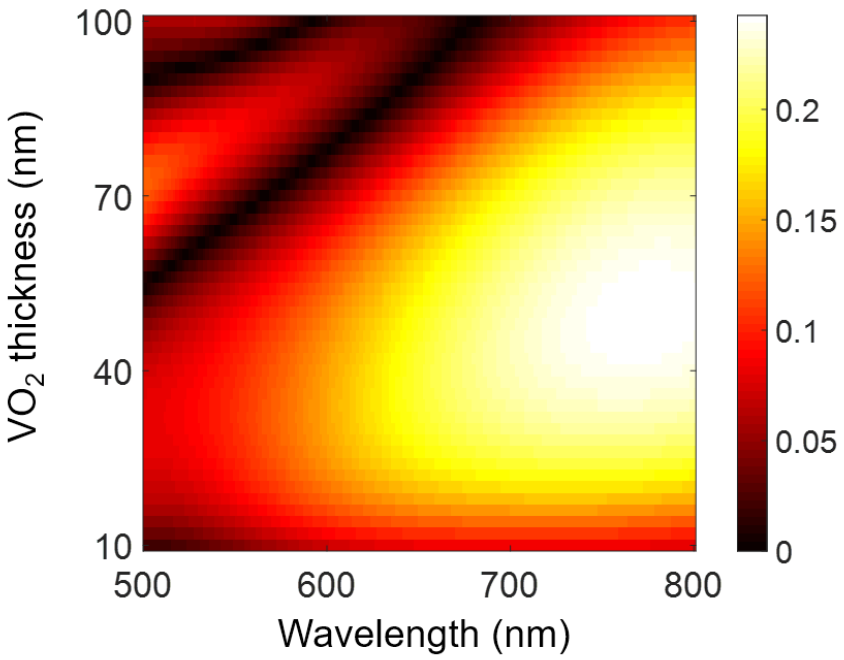

Figure 3.5. Optimization of VO_2 thickness. Figure of merit map (FOM) of a VO_2 film on a sapphire substrate obtained by full-wave simulations. The FOM indicates the reflectance contrasts between the insulating and metallic phases of VO_2. The results indicate that the largest optical contrasts at the zero-phonon lines when VO¬2 thickness is about 40 nm.

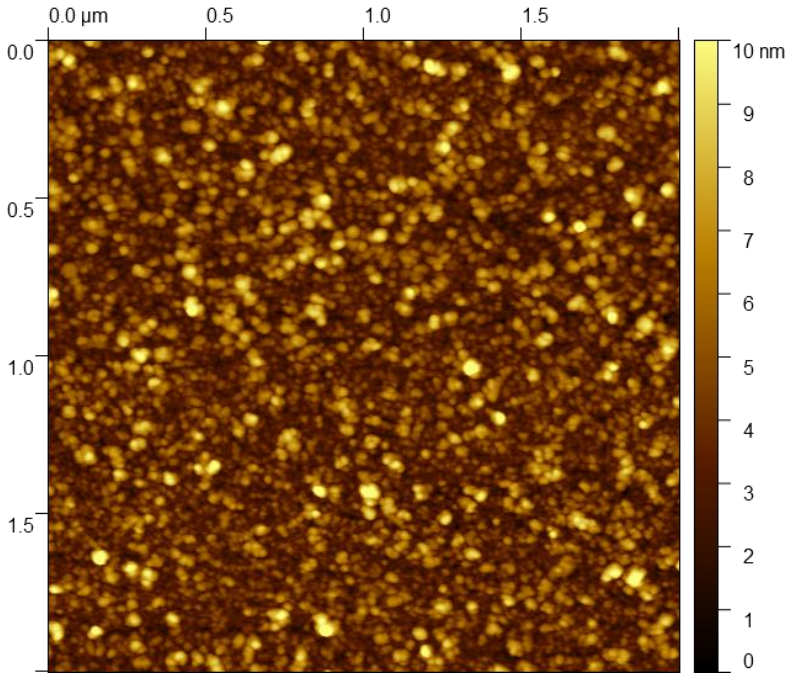

Figure 3.6. Surface characterization of VO2 film. Atomic force microscope measurement of VO2 film deposited on a sapphire substrate. This result shows that the film is uniformly grown, and the root-mean-square roughness is around 1.5 nm (2 µm × 2 µm) which is much smaller than thickness of the film which is 40 nm.

3.5 h-BN emitter characterization

Figure 3.7-a shows the optical microscope image of a thin *h-BN* flake on a VO_2/Sapphire substrate. This sample was prepared by mechanical exfoliation of high purity *h-BN* single crystals and transferred onto a 40 nm thick VO_2 film deposited on 500 μm thick sapphire by pulsed laser deposition. To determine the thickness of this flake at each position, we employed atomic force microscopy (AFM). Figure 3.7-b shows an AFM image of the *h-BN* flake shown in Figure 3.7(a). The red dot in Figs. 3.7-a and 3.7-b indicates the location of the quantum emitters A and B with emission wavelength of 600

nm and 620 nm, respectively. Figure 3.7-c show AFM height profile across the lines (S-E) indicated in Figure 3.7-b where flake thickness varies in the range 230-420 nm. At the location of the emitter A and B height of the flake is 310 nm and 340 nm, respectively.

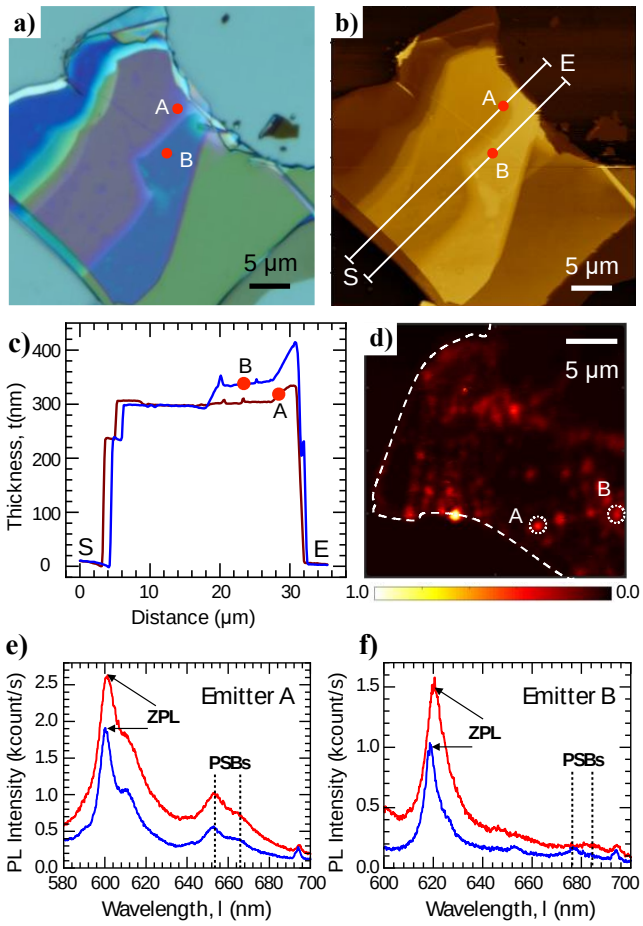

Figure 3.7. Characterization of the exfoliated flake and spectra of h-BN quantum emitters. (a) Optical image of the mechanically exfoliated h-BN flake on VO2/Sapphire substrate. (b) Atomic force microscopy image of the flake shown in (a). The red dots on the traces (S-E) in (b) and (a) indicate the position of emitters A, and B with emission wavelength of 600 nm and 620 nm, respectively. (c) Line profiles along the region indicated by the trace in (b). At the location of the emitter A and B height of the flake is 310 nm and 340 nm, respectively. (d) Confocal photoluminescence (PL) map of the h-BN flake. The position of two single-photon emitters is marked by white circles. The edge of the flake in marked by white dashed line. The PL spectra of emitters A and B shown in (e) and (f), respectively, were obtained with VO2 in

insulating state (blue) and metallic state (red). In these spectra ZPL and phonon sidebands (PSBs) are highlighted and the small peak around 692 nm corresponds to the emission from sapphire.

To locate the quantum emitters precisely, we performed confocal photoluminescence (PL) mapping in mode by which the sample was scanned point by point. Figure 3.7-d shows a PL map over an area of 20 x 20 μm^2 on the *h-BN* flake. The location of the quantum emitters A and B are highlighted by dashed circles. The single-photon emission nature of these quantum emitters is evident from their second-order autocorrelation measurements indicating $g^2(0) < 0.5$. Figures 3.7-e and 3.7-f show the PL spectra of these quantum emitters obtained for insulating and metallic VO_2. The emission spectra of each quantum emitter consist of a pronounced ZPL accompanied by a weaker phonon assisted emission [2,39]. An increase in PL intensity as obtained for metallic VO_2 compared to insulating VO_2 is noticeable for all quantum emitters, which in general suggests a higher photon emission rate, i.e., a decrease in emission lifetime, a change in illumination pattern, or any of these. However, in our experiments, a decrease in the emitter lifetime obtained from Hanbury Brown and Twiss (HBT) measurements for metallic VO_2 compared to insulating VO_2 suggests that this increase in absolute PL intensity originates from enhancement of emission rate. Recent experiment has reported that the decay rate of *h-BN* quantum emitters remains constant even when heated up to 800 K [24] which further corroborates that the enhancement of decay rate is due to modification in LDOS rather than a thermal effect. The defect-based quantum emitter dimensions are at the atomic scale, and thus the lateral position can be precisely measured down to few tens of nm when a sufficient number of photons is collected by the camera along with low noise (readout and amplification) and background signals.

To investigate the single-photon emission characteristics and decay lifetime of the quantum emitters, we measured their second-order intensity correlation functions $g^2(\tau)$ in both insulating and metallic phases of VO_2. In order to reduce the influence of background signal and noise, we corrected the raw $g^2_{raw}(\tau)$ using the function $g^2(\tau) = [g^2_{raw}(\tau) - (1-\rho^2)]/\rho^2$, where $\rho = S/(S+B)$ where *S* and *B* refer to the signal and the background counts, respectively. This background corrected $g^2(\tau)$ was fitted with double exponential of the form

$$g^2(\tau) = 1 - \rho^2\left[(1+\zeta)e^{-\gamma_1|\tau|} - \zeta e^{-\gamma_2|\tau|}\right]$$

where, $\zeta, \rho, \gamma_{1,2}$ are laser power-dependent parameters [43,100]. Here, γ_1 and γ_2 are the faster and the slower decay time constants, respectively, for a three-level system. The second-order intensity correlation functions $g^2(\tau)$ under continuous wave excitation pumping for the quantum emitters A and B is shown in Figs. 3.8-a and 3.8-b, respectively, when VO_2 is insulating (blue dots) and metallic phase (red dots). The data for the metallic phase VO_2 configuration has been offset vertically for visual clarity. Equal-time coincidence counts $g^2(0)$ for each quantum emitter is less than 0.5, which indicates the presence of a single emitter. All measurements were performed at a constant 50 µW pump laser power which is orders of magnitude smaller compared to the saturation power of ~ mW for *h-BN* quantum emitters [39–41]. Given the Fresnel reflections from all interfaces, which were analyzed using full-wave simulations, the excitation power within the flake along the axial direction is position dependent. From fitting our experimental data of correlation functions $g^2(\tau)$, we extracted the decay constants ($\gamma_{1,2}$) which has contributions from the spontaneous decay rates and the pump rate [24,68]. The spontaneous decay rates (γ) of the emitters A and B are shown in the Table 3.1. The correlation functions over long-time scales are shown in Figure 3.13. With an excitation power of 50 µW, the pump rates are ~ 25-fold and 73-fold slower than the spontaneous

decay rates for emitters A and B, respectively, and thus make negligible contributions to the decay constants. From Table 3.1, we clearly see that for all the emitters, the decay rates are higher in the presence of a metallic-VO_2 when compared to an insulating-VO_2 configuration. Thus, the emitters A and B are located at distances, from the surface of VO_2, such that their optical environment is modified when VO_2 undergoes an insulator-to-metal transition.

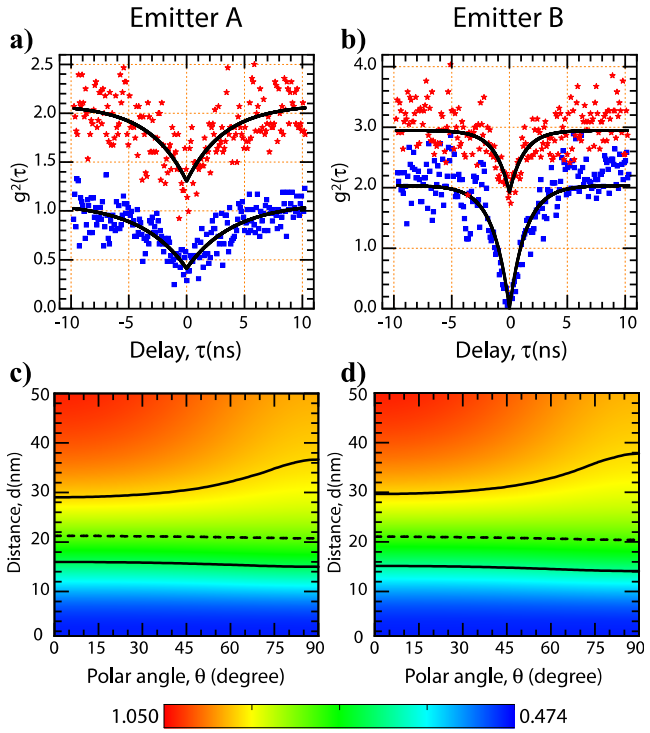

Figure 3.8. Single-photon source characterization and axial location in h-BN flake. Plot of the second order photon correlation measurement, g2(τ) for the emitters A and B, in (a) and (b), respectively. The experimental data, blue squares for insulating VO2 phase and red stars for metallic VO2, were fitted to obtain the decay rates of the emitters. From the fit, we calculated the relative decay rates $\beta=\gamma_{Insulating}/\gamma_{Metallic}$ for the three emitters A and B as 0.818 ±0.108 and 0.800±0.124, respectively. For clarity, g2(τ) data obtained for metallic VO2 in (a), and (b) were shifted by 1 and 1.5, respectively. Plot of the relative decay rates β as a function of the distance (d) from the surface of VO2 and the polar angle (θ) for the emitters A and B are shown in (c) and (d), respectively. The dashed contour lines in (c) and (d) correspond

to the experimental value of β obtained from (a) and (b), respectively, while the solid lines correspond to the error (±Δβ) in the ratio.

To model the distance-dependence of the quantum emitter lifetime on VO_2 phase, we define the ratio of their decay rates in the insulating and metallic phases as β. Figures 3.8-c and 3.8-d show the two-dimensional plot of relative decay rate β as a function of distance d from the *h-BN*/VO_2 interface and the polar orientation angle θ of the dipole for each quantum emitters A and B, respectively. Each plot has three contour lines; a dashed line for the relative decay rates β while the upper and the lower solid contour lines correspond to the error in decay rate ($\pm \Delta\beta$). Using the experimental values of γ from the Table 3.1, we obtained the relative decay rates β for the quantum emitters A and B, as 0.818 ± 0.108 and 0.800 ± 0.124, respectively. From these simulations and the experimental values of β, it is evident that the quantum emitters are located within a narrow region at a distance $d \sim 21$ nm from the surface of *h-BN*/VO_2 interface. However, the uncertainty in the axial position depends on the emitters' polar angle θ. For emitter A, uncertainty (full width) varies from ~ 13 nm at $\theta = 0^0$ to ~ 22 nm at $\theta = 90^0$. Similarly, for quantum emitter B uncertainty in their axial location varies from ~ 15 nm to ~ 23 nm at $\theta = 0^0$ and $\theta = 90^0$, respectively.

3.6 LDOS engineering with phase change material

Figure 3.9 shows the individual contribution from radiative and non-radiative channels to the decay rates $\gamma_{Insulating}$ (Figures 3.9-a,b) and $\gamma_{Metallic}$ (Figures 3.9-c,d) for both parallel and perpendicular orientations as a function of the distance (d) from *h-BN*/VO_2 interface. The non-radiative decay rate of the emitter corresponds to the emission of a photon which is absorbed in the lossy material VO_2. For numerical simulation we considered an *h-BN*

quantum emitter with ZPL wavelength of ~ 600 nm and PLQY of 0.79. Figure 3.9 illustrates that at distances in the range ~ 0–15 nm, decay rate γ is dominated by the non-radiative channel and thus the emitters located within this range of distances are "hidden" owing to a lack of light emission available for collection objective lens. However, the radiation contribution to the total decay rate is stronger for vertical dipole compared to the horizontal dipole within first ~50 nm with both states of VO_2. Thus, emitters found in the vicinity of *h-BN*/VO_2 interface have a higher probability of dipole moment oriented along the vertical direction.

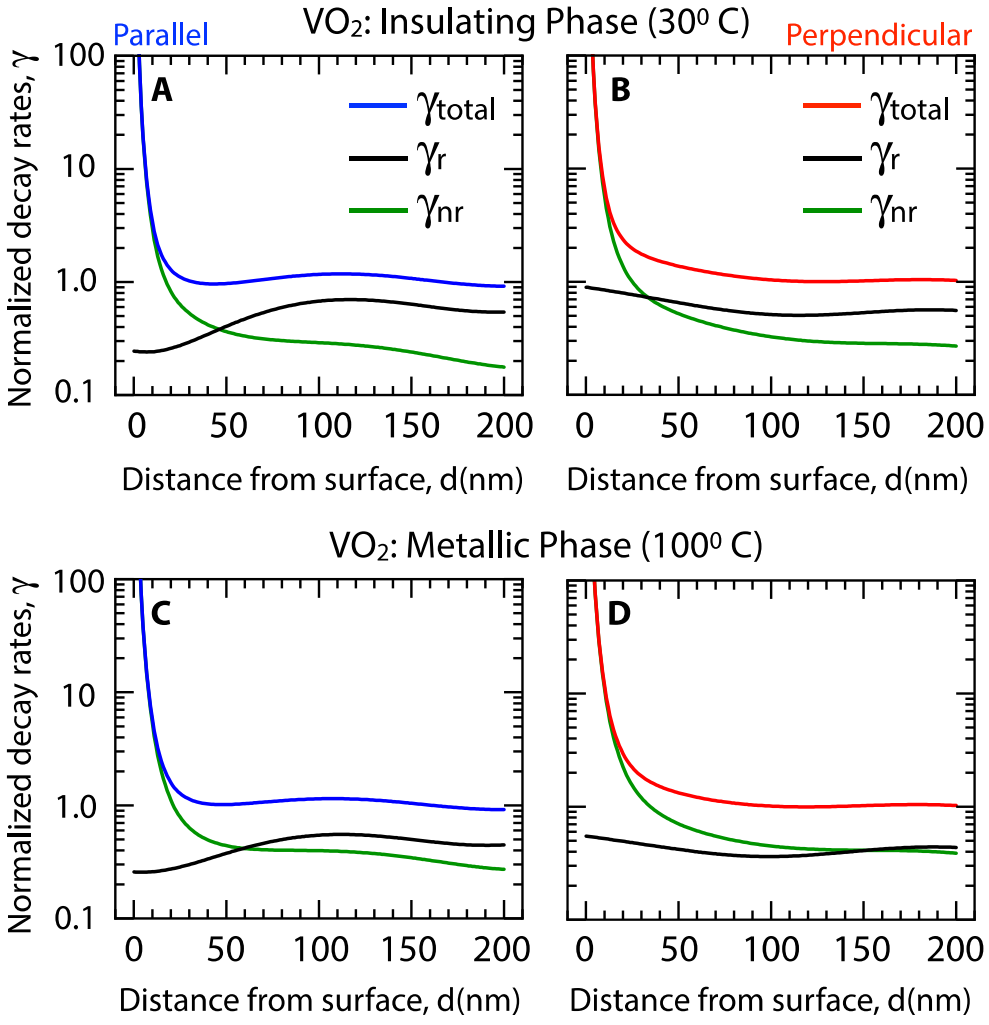

Figure 3.9. Radiative and non-radiative decay rates. Total (γ_{total}/γ_0), radiative (γ_r/γ_0), non-radiative (γ_{nr}/γ_0), rates of spontaneous emission of a quantum emitter as a function of distance from VO_2 surface for two dipole orientations, i.e., parallel (θ=90°) and perpendicular (θ=0°) to the surface. For numerical simulation we considered the emission wavelength λ_0 = 600 nm and the quantum yield QY = 0.79 corresponding to the emitter A. (a, b) Insulating phase of VO_2, (c, d) metallic phase of VO_2. Free-space decay rate $\gamma_0 = n\omega_0^3|\rho|^2/3\pi\varepsilon_0\hbar c^3$, with c being the speed of light, n the refractive index of h-BN, ω_0 the atomic transition frequency, $\hbar$ the reduced Planck's constant, and ρ the amplitude of the dipole moment vector. The refractive indices of the upper medium, h-BN, and that of sapphire were set to 1, 1.82, and 1.77, respectively. The refractive index of VO2 at 600 nm was set to 3.05 + 0.42i (insulating phase) and 2.57 + 0.64i (metallic phase) from our ellipsometry data.

3.7 Optical characterization of emitters

To perform background subtraction for $g^{(2)}$ measurements we scanned a small PL map (5μmX5μm) around each emitter in the same optical condition as the $g^{(2)}$ measurement was performed (i.e., using bandpass filter to only pass through the zero phonon line). Then by fitting a Gaussian profile to the spatial photoluminescence we extract the value of background (B) and signal(S).

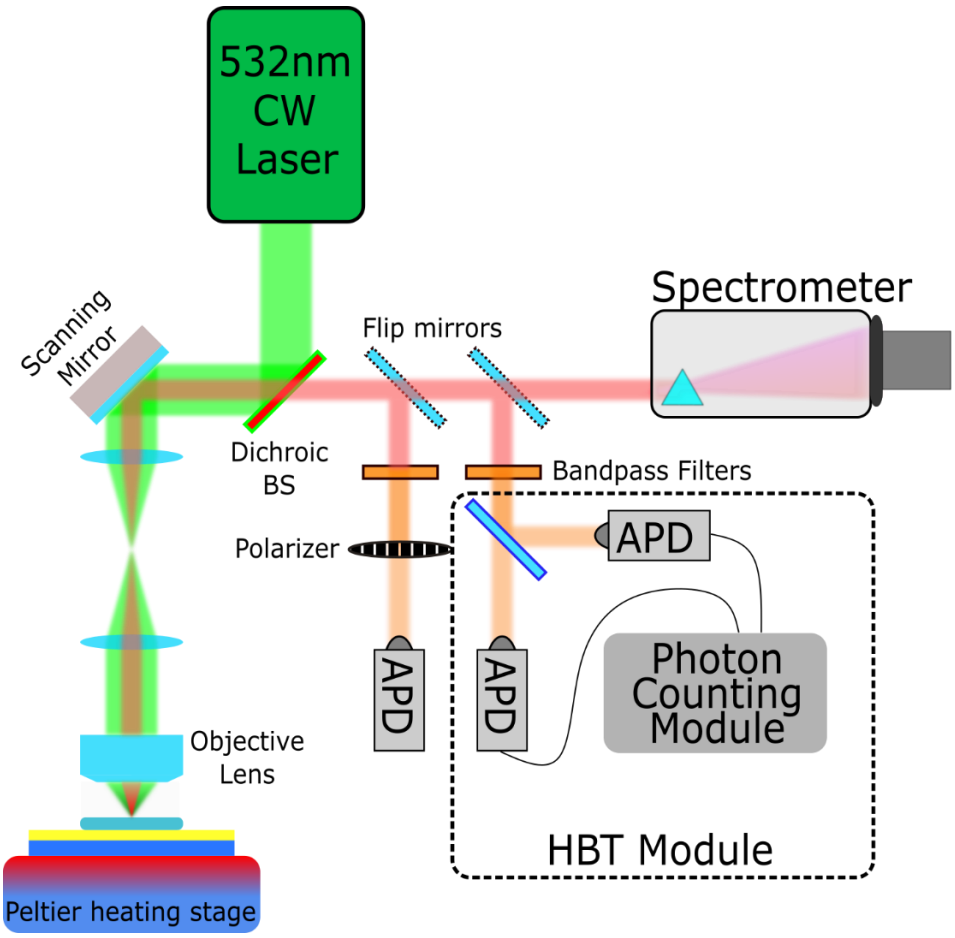

Figure 3.10. Experimental setup. Schematic of the homebuilt confocal microscope used to characterize h-BN quantum emitters, perform correlation measurements and emission polarimetry.

Then we define parameter ρ as $\rho = S/(S + B)$. If the raw (i.e., background is not corrected) $g^{(2)}$ function is $g_{raw}^{(2)}$ then the background corrected intensity autocorrelation $g_{bgc}^{(2)}$ is calculated as:

$$g^{(2)}_{bgc}(t) = \frac{g^{(2)}_{raw}(t) - (1-\rho^2)}{\rho^2}.$$

A similar method is used for background subtraction of polarization measurement. We subtracted ½ of the background value extracted from the fit mentioned above from the angle dependent polarization.

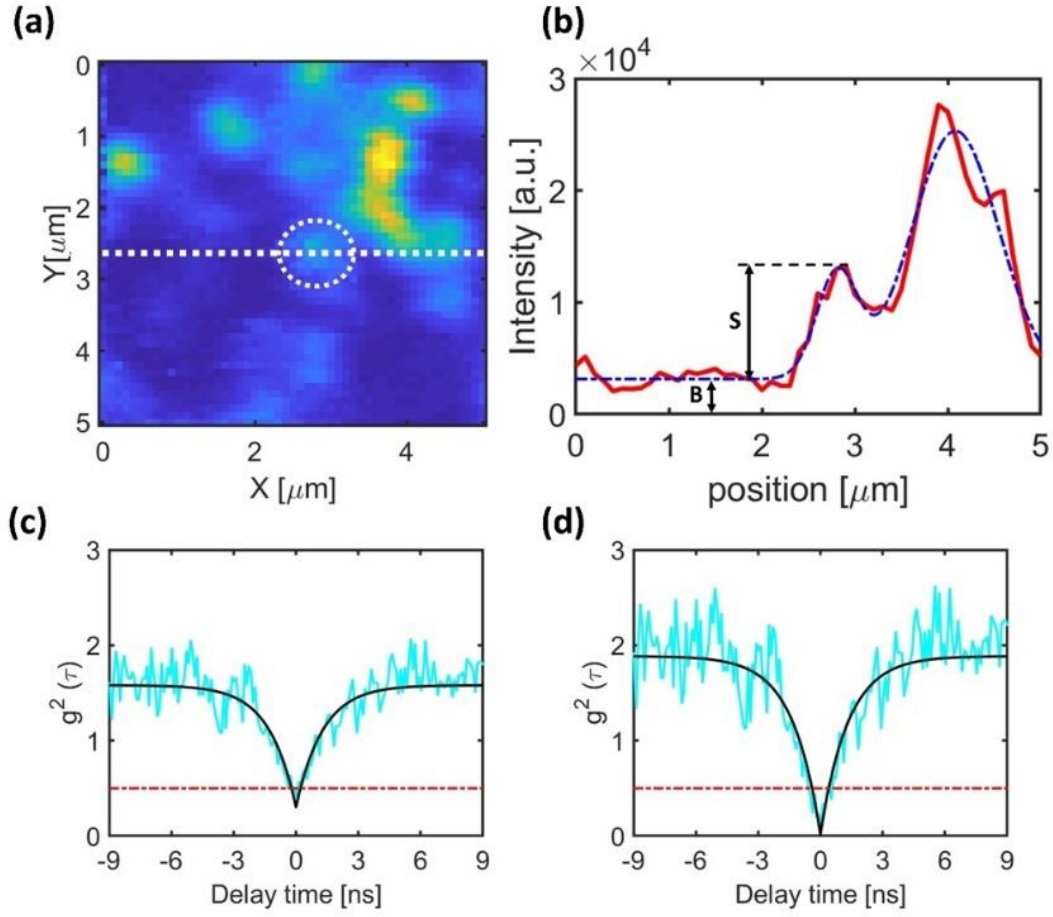

Figure 3.11. Background subtraction for correlation measurements. Background subtraction for g^2 (τ) measurement of emitter B. (a) shows a PL map around the emitter, (b) shows a profile of the PL map shown by a dashed line in (a) with

a Gaussian fit to it, and values for signal and background. (c) shows g^2 (τ) result before background subtraction and (d) shows g^2 (τ) result after background subtraction.

We also studied a bright emitter with ZPL at 570 nm however before performing polarization measurement this emitter bleached and we could not perform a complete analysis similar to emitters A and B. The full information of decay rates of three emitters under study can be seen in Table 3.1.

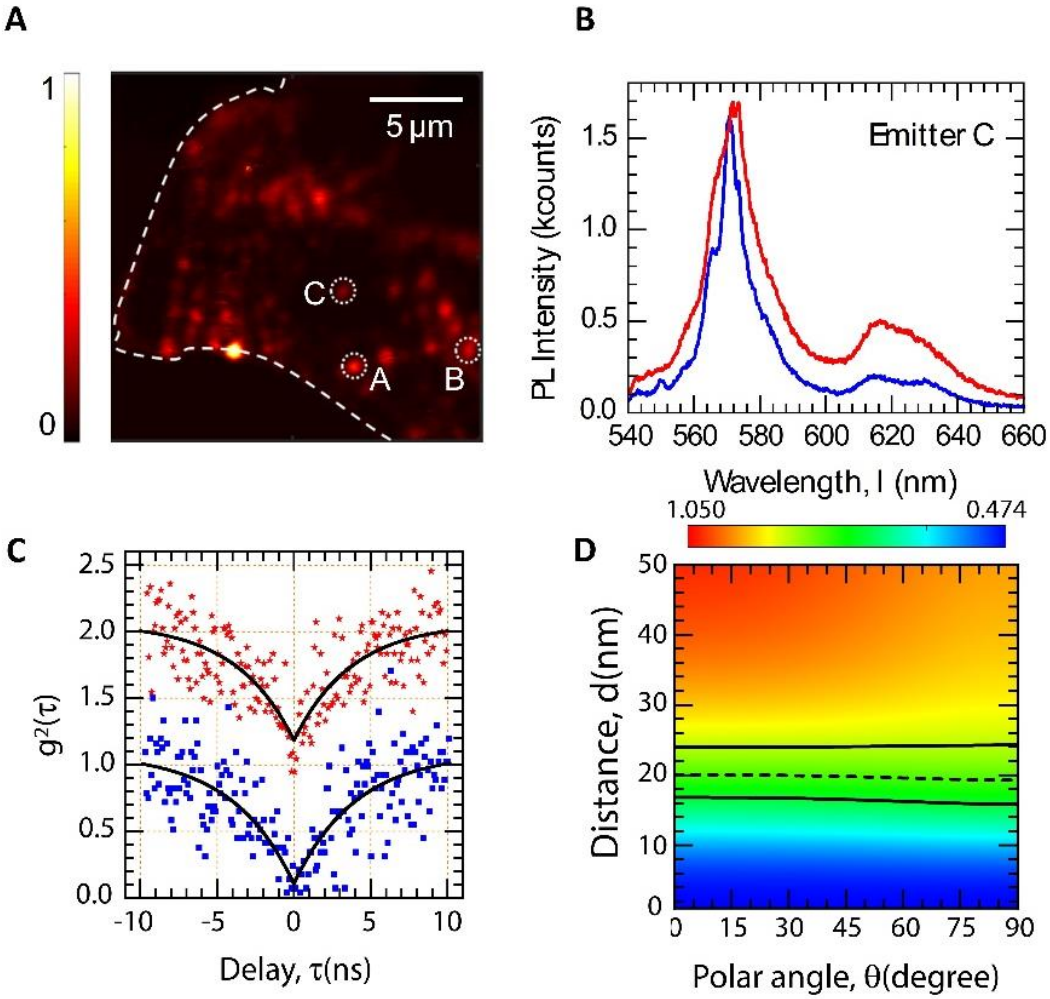

Figure 3.12. Emitter C. In (a) we can see the position of this emitter in the PL map and spectra (b) and autocorrelation measurement result (c) at 30C and 100C. By comparing the ratio of decay rates to simulations at 570 nm, we extracted the axial position of this emitter as can be seen in (d).

Emitter	Decay rate, $\gamma_{\text{Insulating}}$ (MHz)	Decay rate, γ_{Metallic} (MHz)
A	249 ± 15	304 ± 33
B	693 ± 45	865 ± 122
C	268 ± 16	334 ± 18

Table 3.1. Spontaneous emission rates of emitters. Spontaneous decay rates of the emitters A, B, and C in the vicinity of VO_2 in insulating phase and metallic phase. The decay rates are estimated based on the fitting of $g_2(\tau)$ and subtracting the contribution of pump-dependent excitation rate.

Microsecond scale autocorrelation function of three emitters at both 30 °C and 100 °C is plotted in Figure 3.13 to demonstrate how $g^{(2)}$ of all three emitters at long time scales approaches 1.

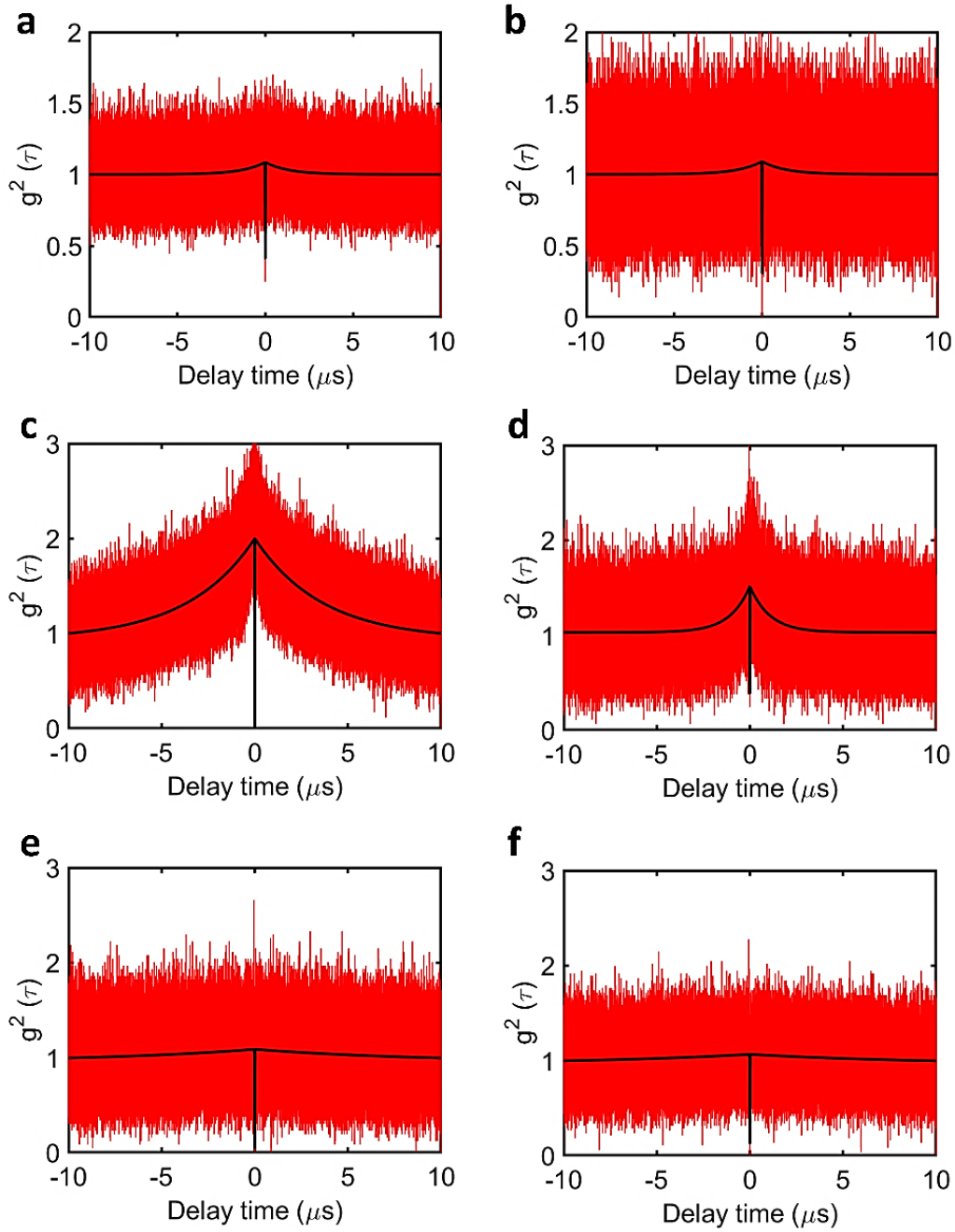
a
b
c
d
e
f
$g^2(\tau)$
Delay time (μs)
-10
-5
0
5
10
0
0.5
1
1.5
2
3

Figure 3.13. Full-scale correlation data for the emitters A, B, C. Plot of the correlation measurement for Emitters A (a,b), Emitter B (c,d) and Emitter C (e,f) as a function of delay over the range of microseconds. The data in (a,c,e) and (b,d,f) are at room temperature and 100℃, respectively.

3.8 Photophysics of *h-BN* quantum emitters

We model single *h-BN* quantum emitter as three-level system that consists of a ground state $|b\rangle$, excited state $|a\rangle$ and metastable state $|c\rangle$ as shown in Figure 3.14. The emission characteristics of this quantum emitter can be described by rate equations for population of the three levels.

$$\dot{\varrho}_{aa} = R\varrho_{bb} - (\gamma_b + \gamma_a)\varrho_{aa}$$

$$\dot{\varrho}_{cc} = \gamma_a\varrho_{aa} - \gamma_c\varrho_{cc}$$

Here, R is the rate of excitation and γ_i (with i= a, b,c) is the decay rate of population (radiative and non-radiative combined).

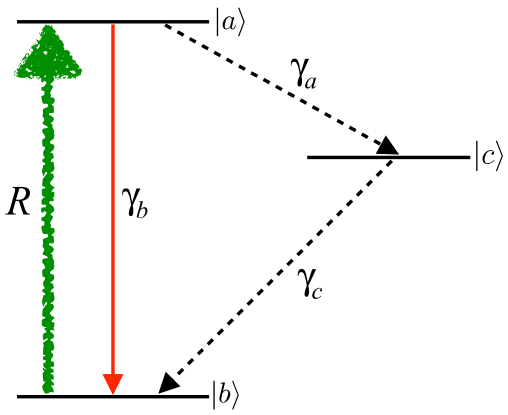

Figure 3.14. Three-level system with corresponding decay and excitation rates.

These equations are also supplemented with population conservation equation $\varrho_{aa} + \varrho_{bb} + \varrho_{cc} = 1$. Using the rate equations, one can derive the analytical expression for the normalized "ideal" second-order autocorrelation function $g^2(\tau)$ as:

$$g^2(\tau) = 1 - \left[(1+\zeta)e^{-\gamma_1|t|} - \zeta e^{-\gamma_2|t|}\right]$$

where the coefficients are given in the limit ($\gamma_b \gg \gamma_a, \gamma_c$)

$$\gamma_1 = R + \gamma_b$$

$$\gamma_2 = \gamma_c + \frac{R\gamma_a}{(R+\gamma_b)}$$

$$\zeta = \frac{R\gamma_a}{[\gamma_c(R+\gamma_b)]}.$$

However, in the presence of a background such as laser scatter or diffused photoluminescence takes a modified form:

$$g^2(\tau) = 1 - \rho^2\left[(1+\zeta)e^{-\gamma_1|\tau|} - \zeta e^{-\gamma_2|\tau|}\right]$$

where, ρ quantifies the background and $g^2(0) = 1 - \rho^2$. The decay rate of the excited state $|a\rangle$ is $\gamma_t = \gamma_a + \gamma_b \approx \gamma_b$ as the transition rate to the metastable state $|c\rangle$ is orders of magnitude smaller compared to the decay rate γ_b. From above equations we can obtain the decay rate of the quantum emitter using the pump-power-dependent decay rate γ_1 as $\gamma = \gamma_1 - R$. In our experiment, the focal spot was near diffraction limit ($\sim 0.5\,\mu m$), the average pump power was kept constant at $P_{avg} = 50\ \mu W$ for all the measurements.

The spontaneous decay γ and the absorption cross-section σ can be estimated by measuring the pump-power-dependent decay rate γ_1. Figure 3.15 (a) shows the evolution of the decay rate γ_1 as a function of excitation power at the location of the emitter after taking into account Fresnel reflections from all interfaces. From our full wave-simulation, for emitter A ($\lambda = 600\ nm$) the excitation power drops to $\tilde{P}_{avg} \cong 0.6\,P_{avg}$. From the linear fit, we obtained the spontaneous decay $\gamma = 249$ MHz by extrapolating the linear fit to zero excitation power. At excitation power $\tilde{P}_{avg} = 50\ \mu W$ and taking into account local power, the absorption rates for both emitters are $R = 9.5$ MHz and 11.9 MHz at 30 C and 100 C resptively. Compared to the pump-power-dependent decay rate γ_1 these rates are about 25-fold and 73-fold weaker for emitter A and emitter B, respectively. Thus, in our experiment, the contribution of the excitation rate R is negligible compared to the spontaneous decay rate, i.e., $\gamma \cong \gamma_1$. The absorption rate is given by $R = \sigma I/h\nu$ with absorption cross-section σ, excitation intensity I, and excitation frequency ν. Using the absorption rate $R = 9.5$ MHz at excitation power $\tilde{P}_{avg} = 30\ \mu W$ and a near diffraction limited focal spot, we estimated the absorption cross-section $\sigma \cong 9.28 \times 10^{-16}\ cm^2$. Similar absorption cross-section for *h-BN* emitters have been reported [101]. Next, we estimated the intersystem crossing rates by fitting γ_2. Here, we treated γ_a as constant and γ_c as excitation power-dependent rate of the

form $\gamma_c = \gamma_c^0 + \frac{uP}{P+v}$. From our fitting we obtained $\gamma_a = 5.84$ MHz, $\gamma_c^0 = 0.40$ MHz, u = 0.89 MHz, v = 0.05 mW.

Internal quantum yield in an important parameter for a quantum emitter which can be estimated from the value of rate coefficients and the maximum single-photon rates, i.e., the saturation count rate I_∞ as

$$I_\infty = \eta_c \eta_q \frac{\gamma_b}{1 + \gamma_a(\gamma_c^0 + u)^{-1}}.$$

Here, η_c is the collection efficiency of the experimental set up, η_q is the quantum efficiency, $\gamma_b, \gamma_a, \gamma_c^0, u$ are rate coefficients which can be obtained from power dependent de-shelving model. We fitted the power-dependent PL intensity and fitted with the function $I = I_{sat}\left(\frac{P}{P+P_{sat}}\right)$ and obtained $I_{sat} = 0.025$ MHz and $P_{sat} = 104\ \mu W$. From the rate coefficients, we obtain $\eta_c \eta_q = 5.63$ x 10^{-4}. Taking into account the collection, transmission, and coupling efficiency of the optical element of the experimental set up, the collection efficiency $\eta_c = 8.87$ x 10^{-4} which gives $\eta_q = 0.634$. The quantum efficiency η_q has contribution from the internal quantum yield, radiative Purcell enhancement, and the non-radiative loss due to ohmic loss in VO_2. Using simple algebra, we obtain

$$\frac{1}{\eta_q} = \frac{1}{\eta_l} + \frac{1}{\eta_e}\left(\frac{1}{\eta_i} - 1\right).$$

Here, η_l accounts for the rate of energy loss in VO_2, η_i is the internal quantum yield of the *h-BN* emitter, and η_e is the radiative Purcell enhancement with respect to the homogenous medium. From our full-wave simulation, we obtained $\eta_l = 0.76$, $\eta_e = 0.324$ which yield $\eta_i = 0.793$.

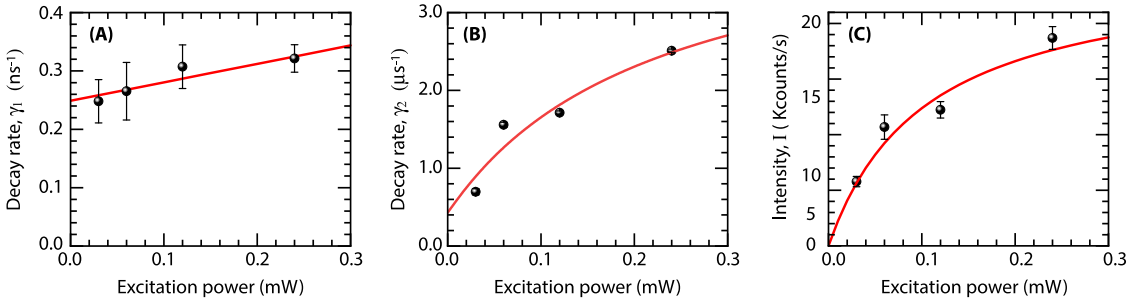

Figure 3.15. Plot of the decay rates γ_1,2 as a function of the excitation power at the location of the emitter. We fitted the experimental data shown in (a, b) with Eqs. (S4, S5), respectively. (c) Plot of the intensity as a function of excitation power to determine the saturation count rates (I_{sat}) and saturation power (P_{sat}).

3.9 Dipole orientation

Next, we focus on emission polarimetry of the quantum emitters. Previous studies [102] have shown that the three-dimensional orientation (θ, φ) of a dipole can be directly extracted by analyzing polarization characteristics of its emitted light. Figures 3.16-a, 3.16-b is the emission polarization measurement from the quantum emitters A and B, respectively. The data is fitted by the function:

$$I(\alpha) = I_{min} + (I_{max} - I_{min}) \cos^2(\alpha - \varphi)$$

where $I_{min,\ max}$ and φ are the fitting parameters. From the fit, we obtained for emitter A: $I_{min} = 0.356 \pm 0.013$, $I_{max} = 0.966 \pm 0.024$ and $\varphi = 175.7^0 \pm 1.0^0$. Similarly, for emitter B: $I_{min} = 0.318 \pm 0.034$, $I_{max} = 0.888 \pm 0.066$ and $\varphi = 109.9^0 \pm 2.9^0$. In emission polarimetry, the polar angle θ can be extracted from the degree of polarization of the emission defined as

$$\delta(\theta) = \frac{I_{max} - I_{min}}{I_{max} + I_{min}}.$$

From the fitting parameters (I_{max} , I_{min}), we obtained $\delta = 0.461 \pm 0.023$ and $\delta = 0.473 \pm 0.070$ for emitter A and B, respectively. Figures 3.16-c and 3.16-d show the calculated degree of polarization δ as a function of the polar orientation angle θ using the experimental values of numerical aperture (0.9), the refractive indices of *h-BN*, VO_2 (insulating phase) and sapphire. The distance *d* of the quantum emitters A and B from VO_2/Sapphire substrate was set to $d \sim 20$ nm. From Figures 3.16-e and 3.16-f we clearly see that variation in the distance *d* is negligible (dashed line). The red dot in Figures 3.16-e and 3.16-f represents the measured value of δ and we extract the polar orientation angle $\theta = 20.5^0 \pm 3.6^0$ and $\theta = 21.2^0 \pm 4.5^0$ for emitter A and B, respectively. In estimating the value of error in θ we accounted for the error in location *d*, which is shown Figures 3.16-e and 3.16-f by solid lines. Figure 3.16-e shows nanometer-scale axial localization of emitter A with an uncertainty (full-width) of ~ 15 nm, oriented along $(\theta, \varphi) = (20.5^0 \pm 3.6^0, 175.7^0 \pm 1.0^0)$. Similarly, Figure 3.16-f shows nanometer-scale axial localization of emitter B with an uncertainty full-width of ~ 17 nm, oriented along $(\theta, \varphi) = (21.2^0 \pm 4.5^0, 109.9^0 \pm 2.9^0)$. The strong vertical component of the dipole orientation for both emitters found in the vicinity of *h-BN*/VO_2 interface are consistent with our simulations results shown in Figure 3.9. The predominant out of plane dipole orientation of these emitters can be a result of an out of plane atomic structure of the emitter. We believe the information provided by these measurements are of fundamental value in determining the underlying atomic structure of emitters.

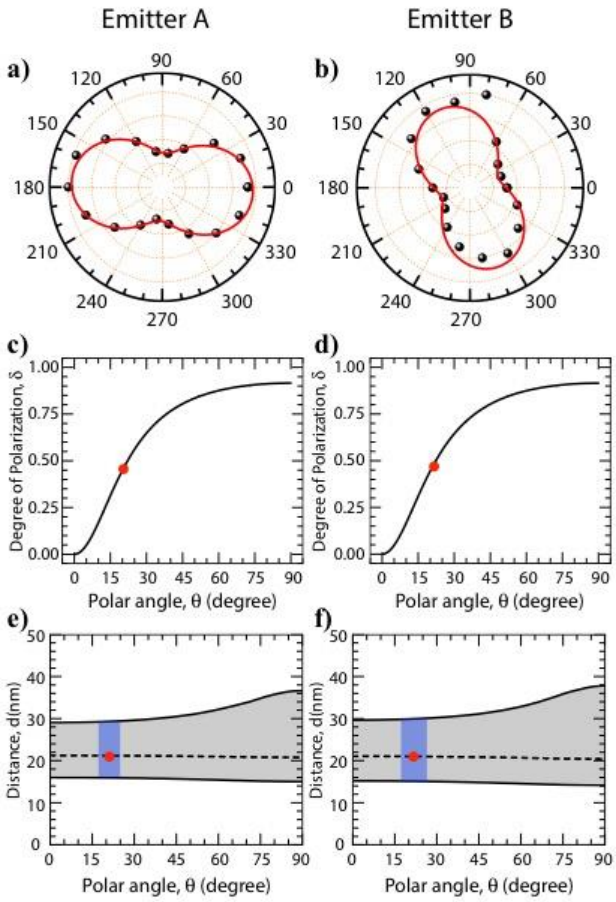

Figure 3.16. 3D-Orientation of h-BN quantum emitters and nanometric axial location. (a,b) Polar plots of the photoluminescence (PL) intensity of the emitter A and emitter B, respectively as a function of the emission polarization analysis angle (α). The PL data (solid spheres) were fitted to extract the azimuthal angle (φ) of the emitters and the degree of polarization (δ). From the fit, we deduce that for emitter A, φ=175.7°± 1.0°; δ= 0.461±0.023 and for emitter B, φ=109.9°± 2.9°; δ= 0.473±0.070. (c, d) Calculated value of degree of polarization (δ) as a function of the polar angle (θ) of the emitters located at a distance of ~ 21 nm from the surface of VO2. The red dots in (c) and (d) corresponds to the experimental value of δ obtained from (a), and (b), respectively. The extracted value of the polar angle for emitter A and B are θ = 20.5° ±3.6° and θ = 21.2° ±4.5°, respectively. (e, f) Purple shaded region shows the range of the distance (d) and the polar angle (θ) of the emitters A and B, respectively, based on our experimental data and simulations.

Next, we investigated the feasibility of transferring the *h-BN* flake from the VO_2 measurement substrate to a device substrate, which is a necessary capability for integration of quantum emitters with chip-based photonic components, waveguide circuits, and planar metamaterials [103–106]. In contrast to wet chemical transfer method [107], we utilized a polymer-assisted hot pickup technique [89,108,109] to transfer the emitter-host *h-BN* flake from VO_2 to a receiving SiO_2/Si device substrate. Figure 3.17-a, 3.17-b show the optical image of the flake before and after the transfer. We were able to relocate the emitters A and B on the device substrate by performing confocal PL mapping (Figure 3.17-c) and matching the spectral (Figure 3.17-d) and spatial signatures of both emitters before and after the transfer process. We expect that the axial position of the emitters from the bottom surface and the polar angle of their dipole orientation to remain unchanged after the transfer. However, the azimuthal angle may change. Next, we performed emission polarimetry to determine the azimuthal angle of the emitters after the transfer. Figures 3.17-d and 3.17-e show polar plots of the PL intensity of the emitter A and emitter B, respectively as a function of the emission polarization analysis angle (α). From the fitting the data, we deduce that for emitter A, $\varphi = 164.6° \pm 3.0°$ and for emitter B, $\varphi = 94.4° \pm 4.0°$. Next, we measured the relative orientation of the flake before and after the transfer. The transferred flake is oriented at an angle $\Delta\varphi = -12.6°$ with respect to its orientation on VO_2/Sapphire which indicates that the azimuthal orientation of the emitters is also preserved within experimental errors.

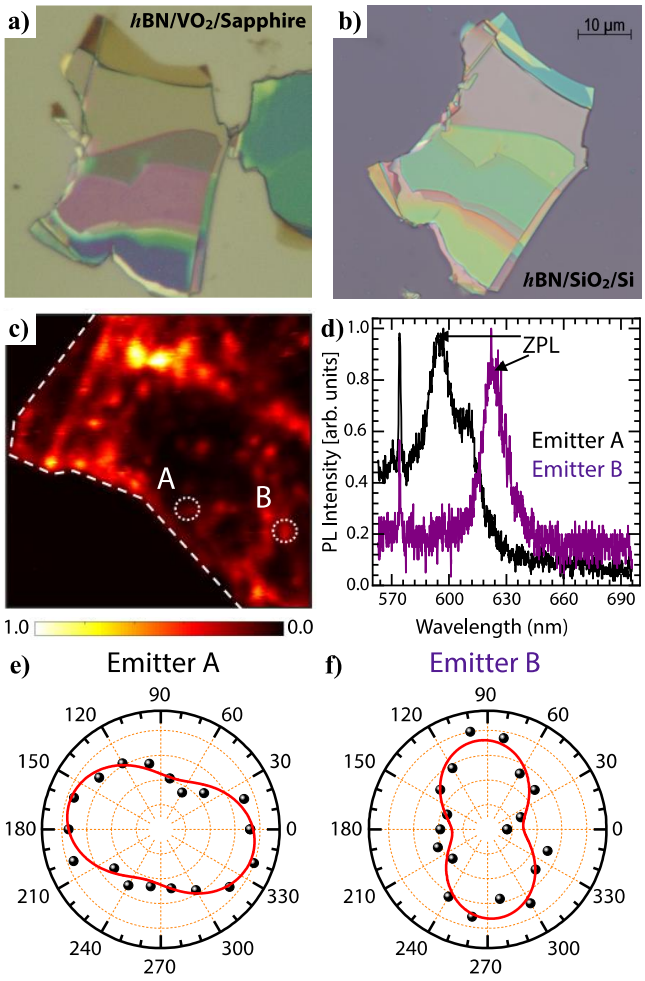

Figure 3.17. Emitter characterization. (a,b) Optical image of the flake on VO2/Sapphire substrate (before transfer) and SiO2/Si substrate (after transfer) respectively. The transferred flake is oriented at an angle $\Delta\varphi$=-12.6° with respect to its orientation on VO2/Sapphire substrate. (c) Confocal photoluminescence (PL) map of the flake on SiO2/Si substrate. Encircled (dashed white circle) highlights the region where emitters A and B are located. (d) PL spectra from the region highlighted in (c) shows the presence of emitters A and B which matched with the spectra obtained from the same location before transfer. The sharp line ~ 575 nm corresponds to Raman line of h-BN. (e,f) Polar plots of the PL intensity of the emitter A and emitter B, respectively as a function of the emission polarization analysis angle (α) on SiO2/Si substrate after the transfer. From the fit, we deduce that for emitter A, φ=164.6°± 3.0° and for emitter B, φ=94.4°± 4.0°

3.10 Experimental methods

3.10.1 Optical characterization

Optical characterization of samples was performed in a home-built confocal microscope capable of optical spectroscopy in visible range (Princeton HRS 300 system) and intensity auto-correlation measurement ($g^2(\tau)$) in a Hanbury Brown Twiss (HBT) configuration using a 50-50 beam splitter and two avalanche photo diodes (PDM Series -PicoQuant). We used a fast-scanning mirror (Newport) and a $4f$ telecentric configuration to perform photoluminescence mapping. The microscope uses a 532 nm CW laser (Cobolt) to pump emitters in *h-BN*, a 100X objective (Leica) to focus the beam on the sample and used 50 µW power of laser (before objective) for all emitters. A quarter wave plate was put in the beam path at 45^0 orientations with respect to linear polarization of laser in order to produce circularly polarized light. We pumped with circularly polarized light to excite all emitters irrespective of their in-plane dipole orientation. A tunable bandpass filter (Semrock versachrome) was used to only pass the zero-phonon line on the emitter into HBT setup to reduce background. To measure the azimuthal component of the emitter's dipole orientation we put a rotating polarizer in the detection path via a flip mirror and we rotate the polarizer from a vertical configuration with increments of 20 degrees until 340 degrees and the intensity after the polarizer is recorded with an APD. A polar plot of intensity as a function of angle is plotted (Figs. 3.16-a, 3.16-b, 3.17-e, and 3.17-f). Visibility of the polar plots were used to determine the polar component of the dipole orientation (Figs. 3.16-c and 3.16-d). Annealing in an inert environment is routinely used to create or activate quantum emitters in diamond as well as *h-BN*. For the *h-BN* samples described here, we annealed a bulk crystal of *h-BN* at 950 ℃ in a 1 bar pressure argon gas for 30 minutes

before exfoliation. We mounted our sample consisting of *h-BN*/VO_2/Sapphire on a Peltier heating stage.

3.10.2 Transfer of h-BN flake from VO_2 to SiO_2 substrate

After the completion of emitter localization in *h-BN* on VO_2, the flake can be deterministically transferred on to a different, arbitrary substrate for further studies, such as integration into resonant photonic structures like waveguides, photonic crystal cavities, DBRs, etc. The host *h-BN* flake was deterministically transferred from VO_2 on to SiO_2 using the polymer assisted hot-pickup technique. A transfer handle with a hemispherical PDMS block (to allow precise point contact and deterministic choice of flake) coated with a thin polycarbonate (PC) film was used. The flake was picked up from VO_2 between 130-140^oC (contact and pickup were both done at elevated temperatures to increase yield) and dropped onto SiO_2 at 200^oC, following which the PC film was removed by gentle chloroform and isopropanol treatment.

The polymer assisted hot pickup-based transfer technique enables an accuracy in spatial positioning on the desired substrate close to 1-2μm. In principle, it is limited by two factors — optical resolving power of the microscope used during the transfer and the micromanipulators used to position the flake with respect to the substrate. In our experiments, a 50x objective was used, which allowed us to identify feature sizes of about 1μm and a manual micromanipulator set was used which had a bidirectional repeatability of approximately 2μm. In addition, the desired substrate can be placed on a rotational stage and the host *h-BN* flake can transferred with a rotational alignment precision of about 0.1 degrees. However, in our experiment the uncertainty in rotational alignment is limited by uncertainty in the in-plane dipole moment which is about 3–5 degrees. This enables high-accuracy

angular alignment of the in-plane dipole moment of the *h-BN* flake to the desired substrate containing any nanophotonic design sensitive to dipole orientation.

In order to facilitate that we fabricated "transfer handles" as follows: A 1 cm x 1 cm x 0.5 cm block of cured PDMS was cut and put on a glass slide. Drops of uncured PDMS (Sylgard 10:1 ratio) were poured onto the block so that the PDMS assumes a hemispherical lens-like shape. This was cured overnight at 80C in an oven. The curvature of the PDMS ensured deterministic contact at the center of the lens while transferring the flakes. Polycarbonate (PC) crystals were dissolved in chloroform (6% by weight) with a magnetic stirrer overnight at 30°C. A few drops were cast on a glass slide and immediately another glass slide was pressed on it and then slid down to ensure uniform PC film on both glass slides. After 20 minutes of curing, a scotch tape with a window of opening cut out in the middle was used to pick-up the PC film and lay it on the PDMS hemi-spherical handle, thus completing the process of the "transfer handle" creation. In order to perform the deterministic transfer, the *h-BN* on VO_2 was put on a temperature controlled hot plate and heated up to 130°C.

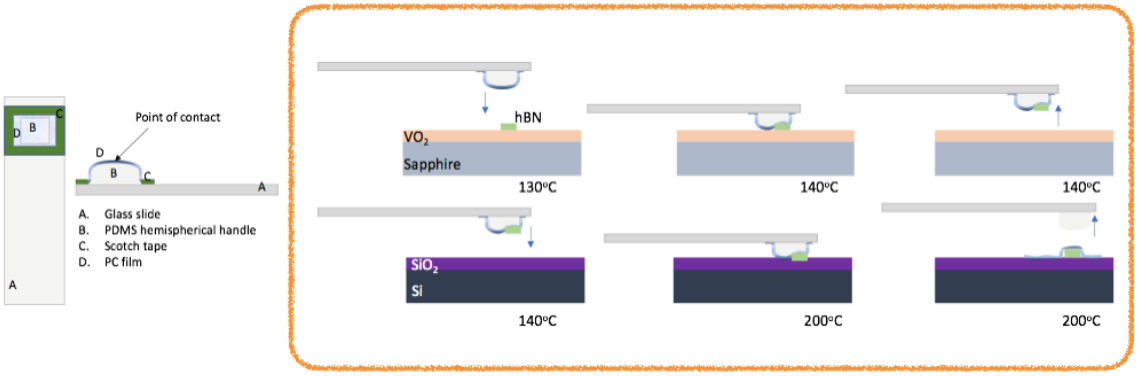

Figure 3.18. Transfer Process: Schematic of dry transfer process used to transfer our h-BN flake on VO2/Sapphire substrate to SiO2/Si substrate.

The PC/PDMS block was slowly brought in contact with the h-BN flake of interest using a micro-manipulator and the system was heated slowly up to 140^{o}C to ensure that the PC film uniformly touches the entire *h-BN* flake. At this temperature, the PC is stickier than the VO_2 and attracts the *h-BN*. Then the system is slowly retracted without lowering the temperature. As the PC film detaches from the VO_2 substrate, it lifts the *h-BN* flake of interest along with it. It should be noted that while conventionally this is achieved by lowering the temperature rather than the substrate, we found that this reduced the yield in our case because then the VO_2 is stickier than the PC at lower temperatures (<130^{o}C) and the flake does not pick up reliably. Once the *h-BN* is on PC/PDMS it can be arbitrarily placed on any substrate with a spatial accuracy of 1um, limited by our transfer setup. In order to "drop" it on to the desired substrate, we bring the h-BN flake and substrate in contact at 140^{o}C. As soon as the PC makes full contact with the substrate, the temperature is taken up to 200^{o}C and the PC melts and "drops" on the substrate. The PC film can be removed by gentle chloroform and isopropanol treatment sequentially, for 5 minutes. Our transfer process does not involve etching or usage of any harsh chemicals thus preserving the quality of the flakes and also the emitters. Also, our choice of a hemispherical handle allows us greater flexibility in deterministically picking and placing *h-BN* flakes, which greatly increases the versatility of this process over other existing methods where the entire substrate is usually etched, and all flakes are transferred to the next substrate. After successful transfer of our flake onto SiO_2/Si substrate we performed a confocal PL map of the region containing emitters A and B, to relocate the quantum emitters. We could match spectral and spatial signatures of both emitters in the *h-BN* flake after transfer onto Si/SiO_2. By comparing the PL map before and after transferring it can be observed that the spatial emission patterns before and after transfer are different which can be a result of the dependence of activation of different defect sites in *h-BN* on the substrate. This dependence can be attributed to the different optical and electrical

properties of the two substrates. The entire transfer process and relocating of the emitters is summarized in Figure 3.18.

3.11 Systematic errors and their effect on the results obtained

To determine the *axial* position of the *h-BN* emitters and the *polar* angle of their dipole orientation, we performed full-wave simulations using COMSOL Multi-Physics to calculate relative decay rate $\beta = \gamma_{Insulating}/\gamma_{Metallic}$ as a function of distance d of a quantum emitter from the surface of VO_2 when switched from the insulating to metallic state. Here, the decay rate γ depends on the optical environment, i.e., the refractive index of the surrounding medium, thickness of the multi-layered structures, uniformity, etc. In our simulations, we assumed infinitely extended substrates along X/Y directions; sapphire, VO_2, and *h-BN* constitute the multi-layered substrates with uniform thickness. We extracted the refractive index (n,k) of VO_2 by employing ellipsometry of VO_2 on sapphire substrate. The thickness of VO_2 was measured using AFM and it was set to 40 nm with the root-mean-square roughness is around 1.5 nm. Our COMSOL simulation showed that this small roughness leads to a ~1.5 % and ~1.0 % variation in the decay rate for *z*-dipole at 30 C and 100 C, respectively, at the location of the emitter. With the QY of the emitter ~ 0.8, this error propagates to an error of 1.2 % in the relative decay rate β. For *x*-dipole similar analysis yielded an error of 0.2 %. Next, we considered uncertainty in the thickness of *h-BN* with variation up to 10 nm. For this case we obtained an error of ~ 0.1 % and 0.2 % in the relative decay rate β for *z*-dipole and *x*-dipole, respectively. These results suggested that our results are minimally affected by these variations. In our simulation, we set the refractive index of *h-BN* to be 1.82 at 600 nm, and a weak linear variation was employed to calculate refractive index at 570 nm and 620 nm as 1.84 and 1.81, respectively. However, some variation in *h-BN* refractive index has been reported in both CVD grown as well as exfoliated samples. To

quantify the error in β due to uncertainty in the refractive index of *h-BN*, we considered the value of *h-BN* refractive index up to 1.90. Our simulation showed that even this large uncertainty, the error in β is ~ 4.1 % and 6.6 % for *x*-dipole and *z*-dipole, respectively. One of the parameters which strongly influenced the decay rate calculations and β is the quantum yield (QY) of the *h-BN* quantum emitters. It has been reported that *h-BN* color centers exhibit QY in the range 0.6 ~ 1.0 [39,41]. We used this range to quantify the errors (shown in Figure 3.1-b). To eliminate this systematic error, we directly extracted the QY for our emitter(s).

3.12 Summary and conclusions

To summarize, we have demonstrated an experimental technique by which the axial position of quantum emitters in a multi-layered *h-BN* flake can be extracted with nanometer-scale accuracy by exploiting the modification of photonic density of states using a phase change optical material, VO_2. Here, we tailor the optical environment of an emitter in the vicinity of VO_2/Sapphire substrate which generates a sharply distance-dependent PL response. By performing time-resolved fluorescence spectroscopy, supplemented with emission polarimetry, several specific quantum emitters were identified at an axial distance of ~ 21 nm from the *h-BN*/VO_2 interface while also determining their full dipolar orientation (θ, φ). Although, in this work, we focused on locating *h-BN* quantum emitters with ZPL in the wavelength range ~ 550–640 nm, presence of other emitters with ZPL outside this range as well as embedded further deeper in the flakes cannot be ruled out. Next, we utilized a polymer-assisted hot pickup technique to transfer the identified *h-BN* emitters from a VO_2 measurement substrate to a SiO_2/Si device substrate, which opens the door to coupling of fully characterized emitters, where each emitter has undergone precise measurement of axial position and orientation. It is worth noting that any phase-change material which experiences a sharp change in optical properties would be suitable for this purpose. However, VO_2 is particularly interesting because its insulator-to-metal transition

happens near room temperature and is thus well suited to dynamically control emission rates of quantum emitters near room temperature. Owing to the broadband nature of change in the dielectric function of VO_2 when switched from the insulating to metallic phase, our technique could also be extended to locating other visible or infrared quantum emitters. Moving forward, characterizing, and controlling the spectral diffusion of our localized *h-BN* quantum emitters for generating identical photons would constitute an interesting direction for future research.

Chapter 4. Stark tuning and linewidth control of h-BN emitters by electrostatic field

4.1 Abstract

Color centered-based single-photon emitters in h-BN have shown promising photophysical properties as sources for quantum light emission. Despite significant advances towards such a goal, achieving lifetime-limited quantum light emission in h-BN has proven to be challenging, primarily due to various broadening mechanisms including spectral diffusion. Here, we propose and experimentally demonstrate suppression of spectral diffusion by applying an electrostatic field. We observe both Stark shift tuning of the resonant emission wavelength, and emission linewidth reduction (down to 89MHz) nearly to the homogeneously broadened lifetime limit. Lastly, we find a cubic dependence of the linewidth with respect to temperature at the homogeneous broadening regime. Our results suggest that field tuning in electrostatically gated heterostructures is promising as an approach to control the emission characteristics of h-BN color centers, removing spectral diffusion and providing the energy tunability necessary for integrate of quantum light emission in nanophotonic architectures.

4.2 Introduction

Hexagonal boron nitride (h-BN) is a van der Waals material with a large band gap of ~6 eV. It has played a pivotal role in the development of 2D materials-based devices as an excellent gate dielectric and atomically smooth substrate [110,111]. This material also hosts single-photon emitters in the visible range of the electromagnetic spectrum [2,112]. Color centers in h-BN exhibit high stability at room temperatures and above [19,24], as well as high

Debye-Waller factors [19,49,113], and potentially complete mechanical decoupling of the emitter from vibrations of the lattice [25,114]. The atomistic picture of the origin of these emitters is still under debate, [20,22,46,87] but the role of carbon in the formation of emitters at visible range of spectrum has been established [21]. Optically driven magnetic resonance of ensemble [50,115] and single [116] emitters in h-BN shows these spins can be magnetically addressed, useful for sensing and quantum computation applications.

Control of many quantum optical processes requires a source of spectrally indistinguishable photons [4,32]. Thus narrow, ideally lifetime limited emission linewidth is therefore a crucial issue for such applications. While color center point defects in h-BN are robust and bright sources of single photons even at room temperature, the emission spectrum is typically strongly affected by various broadening mechanisms. Previous studies have identified spectral diffusion as one of the major broadening for h-BN single-photon sources, even at cryogenic temperatures [57,60,88,117]. Spectral diffusion corresponds to rapid fluctuations in the energy of the emitter which manifests itself as rapid movement of narrow homogeneously broadened spectral lines. As a result, the observed line profile is a convolution of the homogenously broadened spectral line and inhomogeneous spectral diffusion driven broadening. ($\gamma = \gamma_{hom} + \gamma_{inhom}$) The homogenously broadened linewidth depends on the lifetime and dephasing processes ($\gamma_{hom} = \frac{1}{2\pi T_1} + \frac{1}{\pi T_2^*}$). Here, T_1 is the decay lifetime of the emitter and T_2^* is the pure dephasing time scale which can result from spin-bath and/or emitter-phonon interactions. When the single-photon emission is purely lifetime limited, the inhomogeneous broadening is eliminated and the pure dephasing contribution to the homogeneous linewidth is zero, so the lifetime limit of the linewidth is $\frac{1}{2\pi T1}$.

While the microscopic origin of spectral diffusion broadening is still under debate, there is growing consensus that itinerant localized charges are a source of time-dependent electric

fields in the emitter environment, which modulates the dipole overlap wavefunction leading to spectral diffusion. Photoionization of nearby impurities [38,60], charging and discharging of nearby charge traps [38,60], and presence of mobile charged impurities [57] are some potential sources of these localized charges. The time scale of spectral diffusion can range from microseconds [57] to milliseconds [60,117] to even seconds and minutes, depending on the dominant source of fluctuating environmental and stray fields [118]. Also, the dependence of spectral diffusion on pump power [117] supports the idea that the charges responsible for spectral diffusion can be photo-activated. So far, several studies have attempted different methods to suppress spectral diffusion in h-BN: for example, one study used anti-Stokes excitation to stabilize the spectral line [118], but linewidth narrowing was not studied. Another study used transparent conducting substrates and reduced the inhomogeneous linewidth by 45% [88] but the resulting linewidth narrowing is still far from the lifetime limit. Another study showed that by combining a resonant excitation and lowering the excitation power, the effect of spectral diffusion was reduced [117]. In quantum dot single emitters, use of electric field for charge depletion is established as a method to increase indistinguishability of the emitter [33].

In this report, we present a new method to suppress spectral diffusion of an h-BN emitter and narrow the linewidth by nearly two orders of magnitude, approaching the lifetime limit of the emitter linewidth. To achieve this goal, we apply an out of plane electrostatic field to an emitter in h-BN and study its absorption spectra via photoluminescence excitation (PLE) spectroscopy.

4.3 Effect of DC electric field on h-BN emitters

For this experiment, an h-BN emitter with a zero-phonon line (ZPL) at 573 nm is studied. The emitter is induced in h-BN by the carbon doping method explained in the methods

section; a Voigt fit to the line shape reveals a ZPL linewidth of 0.90 meV at 6.5 K, which is higher than the average linewidth at cryogenic temperatures for emitters in thick exfoliated h-BN flakes [88], suggesting a significant broadening due to spectral diffusion.

The emitter is placed inside an all van der Waals device consisting of few-layer graphene electrodes and an additional buffer h-BN layer to prevent electrical shorting between the two electrodes as shown in Figure 4.1-b. Second-order intensity autocorrelation experiment shows a $g^{(2)}(0)=0.14$ indicating single-photon emission, while time resolved photoluminescence measurement reveals a decay lifetime of 3.36ns which corresponds to 47 MHz lifetime limited linewidth. The sample is cooled down to 6.5K and the photoluminescence (PL) of the emitter is studied at voltages from -10V to 10V at steps of 1 V, under 532 nm excitation. As can be seen in Fig. 4.1-e, the Stark effect produces a linear change in the energy of the ZPL, which suggests a non-zero out of plane dipole moment. The slope of peak position as a function of voltage in both PL and PLE measurements correspond to a value of 2.7 meV/(V/nm), considering the 29.6 nm thickness of h-BN.

In other studies, a Stark tunability of 43 meV/(V/nm) [27] for in-plane electric field, and 2.5-15 meV/(V/nm) [28] for out of plane electric field is observed for h-BN emitters. Comparing with our result and assuming the dipole moment of different h-BN emitters to be comparable, we conclude that our emitter should be mainly in-plane with a small out of plane component. Polarization measurement of the emitter also shows a linearly polarized emission in accord with a small out of plane dipole.

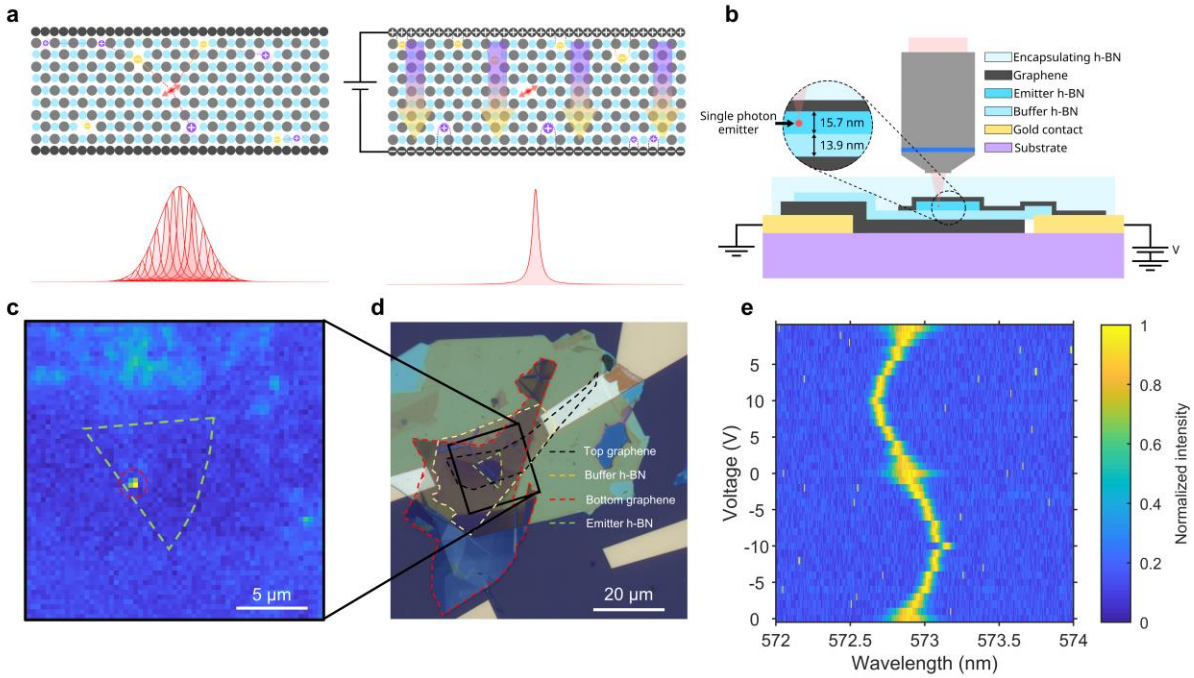

Figure 4.1. Effect of electric field on photoluminescence. (a) Schematic of the effect of electrostatic field on the single-photon emitter, top panels show the emitter located in the h-BN crystal with and without the electric field and the bottom panels show the emission spectra. Electric field locks charges located near the surface of h-BN at their place and reduces spectral diffusion. (b) Schematic of the device consisting of top and bottom graphene contacts, h-BN contatining emitter (shown as the red dot) and buffer h-BN. (c) PL map of the region containing the emitter. Each pixel is the integrated spectra from 570nm to 575nm. (d) Microscope image of the device flake edges are marked with dashed lines show location of top and bottom graphene and buffer and emitter h-BN. (e) Normalized photoluminescence spectra of emitter ZPL at T=6.5K at voltages ranging form -10V to 10 V. D. PL map of the device, the white circle shows emitter's position.

More notably we see the linewidth narrowing as the voltage increases even in the non-resonant excitation regime (PL measurements). As the absolute value of voltage increases the linewidth approaches the limits of spectrometer resolution equal to 0.2 meV. We note that as the emitter undergoes several cycles of voltage tuning the broadening at 0V remains unchanged suggesting negligible hysteresis in this process. This lack of hysteresis reveals

that the charges responsible for spectral diffusion are not permanently removed/screened by the electric field. This supports the idea that generation and recombination of the charges responsible for spectral diffusion is a dynamic process, without long-term charge trapping, and that this dynamic process can be negated at high enough electrostatic field. This effect might be caused by the excitation laser, charging the surrounding dark defects, or mobilizing the charges in the surrounding of the emitter.

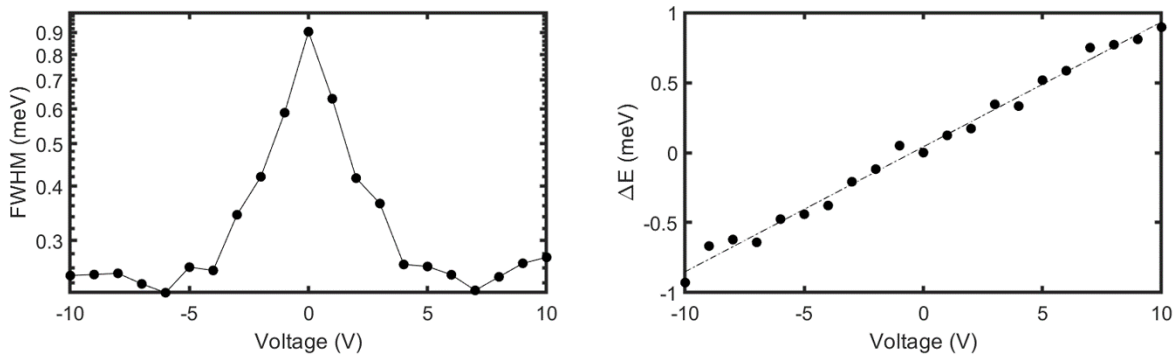

Figure 4.2. FWHM and shift of ZPL peak extracted from PL measurement.

In Figure 4.2 the result of the fits to Figure 4.1-e is shown. The FWHM shows increase as voltage approaches zero and at high voltages (V>5V) the FWHM hits the limit of spectrometer (~0.2nm @ 573nm). Linear fit to the peak shift Vs voltage shows the same value as PLE of 0.09 meV/V. Furthermore, in Figure 4.3 the integrated intensity of the emitter Vs. voltage is plotted, this plot does not show a significant dependence of Integrated PL on the voltage which shows a lack of charge state variation in this emitter across the voltages studied.

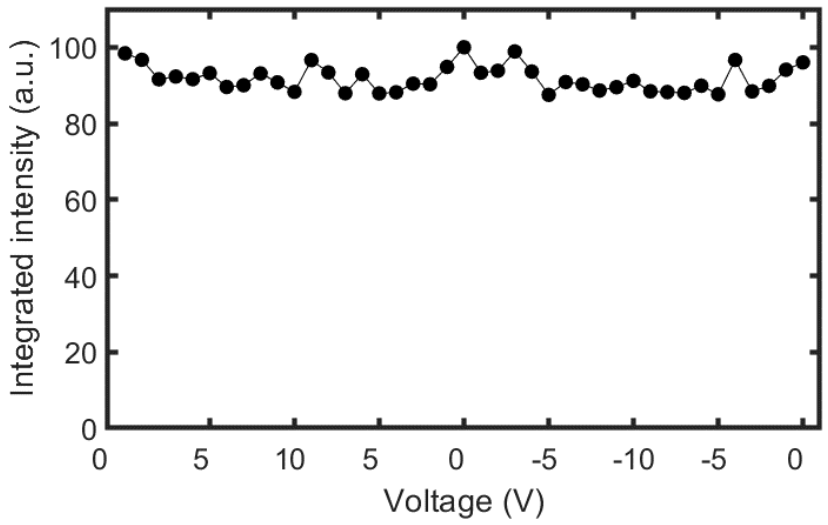

Figure 4.3. Integrated intensity of PL Vs Voltage applied to electrodes.

4.4 Study of linewidth with photoluminescence spectroscopy

To further study the effect of electrostatic fields, without the limitations imposed by the resolution of grating-based spectroscopy and non-resonant excitation, we performed photoluminescence excitation spectroscopy (PLE) experiments using a continuous wave, tunable, narrow linewidth laser source. In PLE experiment, a tunable source of CW laser excitation is slowly scanned across the zero-phonon line and the intensity of the phonon sideband is measured as a function of laser detuning. As a result, this method can measure the absorption spectra of ZPL with a resolution approaching the linewidth of the scanning laser source (~100 kHz).

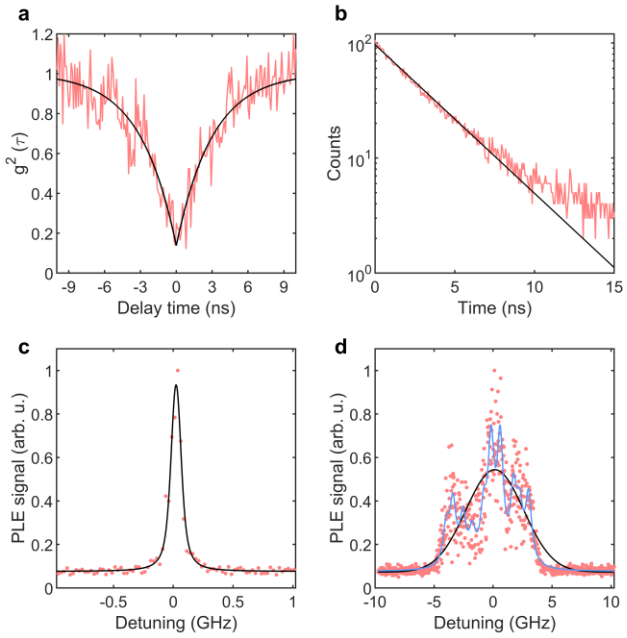

Figure 4.4. Emitter characterization and near lifetime limited PLE. (a) Second order autocorrelation function for photon emission. The fit has a value of 0.14 at τ=0. (b) Time resolved photoluminescence of the emitter. The solid line corresponds to single exponential fit with time constant of 3.36ns this value corresponds to lifetime limited broadening of 47 MHz. The deviation of data from fit at t>10ns is a result of hitting the noise floor of the photodetector. (c) Normalized cryogenic (T=6.5K) PLE spectrum of the emitter at V=10V shows linewidth of 89 MHz. (d) At V=0V PL E spectra shows multiple peaks. The blue trace shows a fit with 10 Voigt functions with the same line shape as part (c), the black trace shows a single Voigt fit to assign a FWHM value equal to 8.5 GHz.

As shown in Figure 4.4, a two orders of magnitude reduction in linewidth is observed with the application of an electrostatic field, almost completely removing the inhomogeneous broadening effects at V=10V with a fitted linewidth of 89 MHz as shown in Figure 4.4-c. The difference between the lifetime limit of 47 MHz and the measured value for linewidth can have several possible explanations. One possible origin of this difference can be residual spectral diffusion, while the electric field has suppressed most of the effect of local charges

that impose spectral diffusion, it is possible that some local charge dynamic still exists and the energy barrier to suppress these fluctuations are larger than the energy provided by the electric field. A more likely source of broadening can be dephasing processes. In such a case the observed linewidth will be limited by the total decoherence time scale consisting of lifetime and dephasing time scales. The source of this dephasing can be lattice vibrations, in which case a further reduction of the temperature can help to close the gap and achieve lifetime limited emission.

In Figure 4.5 several scans of PLE at V=0V are shown. The variation of these PLE scans clearly shows the effect of spectral jumps on the line profile at V=0V.

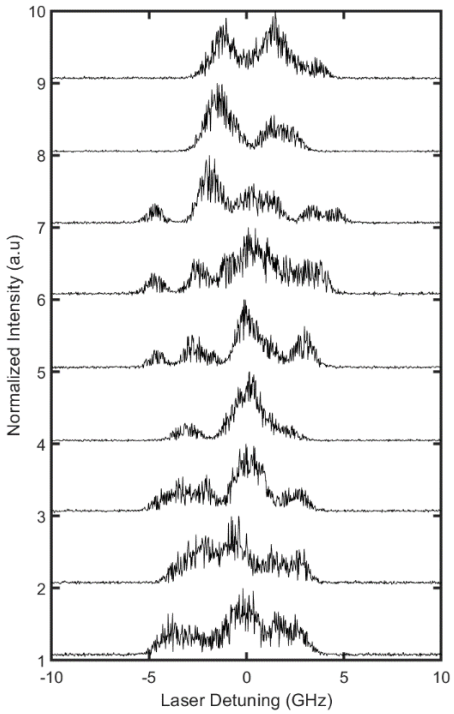

Figure 4.5. 9 PLE scans of the ZPL at V=0 and T=6.5K. The difference in the scans are originated by the difference in the local charges and their fluctuations.

The line shape of emitter at V=0V and voltages near zero exhibits several peaks. This behavior is expected from spectral diffusion broadening as it is caused by the spectral line jumping between several different energies. As PLE itself has a time scale comparable to the time for only few jumps, the PLE spectrum does not show a single wide peak. The result of fitting with sum of 10 Voigt functions to V=0V data can be seen in Fig 4.4-d. This behavior makes it challenging to assign a value for FWHM. So, we decided to assign a FWHM to these peaks by simply fitting a single Voigt function to the data and report the FWHM of the fitted peak. Even though this method does not capture the full complexity of the spectrum, it

is effective in distinguishing between narrow and wide spectra and assigning a value for FWHM. Atomic origins of this linewidth narrowing is not very clear as the atomic structure of the emitters are still under debate, we attribute the origin of the linewidth narrowing broadly to the changes in the local electronic charge fluctuations in the vicinity of the emitter. By applying an electric field, the charges in the h-BN are interacting with the DC electric field and this interaction can cause fewer fluctuations of local charges, this concept is depicted in Figure 4.1-a.

It is worth noting that in recent studies on the effect of electrostatic field on h-BN emitters, [119,120] it has been observed that the emitter charge state can be modulated because of electrostatic doping, such that the emitter can switch between optically dark and bright states. However, we do not observe such an effect here. We suggest that for emitters close to the h-BN surface, application of voltage induces electron tunneling through the h-BN barrier, thus populating, and depopulating the emitter states in the near-surface region (within a few monolayers), effectively modulating the optical transitions from off to on. In the present work, a second h-BN layer was added to prevent electrical shorting between the two electrodes, and another consequence of this layer configuration is that it prevented electron tunneling, since the emitter is not in close contact with the electrodes. Our results suggest that the emitter is not within a tunnelling distance from the top electrode, implying also that it is closer to the bottom of the flake. The spatial distribution of h-BN emitters has not been very well studied, although several reports asserted that emitters are mostly located in the vicinity of edges of the flake [47,51]. Also, one study on axial location of emitters in h-BN has shown them to be close to the surface of a 300nm thick flake of h-BN [121]. So, it is possible that in most cases the emitters are either located near the surface or close to edges of the flake, which supports our understanding of both the recent studies cited, as well as this

work. This phenomenon is possibly related to the microscopic effects of exfoliation and emitter generation.

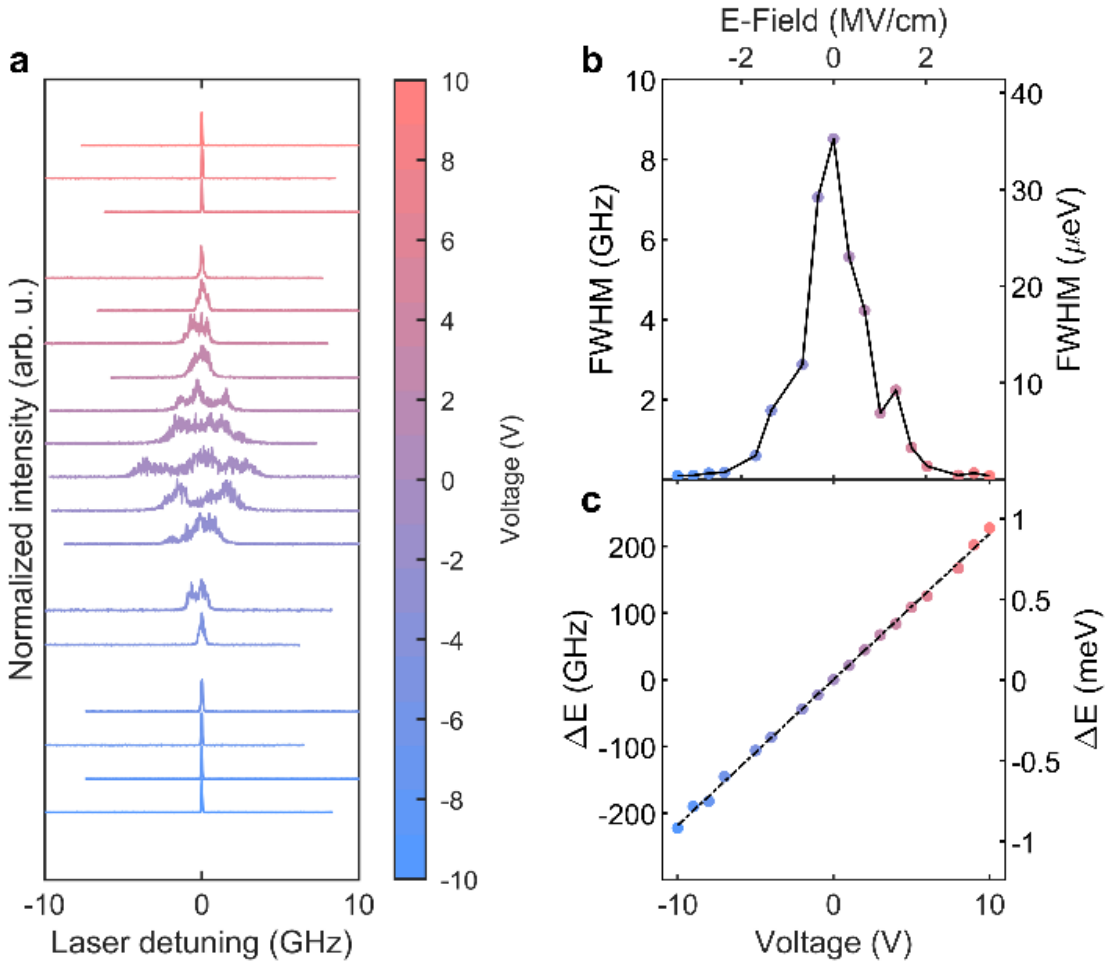

Figure 4.6. Effect of DC electric field on PLE. (a) PLE spectra of emitter at T=6.5 K for applied voltages ranging from -10V to 10V. (b) Full Width at Half Maximum (FWHM) of the peaks determined with a Voigt profile fit as a function of applied voltage, the minimum linewidth of 89MHz is achieved. (c) Measured peak position of the emitter relative to its peak position at 0V as a function of applied voltage.

4.5 Effect of temperature on the linewidth

The effect of temperature on linewidth has been discussed elsewhere [60,88,117] but the linewidth is usually convoluted with inhomogeneous broadening, so the pure effect of temperature on the emitter has been difficult to study independently from the effect of spectral diffusion. Since the electric field can suppress the contribution of the inhomogeneous broadening mechanisms on linewidth, we leveraged this opportunity to study the homogenously broadened linewidth of the h-BN emitter and the effect of temperature on it. We observed a power law increase in the linewidth as temperature increases, with exponent n=3.02 suggesting a T^3 dependence of homogeneous linewidth on temperature. This result is in accordance with some earlier studies on h-BN emitters. [60] However, some other studies have shown a linear dependence [88] or a combination of linear and cubic, $AT+BT^3$, [117] dependence of linewidth on temperature. By carefully examining the results of these studies and comparing it with our results, we noticed that the study which used emitters with a strong spectral diffusion effect shows linear dependence [88], and the study which had low temperature linewidth of 1 GHz, exhibits $AT+BT^3$ dependence of linewidth on temperature, with the linear part dominant below 20K [117]. Comparing the results of these studies to our work, in which spectral diffusion is almost completely suppressed, leads us to conclude that spectral diffusion in h-BN is also activated by thermal fluctuations and exhibit a linear variation with temperature, but purely phononic linewidth broadening effects in h-BN result in a T^3 dependence of linewidth on temperature. This is in contrast with diamond emitters which show no dependence of spectral diffusion on temperature below 20K [58].

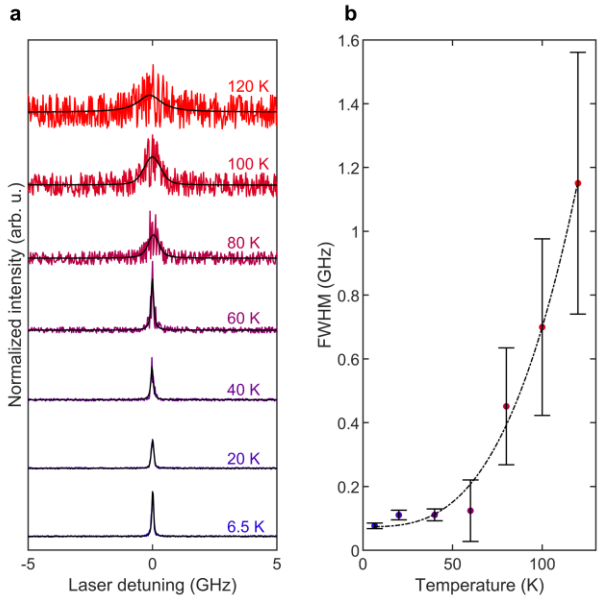

Figure 4.7. Effect of temperature on PLE. (a) PLE traces of the emitter at V=10V for various temperatures. (b) Fitted value of FWHM of the peaks as a function of temperature with a power law fit (FWHM=ATn+C) with a best fit value of n=3.02±0.51, error bars correspond to 95% confidence interval of the fitted values, and the minimum linewidth is 89MHz at 6.5K.

A T^3 dependence of linewidth on temperature is also observed in diamond nitrogen-vacancy (NV) centers [38]. In the case of NV centers, one possible explanation of the T^3 dependence is the fluctuating field created as phonons modulate the distance between the emitter and other defects and impurities, and as a result this type of dependence is mostly observed in samples with high disorder [122]. Our results suggest that this phenomenon is also present in h-BN. The surface of 2D flakes of h-BN is more prone to defects and the emitters in thin layers of h-BN are always close to surface, which can make this the dominant effect in h-BN. This is also in accordance with large spectral diffusion at 0V observed in our study, pointing to the existence of a very defective environment. This argument suggests that in an

ideal case in which spectral diffusion is fully suppressed and the defects to modulate local phonons are non-existent, it is possible to have a minimal effect of temperature on linewidth as reported elsewhere [25].

We have fitted the PLE scans at V=10V for the temperature range of T=6.5K to T=120K with Voigt fits to extract the Gaussian and Lorentzian contribution of each PLE spectra. Since thermal broadening is a homogeneous broadening mechanism, it will keep a Lorentzian profile and spectral diffusion will exhibit a Gaussian linewidth and the total line profile will be a convolution of Gaussian and Lorentzian which is a Voigt profile. Our results in Figure 4.8 shows that for T>20K the Gaussian contribution is basically insignificant to the extent that our fitting method returns zero value for Gaussian FWHM. The Gaussian FWHM is only significant at T=6.5K and T=20K which can mean there is a small residual spectral diffusion at these low temperatures however the general trend of FWHM Vs temperature is set by the Lorentzian part and the T^3 dependence of inhomogeneous linewidth on temperature is deduced from this result.

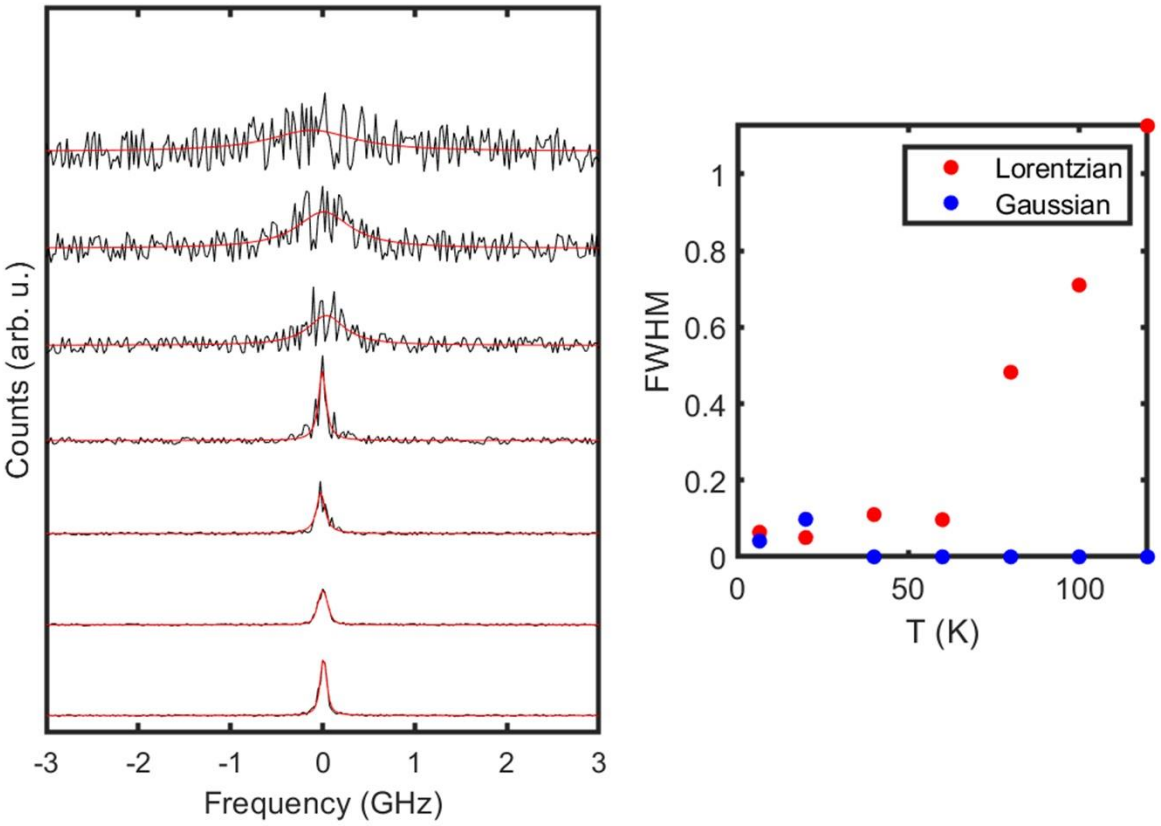

Figure 4.8. The left panel shows Voigt Fit (red) to the PLE data (black) traces for temperatures from 6.5K (bottom) to 120K (top), the right panel shows the fitted values for the Lorentzian and Gaussian FWHM (GHz) extracted from the Voigt fit.

4.6 Reproducibility of results

To check the reproducibility of our findings we have fabricated a second device with the same geometry. For an emitter with ZPL=585nm we have been able to reproduce the same

results, for this device based on the higher thickness of buffer h-BN we applied voltages up to 30V in both directions.

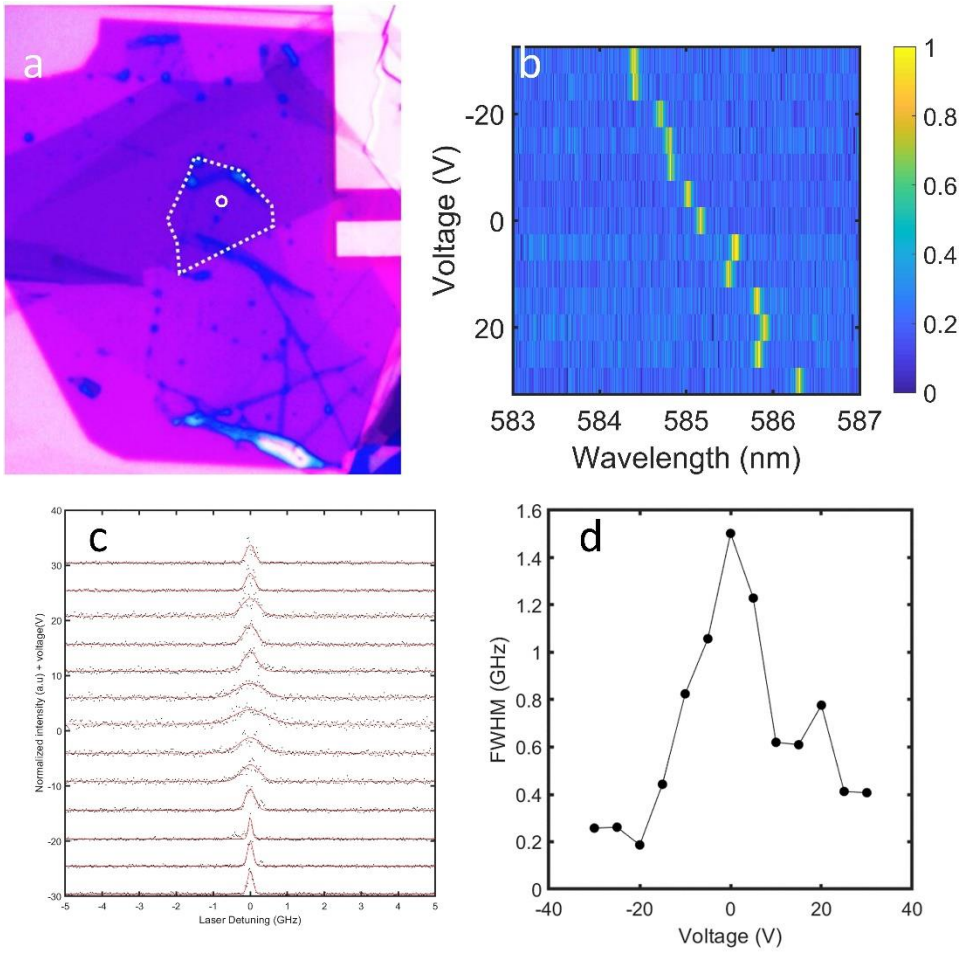

Figure 4.9. Optical microscope image of the device, the white dashed line shows the active region of the device containing all 4 layers of top graphene, emitter h-BN, buffer h-BN and bottom graphene, the white circle shows the location of the emitter. b) PL traces of the emitter at voltages ranging from -30V to 30V, this emitter does not show a significant variation of PL linewidth and the linewidth is limited by the spectrometer resolution limit. c) PLE traces of the emitter at voltages ranging from -30V to 30V, d) effective FWHM of the PLE as a function of voltage with a minimum linewidth of 187 MHz at V=-20V.

This emitter shows linewidth reduction from 1.50 GHz at V=0 to 187GHz at V=-20V.

4.7 Experimental methods

4.7.1 Emitter preparation

The emitter was prepared by annealing an h-BN crystal (HQ graphene) in between two carbon tablets (MSE supplies Carbon sputtering target >99.99% pure) at 1200C for 10 hours. Then, the h-BN crystal was exfoliated with Scotch tape onto a silicon oxide on silicon substrate. The exfoliated h-BN flake is 13.9 nm thick, and an emitter is identified with a ZPL at 573 nm. This flake containing emitter is used in a device to produce a graphene-h-BN-buffer h-BN-graphene structure.

4.7.2 Device fabrication

Graphene and buffer h-BN were directly exfoliated onto SiO_2 (285 nm)/Si substrate and identified via their optical contrast. Substrates were cleaned via ultrasonication in acetone, isopropanol, and deionized water for 20 minutes each and then subject to oxygen plasma at 300mTorr, 70W for 5 minutes. Exfoliation was done at 100^{o}C for higher yield of flakes. All layers were assembled via the polymer-assisted hot pickup technique [109] (with polycarbonate/polydimethylsiloxane stamps). Flakes were picked up between temperatures of 40-70^{o}C and dropped at 180^{o}C. The polycarbonate was washed off in chloroform followed by isopropanol overnight (12 hours). The assembly was done on a substrate of SiO_2 (285 nm)/Si with prepatterned electrodes/contacts of 5nm Ti/95nm Au fabricated with electron beam lithography followed by electron beam evaporation of metal and subsequent liftoff in acetone and isopropanol. Finally, the device was wire bonded onto a custom-made printed

circuit board. The device was then transferred to Attocube Attodry800 cryo microscope for optical characterization. Atomic force microscopy of the device is used to determine the thickness of emitter h-BN and buffer h-BN is.

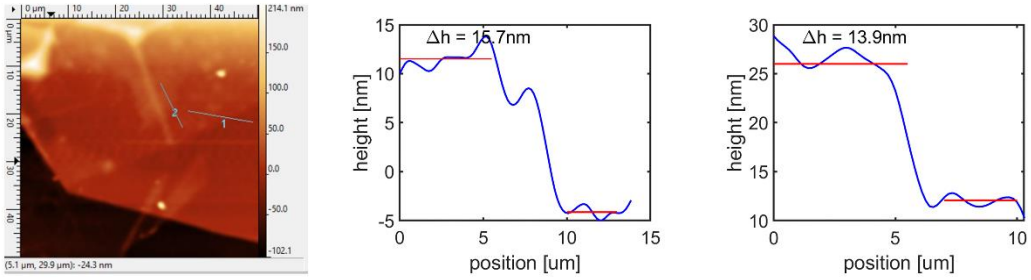

Figure 4.10. AFM topography (left panel) of the device. Two traces (middle and right panel) correspond to lines shown as 1 and 2 on the topography map. These two traces are used to extract the thickness of buffer h-BN and emitter h-BN flakes. The total thickness of both h-BN together is 15.7+13.9=29.6 nm.

4.7.3 Optical characterization

We use a 532nm CW laser (coherent) as excitation source for PL measurement at 100 µW and used a spectrometer (Princeton Instruments) to measure the PL spectrum. Spectra acquisition time was 60 seconds.

g2 experiment was done at room temperature with 532 nm CW excitation at 100 µW and the light was fiber coupled to a fiber beam splitter (Thorlabs) connected to two avalanche photo diodes (Micro photon devices) and the single-photon events were registered by a

Picoharp300 electronics (Picoquant) at TTTR mode. The signal was analyzed with a custom MATLAB script.

We used a tunable CW Dye laser (Sirah Mattise), the signal from emitter was passed through a 620 ±10nm bandpass filter and was detected via an avalanche photo diode. The excitation wavelength was measured with a wavemeter (Angstrom). PLE is performed at 10nW power at scan rate of 1 GHz/s.

The emission from single emitter is passed through a rotating polarizer and the signal is detected with an avalanche photo diode. Polarization measurement of the emitter shows a linearly polarized emission. This emission suggests a mainly in plane dipole.

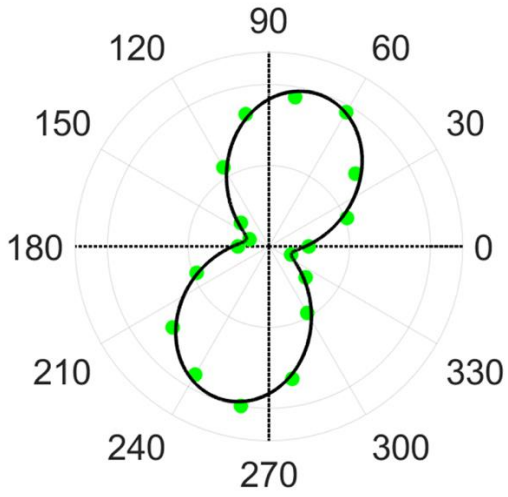

Figure 4.11. Polarimetry of the single-photon emitter performed at room temperature and without an electric field.

We did a least square fit to the polarization plot with the functional form of $I = I_0 + I_1 cos^2(\theta - \theta_0)$ and the resulting visibility is:

$$\frac{I_1}{I_0 + I_1} = 0.74 \pm 0.16.$$

We attribute the deviation of visibility from 1 to the finite numerical aperture of the objective lens, instabilities in emission at V=0 and small out of plane component of the dipole.

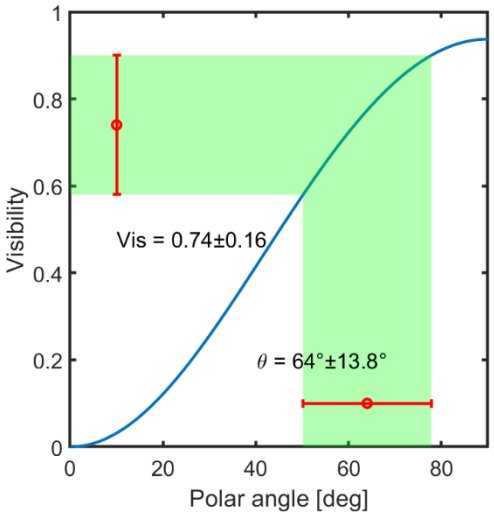

Figure 4.12. The resulst of ray tracing simulation to estimate the out of plane dipole component.

To quantitively estimate the dipole orientation we performed a ray tracing simulation to include the effect of NA=0.9 of the objective and the polar angle of the dipole is 64±14 degrees.

4.8 Summary and conclusion

In summary, we have shown that an out-of-plane electrostatic field can suppress spectral diffusion while also Stark tuning the emission energy of h-BN color center single-photon emitters. Our findings may pave the way for on-chip h-BN quantum communication technologies by removing the barrier to achieving lifetime limited photons, and to potentially generate indistinguishable photons. The extra degree of freedom provided by stark tuning is also desirable to couple the emitters to resonance modes of photonic cavities. Finally, we also studied the dependence of linewidth on temperature in lack of spectral diffusion and found it to be proportional to T^3.

Chapter 5. Photon statistics of h-BN emitters

5.1 Abstract

This study investigates the quantum photon statistics of h-BN emitters by analyzing the Mandel Q parameter. Through extensive experimentation, we measure Mandel Q for h-BN emitters under an array of excitation conditions, examining its dependence on various factors such as temperature and pump power. Our results show that under pulsed excitation we can achieve Mandel Q of -0.002 and under CW excitation this number can reach -0.0025. We investigate the effect of cryogenic temperatures on Mandel Q and conclude that temperature weakly correlates with Mandel Q. Finally, our findings are used to showcase the impact of Mandel Q in quantum applications by providing an example of random number generation and the effect of Mandel Q on the speed of generating random bits via this method.

5.2 Introduction

Hexagonal Boron Nitride (h-BN) is a 2D Van der Waals material with band gap of 6eV [42]. It is shown that point defects in h-BN can act as color centers and used as single-photon sources [2,45,46]. The underlying atomic structure of the class of h-BN emitters emitting at around 585 nm (which is used in this study) is reported to be dependent on Carbon impurities [21], However the exact atomic structure is not determined [20,21]. These emitters are shown to be highly stable at room temperature [19] and higher temperatures up to 800K [24] with a large Debye-Waller factor (>80%) [2]. These emitters exhibit tunable [27,28,123] and lifetime limited linewidth at cryogenic [59,123] and room temperature [25]. Due to the 2D host these emitters are a great candidate for on chip [29]

quantum-nano-photonic applications such as quantum communications and quantum computation [41].

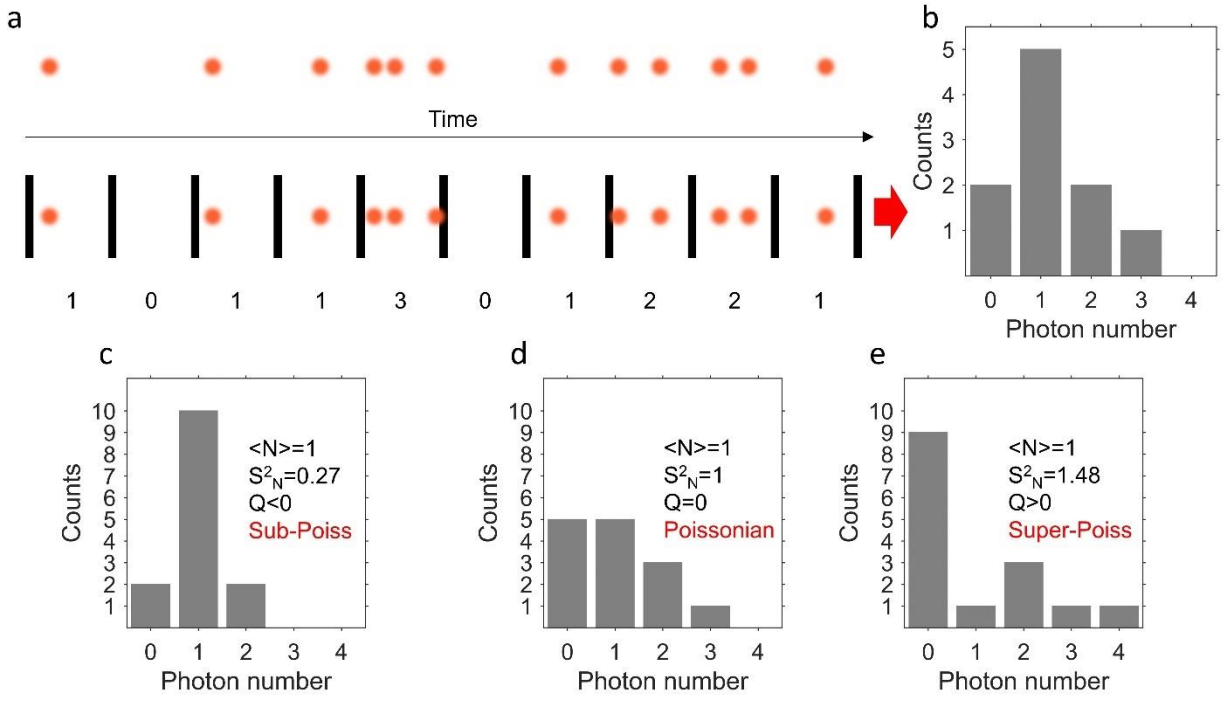

Figure 5.1. The schematic of Mandel Q analysis. (a) shows a stream of photon events with and without dividing into time bins, (b) is the histogram created by binning the photon stream, (c-d-e) histogram of Sub-Poissonian, Poissonian and super-Poissonian photon statistics. The value of Mandel Q depends on whether variance of the distribution is greater or smaller than the average.

For many quantum applications the requirement for the emitter is for it to be able to emit a single-photon (preferably indistinguishable single photon) on demand [33]. To satisfy this requirement one needs to achieve an ultimate sub-poissonian photon statistic. In other words, if we divide the photon generation into cycles, there needs to be one and only one photon

generated per each cycle. With this vision in mind Mandel proposed the notion of Q number [124,125]. Q is defined as:

$$Q = \frac{S^2{}_N}{\langle N \rangle} - 1.$$

In this equation $S^2{}_N$ is the variance of the photon number per cycle and ⟨N⟩ is the average number of photons per cycle. As shown in Figure 5.1 we can divide the stream of photons into several time-bins and measure the statistics of number of photons per bins. For a coherent source of light (LASER) the number distribution follows a poissonian distribution [126], in which the average and variance are equal, hence $Q_{LASER}=0$. For and ideal single-photon source, there is 1 and only 1 photon per cycle so the variance is zero, hence $Q_{Ideal\ SPE} = -1$, this mode of statistics is then called sub-poissonian for having a variance lesser than variance of Poissonian distribution. For a thermal source of light, the statistics is super-poissonian which means Q>0 [126] . Even though for an ideal SPE, Q=-1 for the case of real-world SPEs -1<Q<0 and the absolute value of Q for each excitation cycle is limited to the emission efficiency of the SPE and collection efficiency of the setup [127].

Mandel Q has been studied previously mainly in the pulsed excitation regime and theoretically the single-pulse Mandel Q is shown to be correlated with the value of $g^{(2)}(0)$ [126]. However, the experimental value of $Q_{single\ pulse}$ is limited by the collection efficiency of the experimental setup [127]:

$$Q_{experimental} = Q_{single\ pulse} \times \eta$$

where η is the combined losses in the photon detection process. The fact that this correlation between $g^{(2)}(0)$ and Q exists and the difficulty of measuring the $Q_{single\ pulse}$ due to losses has discouraged most of studies on quantum emitters to measure this parameter and only

report the $g^{(2)}$ function to showcase the quantum nature of the emission, despite the importance of Mandel Q for most applications.

Measuring photon statistics of a quantum emitter under continuous wave (CW) excitation has not been done extensively. We only encountered one study [128] that perform this analysis and based on their results dead time of single-photon detectors play a major role in determining the photon statistics.

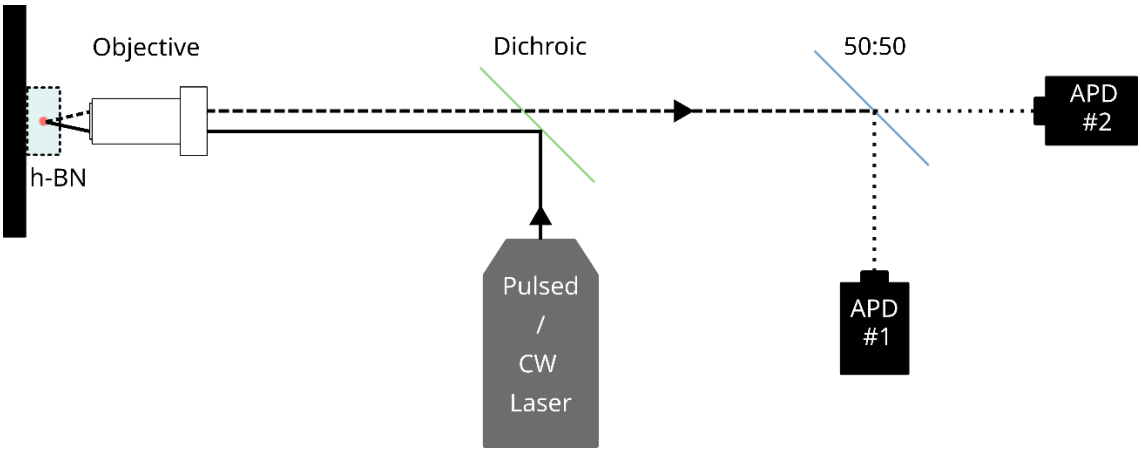

Figure 5.2 Schematic of the experimental setup that collects photon incidents for photon statistics analysis.

In this study we start by exploring the Mandel Q with the traditional method of pulsed excitation and for the first time explore the temperature dependence of pulsed Mandel Q. Then we explore rich regime of photon statistics of a stream of photons generated by CW pump. In this regime the natural time scale of pump and decay dictates the statistics of the emission. We show that in this regime we can beat the limit of efficiency of detection setup for Mandel Q and we also show that pump power can be used as knob to tune Mandel Q. We then use this knob to further demonstrate the importance of Mandel Q in quantum

applications that require on demand single photons. (In our case for random number generation.)

5.3 Pulsed Mandel Q

We start our analysis by studying emitters in exfoliated flakes of h-BN on Si/SiO2 substrate. The flakes are scanned in our homebuilt confocal microscope to find single-photon emitters. each emitter exhibiting a narrow zero phonon line then will be tested through intensity autocorrelation measurement to measure the $g^{(2)}$ function. For the emitter under study here we observe a zero phonon line at 588 nm and a $g^{(2)}(0)$ well below 0.5 threshold, that corresponds to a single-photon emitter. The emission rate shows two distinct on and off states switching between 50 to 100 kHz emission rate, this phenomenon is known as blinking [55,127] and is proposed to be a result of existence of a meta stable third state in the level structure of the emitter (as shown in Figure 5.3-g) . The pulsed $g^{(2)}$ also shows antibunching and the polarization pattern exhibits a dipole radiation pattern matching other studies [121,129]. We calculated the Mandel Q of this emitter by measuring the statistics of photons generated by each pulse in the time span between two consecutive pulses. To remove some of the background noise we performed time gating as introduced in previous studies [127] to remove photons arriving at times larger than 10ns (~10 times the decay lifetime of the emitter). Based on the loss in our microscope (efficiency ~0.005) we expect most of the pulses to show zero counts and some pulses containing 1 or two photons, we do not expect to observe more than 2 photons per pulse in this regime as it is limited by the dead time of the detectors. We chose the pulse-to-pulse duration of 100 ns based on the deadtime of our Avalanche photodiode single-photon detectors (more details in Methods section). as shown in Figure 5.3-h the single-pulse Mandel Q shows the value of -0.002.

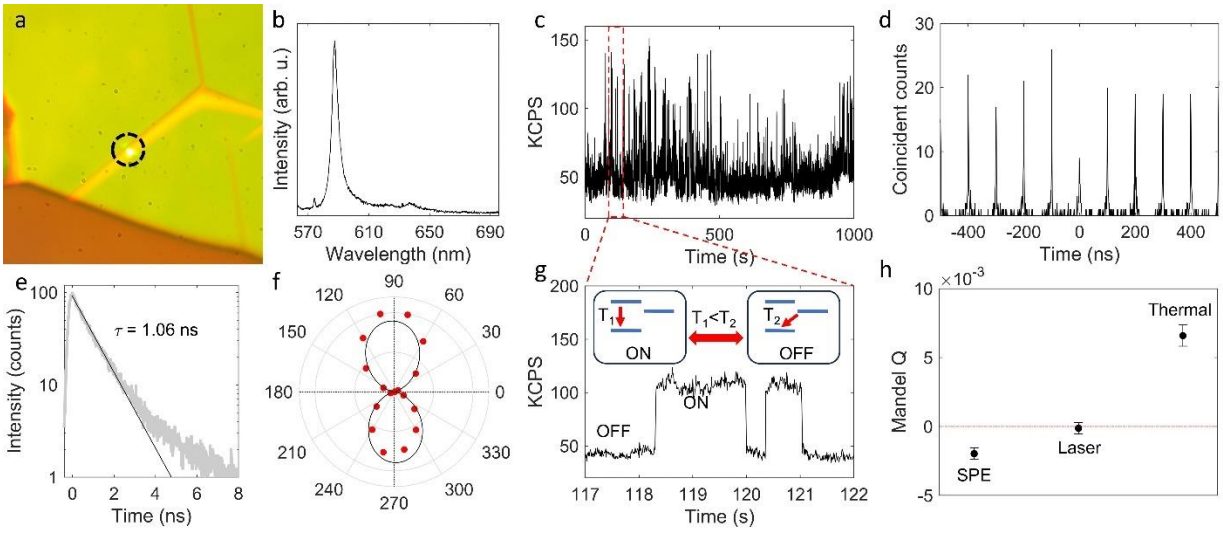

Figure 5.3. Characteristics of h-BN emitter under pulsed excitation. (a) Microscope image of the h-BN flake containing the quantum emitter. (b) PL spectral of the emitter with a ZPL at 588nm and a sideband at 638nm. Inset shows CW $g^{(2)}$ function of this emitter. (c & g) Emission rate of the emitter as a function of time. The emitter exhibits two emissive states of on and off with 50kHz and 100kHz emission rate, respectively. (d) Result of pulsed coincidence measurement of the emitter. (e) TRPL measurement shows decay lifetime of 1.06 ns. (f) Polarization measurement shows a dipole emission pattern. (h) Single-pulse Mandel Q values for emitter in h-BN, coherent source, and thermal source.

5.4 Comparison of h-BN quantum emitter and other light sources

To compare our results with a coherent source and a thermal source of light we perform the same experiment with a laser light and the thermal beam generated by a light bulb. As can be seen in table 5.1 we observe a Q= (-1.97±0.42) X10-3 for h-BN emitter. The result is well below zero considering the error of the measurement derived from averaging the results of 5 experiments. For laser light Q= (-1.25±4.01) X10-4 which shows zero is within the error bar, slight negative value can be explained by the effect of dead time on measurement of two consecutive photons, every instance recorded with two photons is a result of measuring one photon at channel 0 and another photon at channel 1 as one channel can not record both

photons since after recording the first instance it will enter a period in which it can not record another incidence. As a result, the number of two photon incidents that are recorded is smaller than the actual number of two photon incidents which results in a smaller Mandel Q. For thermal light we observe Q= (6.59±0.77) X10-3 which is positive within error bar as expected. This result is also depicted in Figure 5.3-h to compare the Mandel Q of single-photon source, laser, and thermal light.

Single-photon emitter

#	1-photon /pulse	2-photon counts	Mandel Q
1	0.005088	69	-0.00238
2	0.005667	97	-0.00224
3	0.005026	95	-0.00125
4	0.005349	97	-0.00172
5	0.004845	63	-0.00224
Average	5.20E-03	84.2	-1.97E-03
Std. Dev.	0.000286	17	4.24E-04

Laser

#	1-photon /pulse	2-photon counts	Mandel Q
1	0.00494	118	-0.00017
2	0.00497	104	-0.00078
3	0.00497	103	-0.00083
4	0.00491	133	0.000505
5	0.00492	125	0.00016
6	0.00493	124	9.98E-05
7	0.00491	123	9.67E-05
8	0.00495	115	-0.00031
9	0.00493	125	0.000133
10	0.00489	116	-0.00015
Average	4.93E-03	118.6	-1.25E-04
Std. Dev.	2.60E-04	9.5	4.01E-04

Thermal source

#	1-photon /pulse	2-photon counts	Mandel Q
1	5.50E-04	18	5.99E-03
2	5.46E-04	20	6.78E-03
3	5.47E-04	21	7.13E-03
4	5.55E-04	17	5.58E-03
5	5.49E-04	22	7.47E-03
Average	5.49E-04	20	6.59E-03
Std. Dev.	3.36E-06	2	7.68E-04

Table 5.1. Comparison of single-photon emitter, laser, and thermal light Mandel Q

5.5 Effect of temperature on Mandel Q

We performed this experiment on another emitter prepared via same method on the same substrate in a cryogenic microscope to study the effect of temperature on the photon statistics. This emitter exhibits a narrow zero phonon line at 585 nm. To measure the true linewidth of the emission we performed a photo luminescence excitation experiment in which we scan the zero-phonon line with a tunable CW laser and measure the emission rate in the side band (630nm-650nm). This measurement yields the value of 305 MHz for the linewidth which even though not quite lifetime limited but shows very small spectral diffusion at 7 K. We

measured the Mandel Q for temperature values of 7K, 50K, 100K, 150K, 200K, 250K and for each temperature we performed the same time gating procedure mentioned previously to remove the background noises and the result shows that however the minimum Mandel Q is achieved at 7K the correlation of Mandel Q to temperature is not strong and the value of Mandel Q fluctuates around zero with a minimum of -0.0002. We estimate the optical losses in our cryo-microscope to be around 0.0005 which might explain the difference between the numbers observed at room temperature and cryo temperatures.

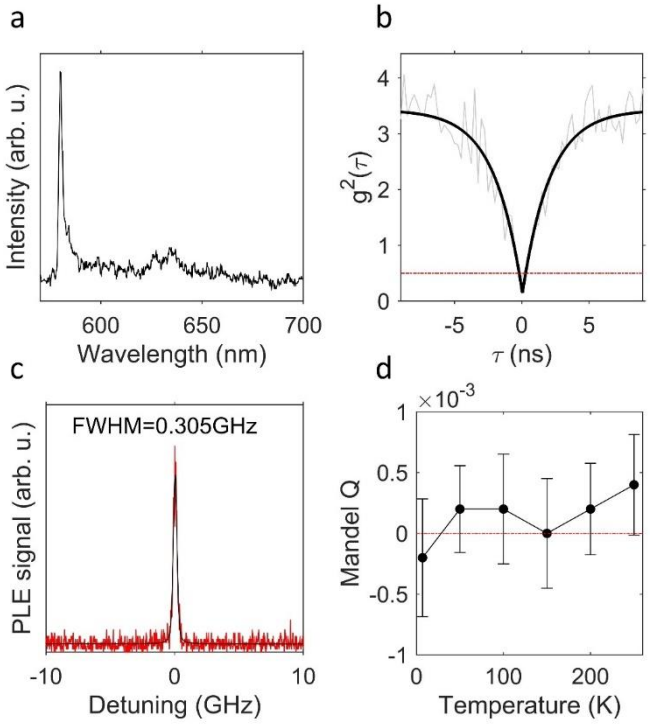

Figure 5.4. Temperature dependence of h-BN emitter Mandel Q under pulsed excitation. (a) PL spectra of the emitter at 7K, (b) CW g(2) function of the emitter. (c) Result of PLE experiment on the zero phonon line of the emitter, the emission shows a narrow linewidth of 305MHz. (c) Mandel Q of emitter at different temperatures from 7K to 250K.

5.6 CW Mandel Q

Furthermore, we studied the photon statistics of h-BN emitter in the CW regime. In this regime we have the freedom of choosing the time bin size to measure Mandel Q as there is no intrinsic time scale (other than the lifetime of the emitter). This concept is depicted in Figure 5.5(a). However base on a previous study [19] the dead time of our detectors can skew the result towards more negative numbers. To resolve this issue we have limited ourselves to a regime in which the inverse count rate of photons (~1000 ns) is much longer than the dead time(~100 ns). In this regime the average time span between two consecutive photons is much longer than the dead time and as a result the effect of dead time does not affect our result.

We examine a range of time bin sizes to reveal the optimal time bin size to reach the largest negative value of Mandel Q. As shown in Figure 5.5-b there is an optimal value of Mandel Q, we denote this value by Q_{min} and the time bin size that corresponds to this value as T_{Qmin}. Another interesting time scale in this analysis is the time bin size in which the emitter reaches Q=0 we call this time scale the onset of coherence as emitters in this condition exhibits poissonian photon statistics and at larger time scales exhibits super poissonian statistics. We use pump power as a knob to change the photon emission rate and study the CW photon statistics of the h-BN quantum emitter. As shown in Figure 5.5-c we operate in the linear regime of excitation-emission and not close to saturation. But we notice a not monotonic dependence of minimum Mandel Q on pump power. However, the dependence of minimum Mandel Q on T_{Qmin} is observed.

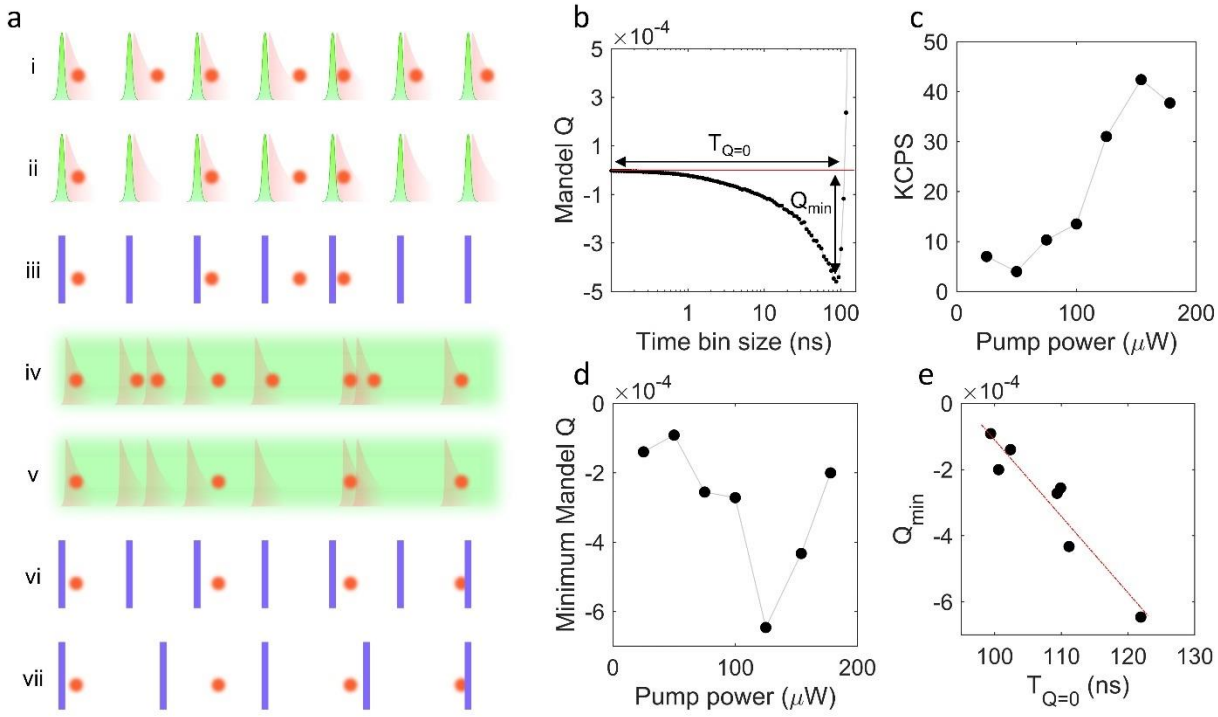

Figure 5.5. CW Mandel Q of h-BN emitter. (a) Schematic of pulsed and CW Mandel Q. (i) Ideal case of pulsed excitation will result in one single-photon per pulse, (ii) considering losses, some of the single photons cannot be detected, (iii) pulse to pulse time scale imposes a natural time scale for binning and reporting the photon statistics. (iv) With CW excitation there is a stream of photons generated based on random excitation and decay of the emitter, (v) due to losses, some of the photons generated cannot be detected, (vi-vii) in the case of CW the freedom to choose the bin size can offset the effect of collection efficiency to some extent. (b) plot of CW Mandel Q as a function of time bin size. (c) Dependence of photon emission rate on pump power shows we are not operating near saturation. (d) CW Mandel Q Vs. pump power. This plot does not show a clear dependence of CW Mandel Q on pump power mainly due to blinking. (e) There is a strong correlation between Qmin and onset of coherence.

To understand this pattern, we study the blinking behavior of the emitter at various pump powers and try to isolate the on times (in which the emitter is in a brighter state) and off times (in which the emitter is in a darker state) and calculate Mandel Q for each case individually.

The result shown in Figure 5.6 shows that as long as the portion of On time is significant the Minimum Mandel Q is inversely correlated with the pump power. We want to note at the maximum pump power the emitter became quite unstable and was in the on state only for a short while.

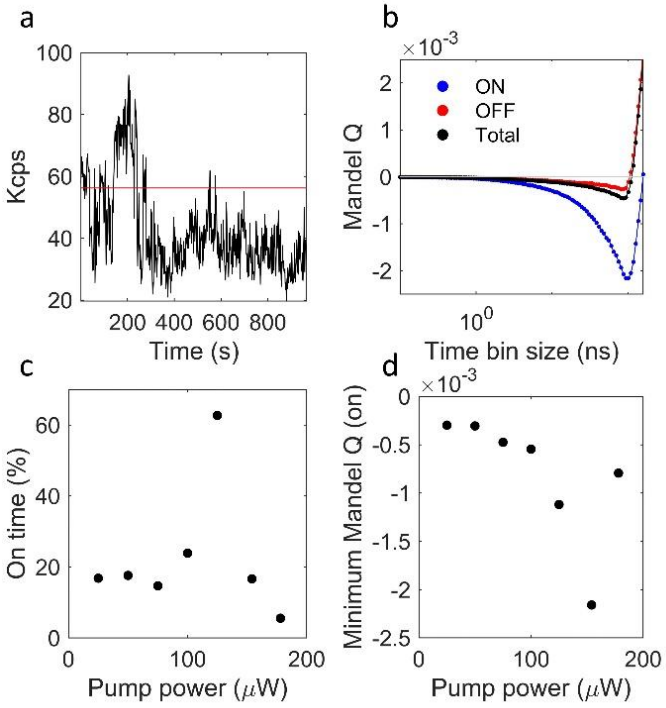

Figure 5.6. Effect of blinking on Mandel Q. (a) Emission rate of the emitter Vs. time shows clear on and off states. (b) dividing the data into on and off parts and calculating Mandel Q for each part. (c) Dependence of blinking on pump power. As the pump power changes the blinking pattern also changes and there is no clear correlation between pump power and the percentage of time that emitter is in the on state. However, for the maximum power (175μW) the emitter is mostly in the off state. (d) Dependence of minimum CW Mandel Q on pump power. As power increases, the Mandel Q decreases.

5.7 Application of Mandel Q in Random Number Generation

Since we can use pump power as a knob to change the CW Mandel Q, we used this advantage to showcase the importance of Mandel Q in quantum applications. We chose quantum random number generation as an example of quantum application that depend on on-demand single-photon sources. We note that other studies already used h-BN emitters for random number generation [130,131]. We propose two protocols to generate random bits from h-BN single-photon emitter to stablish the importance of Mandel Q in randomness of the bits generated. In the first method we use each individual photon even recorded in the two single-photon detectors at the two end of our Hanbury Brown-Twiss setup and if the photon was detected at channel 0 we generated a bit with value 0 and if the photon was recorded at channel 1 we generated a bit with value 1. In the second method we chose a time bin size equal to TQmin and bin the detected stream of photon events based on this value. Then we search for bins with 1 and only 1 photon in the bin. And finally, if the photon is recorded in channel 0 we generated a bit with value 0 and if the singular photon is in bin is recorded in channel 1 we generated a bit with value 1.

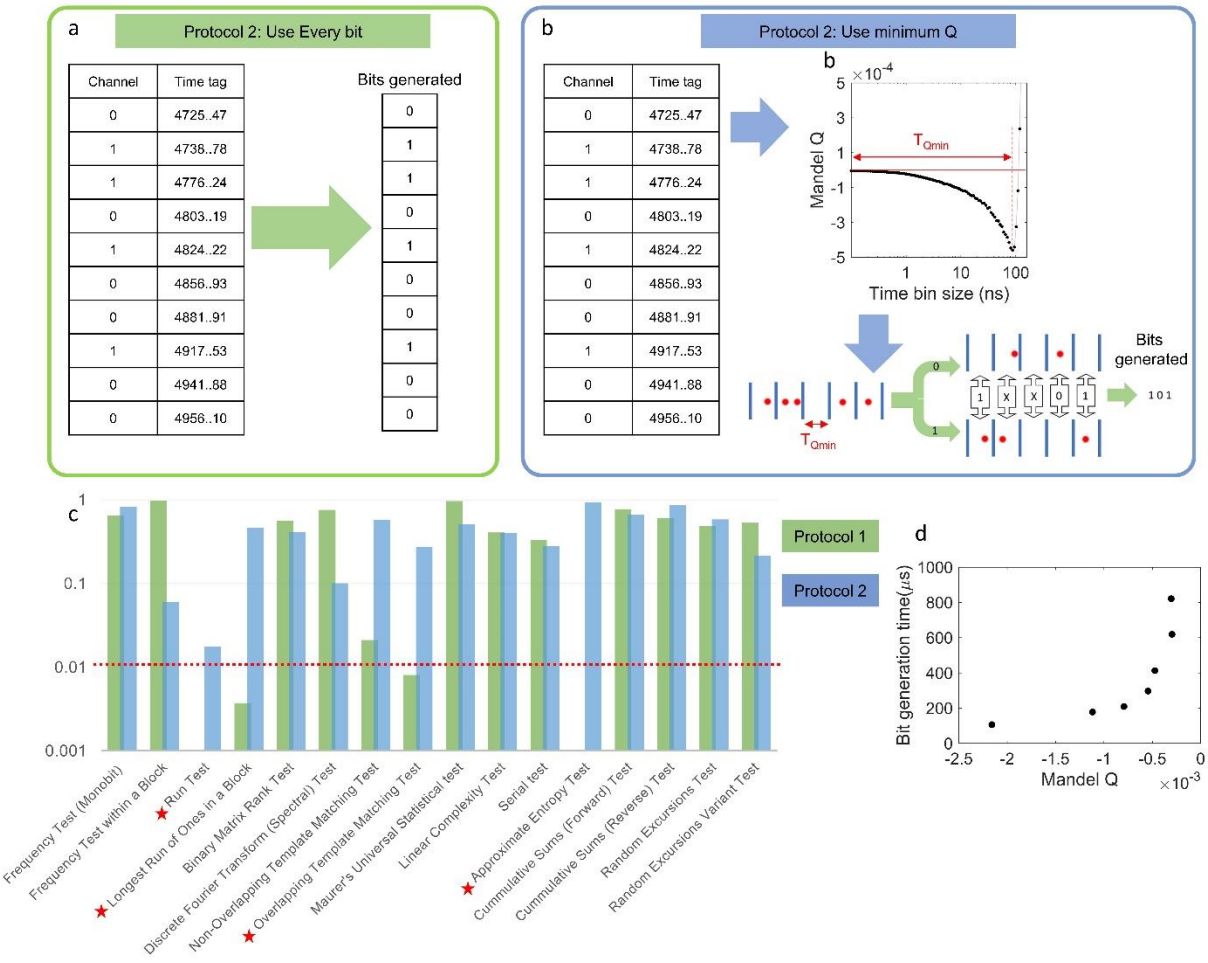

Figure 5.7. Random number generation with h-BN emitters. (a) Protocol 1 of RNG. In this protocol we do not use Mandel Q and simply examine every photon detected. (b) Protocol 2 of RNG. In this protocol we bin the data with the time bin size that provides the minimum Q. (c) comparison of randomness of the bits generated by each protocol via NIST randomness test suite. Protocol 2 passes all tests while protocol 1 does not pass 4 tests. (d) Dependence of time required to generate a bit with protocol 2 with emitter pumped at various pump powers on the Mandel Q. The trend clearly shows at more negative Mandel Qs it takes less time to generate a random bit.

To compare these protocols, we ran the random numbers generated through NIST randomness test [132]. This test suite performs 16 different test to approve the randomness of the bits generated. With each method we generated 400'000 bits and based on the result shown in Fig 5.7-c the bits generated with method 1 did not pass 4 of the 16 tests while the bits generated by method 2 passed all the tests.

To demonstrate the randomness, we also generated a set of 20 digit binaries and turned them into decimal. The result should be a random decimal between 0 and 2^{20}~10^6 .we then plotted the histograms of these decimals and the result for all pump powers looked like the uniform distribution.

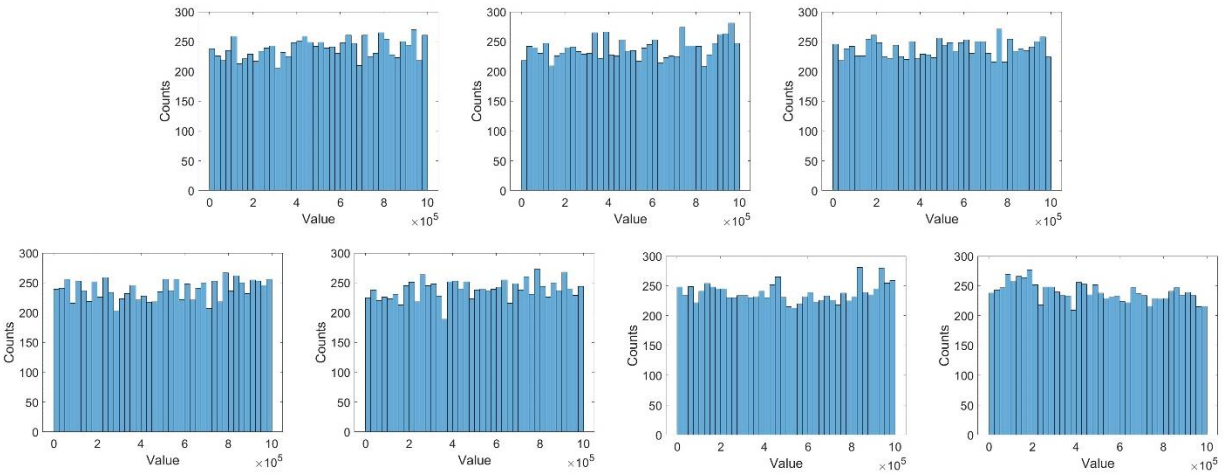

Figure 5.8. Histograms of random decimals generated binned from 0 to 106 for powers from 25-175μW.

Furthermore, we calculated the time it took to generate one bit on average for each pump power and showed that as CW Mandel Q decreases the random bit generation rate increases. This is an intuitive conclusion as we know the most negative Q means there is higher on-

demand-ness of photon generation process and as a result the process can be performed in fewer cycles. This result shows the significance of Mandel Q for quantum applications that require on demand single photons, such as quantum communication and quantum computation.

5.8 Conclusion

To sum up, this research serves as a deep dive into the world of photon statistics of h-BN emitters. We explored both pulsed and CW excitation, at room temperature and at cryogenic temperatures, with various pump powers. We showed that h-BN quantum emitters exhibit negative Mandel Q in the pulsed excitation regime as expected. To Show the credibility of our methodology we compared this value to a coherent source of light and a thermal source of light. We examined the photon statistics of a narrow linewidth emitter at cryogenic temperatures and did not observe a strong dependence of Mandel Q on Temperature. Furthermore, we studied CW Mandel Q of h-BN emitters and showed how pump power can act as a knob to change CW Mandel Q and finally we demonstrated how The value of Mandel Q impacts the performance of a quantum random number generator and for a more negative Mandel Q (for the same emitter) the process of random number generation can be sped up.

Chapter 6. The path forward

6.1 Towards indistinguishable single-photon emitters in h-BN

In this thesis, we have demonstrated a method for achieving lifetime-limited linewidth in single-photon emission from hexagonal boron nitride (h-BN). However, the measurement that confirmed this lifetime-limited linewidth—photoluminescence excitation—is inherently an absorption measurement. We inferred the existence of lifetime-limited photons by relying on the reciprocity principle between absorption and emission. Future efforts should concentrate on extracting these lifetime-limited single photons and testing their indistinguishability. The conditions that lead to a lifetime-limited linewidth, particularly the suppression of spectral diffusion and resonant excitation, should also apply in the case of indistinguishable single-photon emission. Nevertheless, fulfilling the resonant excitation condition presents several challenges. Firstly, extracting single photons resonant with the excitation laser necessitates a method to filter out the back-scattered remaining laser photons. This filtering cannot rely on the energy of the photons, as both laser photons and single-emitter photons share the same energy. Consequently, we have begun to develop a filtering scheme based on the polarization difference between excitation photons and emitter photons, as discussed in Section 6.1.1.

Moreover, we require a method to characterize the linewidth of these lifetime-limited photons. Grating-based spectrometers lack sufficient resolution to resolve the narrow linewidth, and the photoluminescence excitation used previously for measuring the narrow linewidth is ineffective in this context due to its inherent nature as an absorption measurement. As a result, we designed and constructed an interferometry setup to perform single-photon interference. By collecting sufficient data and measuring the coherence length

of the single-photon wave packets, we can determine both the linewidth and the wave packet structure of the photons, deriving the linewidth accordingly. This method is explained in Section 6.1.2.

Lastly, we need a method to assess the indistinguishability of single photons. Historically, this measurement is performed using a Hong-Ou-Mandel experiment. This method can be conducted with a single emitter by introducing a delay line to observe the interaction between two consecutive photons from the same emitter, or with two separate emitters that emit photons of the same energy and coherence properties. The details of this measurement are outlined in Section 6.1.3.

6.1.1 Cross polarization filtering

The concept of cross-polarization filtering involves exciting the emitter with a linearly polarized laser and collecting photons emitted from the emitter with a polarization perpendicular to the excitation polarization. Although the emission pattern of the h-BN emitter is dipole, optimal excitation and detection are not feasible. However, by performing the excitation with linearly polarized light at a 45° angle to the emitter's dipole axis and collecting the light through a linear polarizer at -45° relative to the dipole axis, we can collect half of the emitted light. This amount is sufficient for conducting quantum experiments, though it requires twice the time to achieve a similar signal-to-noise ratio. To effectively remove the laser light and achieve a desirable signal-to-noise ratio comparable to spectral filtering, we need an extinction ratio of 10^{-6}.

We attempted to build a setup consisting of a linear polarizer in the excitation path, along with a linear polarizer in the detection channel. In this experiment, we observed that the

extinction ratio barely reached 10^{-1}. Consequently, we hypothesized that the optics in our microscope were either depolarizing or altering the polarization state of the light.

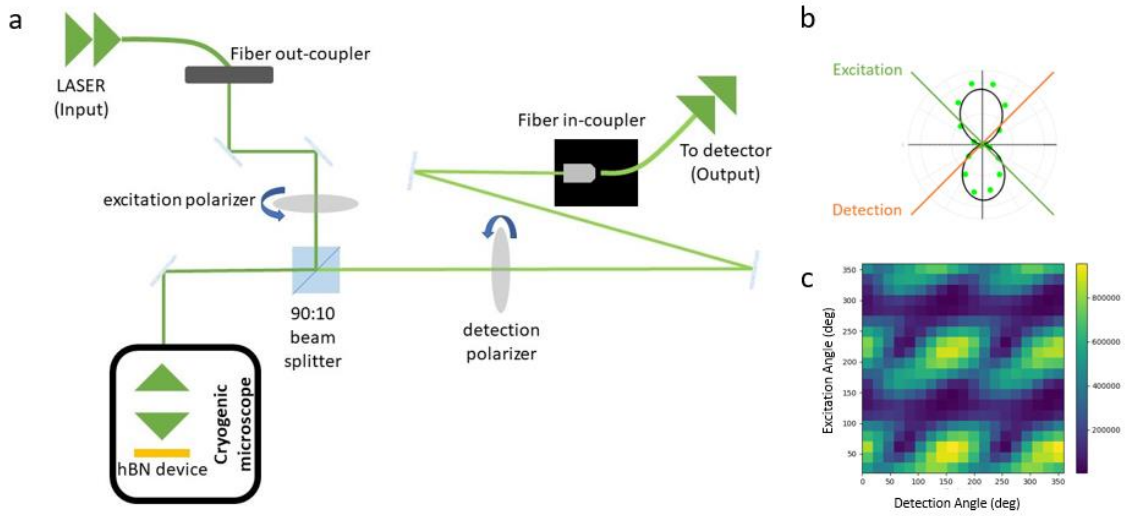

Figure 6.1. The cross polarization technique. (a) a schematic of the simplest possible the cross polarization setup with two polarizers and a 90:10 beam splitter. (b) ideal configuration of emitter dipole and excitation and detection polarizers. (c) result of rotating both excitation and detection polarizers, the color indicates the amount of output intensity.

To investigate this, we performed an experiment to examine the output of the microscope when linearly polarized light enters under various conditions, using a method involving a quarter-wave plate and a linear polarizer, as explained in a referenced study [133]. By rotating the quarter-wave plate and recording the output intensity, we measured the four Stokes parameters describing the full polarization state of the output light.

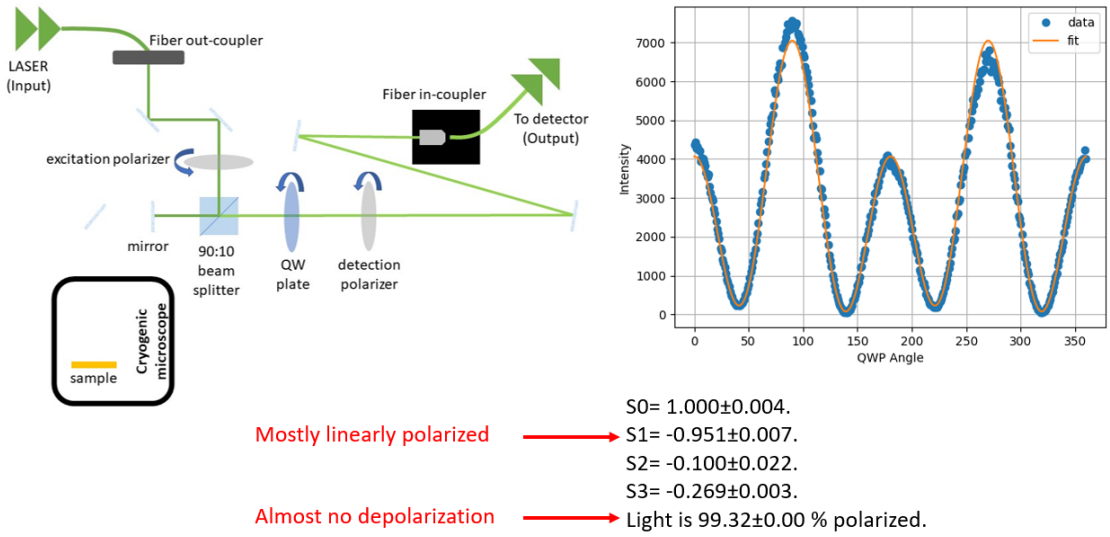

Figure 6.2. the result of experiment with blocking the beam with a mirror and rotating the QWP. Result shows a small change of polarization plane, and very small depolarization.

Initially, we blocked the output of a 90:10 beam splitter with a mirror to determine if the beam splitter was altering the polarization state. The resulting Stokes parameters indicated that the beam splitter did not significantly change the polarization state, nor did it depolarize the light.

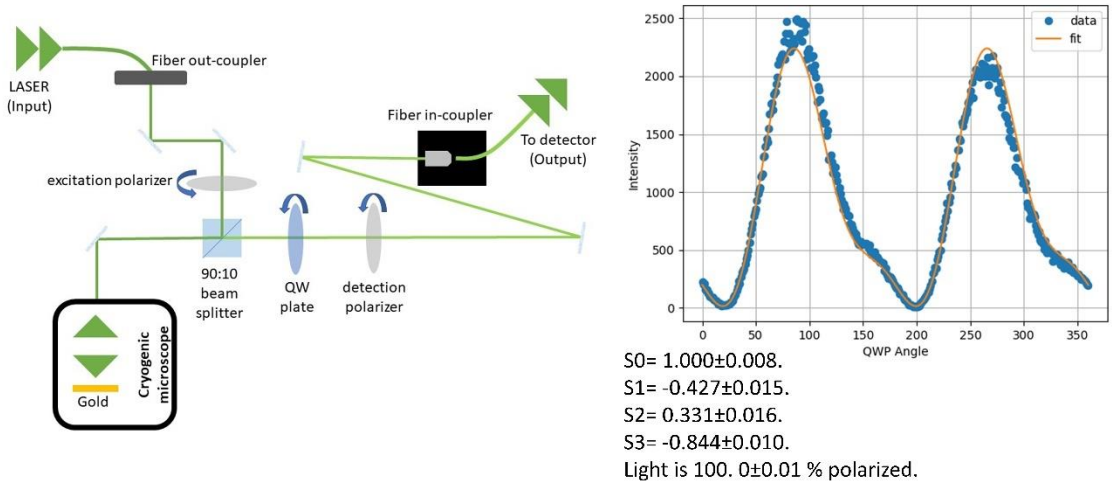

Figure 6.3. The experiment with reflective gold sample instead of h-BN sample. the result shows that the microscope optic change the polarization to an elliptical state with a large S_3.

Next, we replaced the h-BN sample with reflective gold to test if the change in polarization was caused by the microscope's optics. The experiment showed that the output light had a significant circular polarization component. Depolarization, calculated as below was negligible:

$$depolarization(\%) = \left(1 - \frac{S_1^2 + S_2^2 + S_3^2}{S_0^2}\right) \times 100.$$

Replacing the gold with an h-BN and graphene device on a SiO2/Si substrate showed that the sample depolarized the light by 3% but did not further change the polarization state. Our findings suggest that the microscope's internal optics, including the objective lens and mirrors, alter the polarization state from linear to elliptical. To counteract this, we used a quarter-wave plate in the detection path, achieving an extinction ratio of 10^{-4}. The remaining

discrepancy to 10^{-6} is attributed mainly to the light's depolarization caused by the h-BN device and the suboptimal extinction ratio of the polarizer.

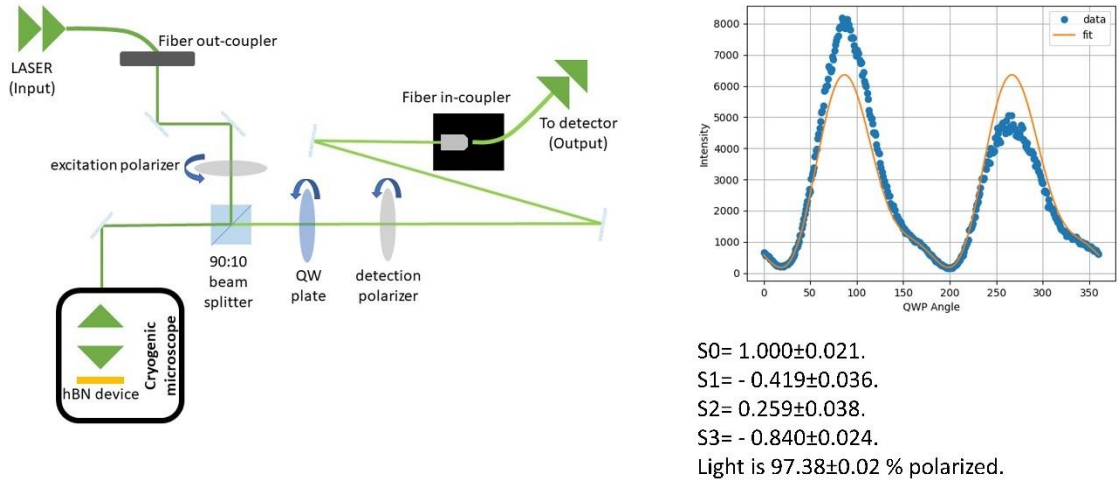

Figure 6.4. Schematic and the result of the experiment with a full h-BN device. Result shows an elliptically polarized light similar to the gold sample however there is around 3% depolarization.

We also experimented with Glan-Thompson polarizers, which offer higher extinction ratios. However, these polarizers displace the beam based on their orientation, complicating the coupling of the output light to fiber-coupled detection devices.

In summary, we attempted to construct a cross-polarization setup to filter the excitation beam based on its polarization. However, we realized that a simple cross-polarization scheme is ineffective due to the ellipticity induced by our microscope optics. Further refinement of the optical setup is required to efficiently use Glan-Thompson polarizers and effectively couple the output light to the detectors.

6.1.2 Single-photon interferometry

We developed a Mach-Zehnder interferometer to analyze the single photons emitted by the h-BN emitter. The advantage of the Mach-Zehnder geometry lies in its ability to probe both outputs simultaneously, making it suitable for correlation measurements if needed. However, for single-photon interferometry, only one of the outputs is necessary. The schematic of the setup is shown in Figure 6.5. Our interferometer consists of a long arm, spanning 300 mm, and a short arm, extending 3 mm, equipped with a piezo stage that has a precision of 50 nm. We successfully observed fringes using an input laser light of 532 nm. The effectiveness of this setup for single-photon interferometry relies on the efficient filtering discussed in Section 6.1.1. In principle, this setup is capable of measuring coherence times as short as femtoseconds, which is significantly more precise than required for measuring the nanosecond-lifetime coherence of the single photons in h-BN.

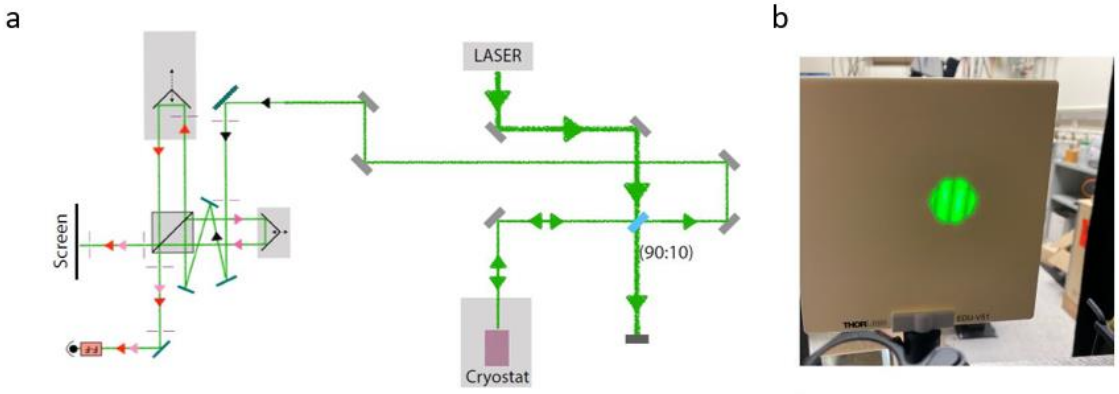

Figure 6.5. The interferometry setup to measure emitter linewidth. (a) The schematic of our MZI. (b) The resulting fringes appearing on the screen.

6.1.3 Hong-Ou-Mandel experiment

The Hong-Ou-Mandel (HOM) experiment is a significant experiment in the field of quantum optics that demonstrates two-photon interference. This phenomenon was first observed in 1987 by Chung Ki Hong, Zheyu Ou, and Leonard Mandel [125], physicists from the University of Rochester. The essence of the HOM effect lies in its demonstration of two identical single-photon waves entering a 50:50 beam splitter, one photon in each input port.

In the experiment, when two indistinguishable photons impinge on a beam splitter, each entering through a separate input, they invariably exit together through the same output port. This outcome highlights a fundamental aspect of nonclassical interference and serves as a foundational experiment for numerous studies in quantum information. The experiment involves the interference of two photons as they reach a symmetric beamsplitter.

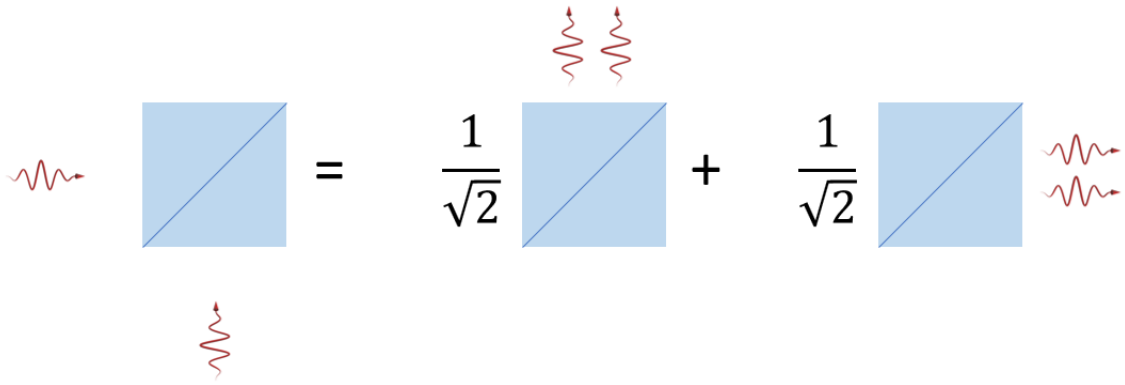

Figure 6.6. In HOM experiment if the two incoming photons are indistinguishable they interact and as a result both photons exit at the same channel.

This effect is an example of a two-particle interference phenomenon, which is a key concept in quantum mechanics. It demonstrates the quantum nature of light, as such behavior does not align with classical physics predictions. In the context of the HOM experiment, the photons (or in some variations, other bosonic particles) always emerge on the same, but randomly chosen, output port when they interfere on a beam splitter.

6.2 High photon collection efficiency

Another limitation of h-BN emitters is their low photon collection efficiency. While the few-nanosecond lifetime of these emitters should yield an emission rate of a few hundred GHz, the recorded emission rates at saturation are only in the order of a few MHz. This discrepancy is largely due to low collection efficiency. A considerable part of this inefficiency stems from the poor coupling of the emitter to the microscope optics. With a conventional objective lens, depending on its numerical aperture, only a small fraction of the photons emitted by the emitter is collected. One solution to this issue involves using nanophotonics to direct the light emitted by the quantum emitter towards a specific location by manipulating the local density of optical states. We have proposed a design that utilizes silicon nano-discs to enhance the directionality of the emission. Additionally, we designed a meta-surface lens to efficiently collimate the single photons and direct them in an out-of-plane direction. Details of this design are available in the referenced study [134].

Another factor contributing to loss is the microscope's optics. To minimize these losses, it might be necessary to redesign the microscope, incorporating fewer optical components. Switching to free-space detectors instead of fiber-coupled detectors could significantly improve collection efficiency.

6.3 Photon addition

There is a theoretical proposal suggesting the use of single-photon emitters to enhance the signal-to-noise ratio of a weak light beam [135]. In this approach, an excited single-photon emitter is positioned in the path of a weak optical beam, which comprises a few photons per unit time. As the weak beam interacts with the emitter, the emitter couples to the beam and undergoes a stimulated emission process, thereby adding a photon to the weak beam. Since the added photon is coherent with the photons in the weak beam, it contributes solely to the signal, not the noise, significantly improving the signal-to-noise ratio. This method could be beneficial for imaging objects with low signals, such as distant galaxies and dimly lit objects.

Our focus has been on the physical realization of this method using h-BN quantum emitters. h-BN emitters are particularly suitable for this application due to their ability to generate lifetime-limited photons and their compatibility with well-established chip-based photonics technology. However, several steps must be taken to achieve this realization. This section outlines the necessary steps for conducting a photon addition experiment.

6.3.1 The emitter requirements

For this technology, we require a stable, lifetime-limited emitter that resonates with the weak incoming beam. Since we often lack control over the energy of the incoming photons in photon addition applications, a tunable emitter is necessary to match the energy of the weak beam. As demonstrated in Chapter 3, h-BN emitters are tunable via Stark shift and exhibit lifetime-limited absorption. However, the range of tunability is quite narrow (just a few nanometers in wavelength), and the emitter is only lifetime-limited within a small portion of this tunability range. This limitation arises because the mechanism that eliminates spectral diffusion is linked to the Stark shift. Consequently, we require an additional tuning

mechanism to alter the energy of the emitter. Fortunately, research indicates that the energy of h-BN emitters can also be tuned using strain. Additionally, introducing an extra in-plane electric field might allow for tuning over a broader energy span. Nonetheless, the impact of these tuning mechanisms on the linewidth remains to be studied.

6.3.2 Optical setup requirements

To successfully perform photon addition, precise timing of two events is necessary. Firstly, the emitter should be resonantly excited. Then, the weak beam needs to resonantly interact with the emitter. The time difference between these two pulses should be set to prevent overlap, enabling us to distinguish between the two events. However, this interval cannot be too long, as the emitter will spontaneously decay within the first few nanoseconds after excitation. Since we possess a continuous wave (CW) tunable laser, it can be used for both beams as they share the same energy, but their intensities need to be vastly different. The excitation beam must be strong enough to overcome the low cross-section of the emitter for efficient excitation (requiring power on the order of nanowatts), while the weak beam should consist of only a few photons per pulse. Additionally, we need a method to convert the CW laser into pulses.

Confronted with these challenges, our initial design involves using an Acousto-Optical Modulator (AOM) to shape the pulses. These pulses will then be sent through a beam splitter to create the excitation and weak beam pulses. The weak beam pulse should pass through an attenuator to achieve the desired intensity, and a delay line should be added to this path to ensure correct pulse sequencing. The paths of the two beams will then converge in a second beam splitter, directing the resulting beam towards the emitter.

Currently, we have obtained and set up the AOM in the excitation path. This AOM is aligned to produce first-order controllable diffraction, which is regulated by an input voltage. Engineering the precise voltage values to create the appropriate pulse train and establishing the desired delay line requires further simulation.

6.3.3 Detection scheme

To validate the success of the photon addition process, two measurements can be conducted. The first is the direct measurement of the photon statistics of the weak beam. Since the input state's statistics are well-engineered and known, the photon-added state at the output should exhibit an additional photon. A method similar to the one described in Chapter 5 can be employed for this experiment. However, if the average photon number exceeds two, a photon number-resolving detector is required to circumvent the complexities introduced by the dead time of avalanche photodiodes.

The second method to validate photon addition involves measuring the fringe visibility of the output beam through an interferometer. The underlying principle here is that the photon added coherently to the weak beam should have a phase that matches the initial phase of the weak beam. Therefore, performing interferometry on the weak beam before and after photon addition should reveal an enhancement in the fringe visibility of the photon-added beam. This method is superior to measuring photon statistics as it provides insights into the stimulated emission process. It can distinguish between stimulated emission and spontaneous photon addition, over which we have no control. For this purpose, the Mach-Zehnder interferometer discussed in section 6.1.2 can be used.

Bibliography

[1] L. Museur and A. Kanaev, *Near Band-Gap Photoluminescence Properties of Hexagonal Boron Nitride*, J. Appl. Phys. **103**, (2008).

[2] T. T. Tran, K. Bray, M. J. Ford, M. Toth, and I. Aharonovich, *Quantum Emission from Hexagonal Boron Nitride Monolayers*, Nat. Nanotechnol. **11**, 37 (2016).

[3] A. K. Geim and I. V. Grigorieva, *Van Der Waals Heterostructures*, Nature **499**, 419 (2013).

[4] B. Lounis and M. Orrit, *Single-Photon Sources*, Reports Prog. Phys. **68**, 1129 (2005).

[5] C. L. Degen, F. Reinhard, and P. Cappellaro, *Quantum Sensing*, Rev. Mod. Phys. **89**, 1 (2017).

[6] M. Herrero-Collantes and J. C. Garcia-Escartin, *Quantum Random Number Generators*, Rev. Mod. Phys. **89**, 1 (2017).

[7] N. Gisin and R. Thew, *Quantum Communication*, Nat. Photonics **1**, 165 (2007).

[8] D. Cozzolino, B. Da Lio, D. Bacco, and L. K. Oxenløwe, *High-Dimensional Quantum Communication: Benefits, Progress, and Future Challenges*, Adv. Quantum Technol. **2**, 1 (2019).

[9] S. Slussarenko and G. J. Pryde, *Photonic Quantum Information Processing: A Concise Review*, Oxford Open Mater. Sci. **6**, (2019).

[10] J. Wang, F. Sciarrino, A. Laing, and M. G. Thompson, *Integrated Photonic Quantum Technologies*, Nat. Photonics **14**, 273 (2020).

[11] C. D. Bruzewicz, J. Chiaverini, R. McConnell, and J. M. Sage, *Trapped-Ion Quantum Computing: Progress and Challenges*, Appl. Phys. Rev. **6**, (2019).

[12] T. Schröder, S. Mouradian, J. Zheng, M. E. Trusheim, M. Walsh, E. H. Chen, L. Li, I. Bayn, and D. Englund, *Review Article: Quantum Nanophotonics in Diamond*, J. Opt. Soc. Am. B **33**, B65 (2016).

[13] I. Aharonovich and E. Neu, *Diamond Nanophotonics*, Adv. Opt. Mater. **2**, 911 (2014).

[14] P. K. Shandilya, S. Flagan, N. C. Carvalho, E. Zohari, V. K. Kavatamane, J. E. Losby, and P. E. Barclay, *Diamond Integrated Quantum Nanophotonics: Spins, Photons and Phonons*, J. Light. Technol. **40**, 7538 (2022).

[15] C. Toninelli, I. Gerhardt, A. S. Clark, A. Reserbat-Plantey, S. Götzinger, Z. Ristanović, M. Colautti, P. Lombardi, K. D. Major, I. Deperasińska, W. H. Pernice, F. H. L. Koppens, B. Kozankiewicz, A. Gourdon, V. Sandoghdar, and M. Orrit, *Single Organic Molecules for Photonic Quantum Technologies*, Nat. Mater. **20**, 1615 (2021).

[16] M. B. Gaither-ganim, S. A. Newlon, M. G. Anderson, and B. Lee, *Organic Molecule Single-Photon Sources*, Oxford Open Mater. Sci. **3**, (2023).

[17] Y. Arakawa and M. J. Holmes, *Progress in Quantum-Dot Single Photon Sources for Quantum Information Technologies: A Broad Spectrum Overview*, Appl. Phys. Rev. **7**, 021309 (2020).

[18] L. Seravalli and F. Sacconi, *Reviewing Quantum Dots for Single-Photon Emission at 1.55 Mm: A Quantitative Comparison of Materials*, JPhys Mater. **3**, (2020).

[19] T. T. Tran, C. Elbadawi, D. Totonjian, C. J. Lobo, G. Grosso, H. Moon, D. R. Englund, M. J. Ford, I. Aharonovich, and M. Toth, *Robust Multicolor Single Photon Emission from Point Defects in Hexagonal Boron Nitride*, ACS Nano **10**, 7331 (2016).

[20] S. A. Tawfik, S. Ali, M. Fronzi, M. Kianinia, T. T. Tran, C. Stampfl, I. Aharonovich, M. Toth, and M. J. Ford, *First-Principles Investigation of Quantum Emission from HBN Defects*, Nanoscale **9**, 13575 (2017).

[21] N. Mendelson, D. Chugh, T. S. Cheng, A. Gottscholl, H. Long, C. J. Mellor, A. Zettl, V. Dyakonov, P. H. Beton, S. V. Novikov, C. Jagadish, H. H. Tan, M. Toth, C. Bradac, and I. Aharonovich, *Identifying Carbon as the Source of Visible Single Photon Emission from Hexagonal Boron Nitride*, Nat. Mater. **20**, 321 (2020).

[22] S. Gao, H. Y. Chen, and M. Bernardi, *Radiative Properties of Quantum Emitters in Boron Nitride from Excited State Calculations and Bayesian Analysis*, NPJ Comput. Mater. **7**, 1 (2021).

[23] M. Abdi, J. P. Chou, A. Gali, and M. B. Plenio, *Color Centers in Hexagonal Boron Nitride Monolayers: A Group Theory and Ab Initio Analysis*, ACS Photonics **5**, 1967 (2018).

[24] M. Kianinia, B. Regan, S. A. Tawfik, T. T. Tran, M. J. Ford, I. Aharonovich, and M. Toth, *Robust Solid-State Quantum System Operating at 800 K*, ACS Photonics **4**, 768 (2017).

[25] A. Dietrich, M. W. Doherty, I. Aharonovich, and A. Kubanek, *Solid-State Single Photon Source with Fourier Transform Limited Lines at Room Temperature*, Phys. Rev. B **101**, 081401(R) (2020).

[26] M. Hoese, P. Reddy, A. Dietrich, M. K. Koch, K. G. Fehler, M. W. Doherty, and A. Kubanek, *Mechanical Decoupling of Quantum Emitters in Hexagonal Boron Nitride from Low-Energy Phonon Modes*, ArXiv 1 (2020).

[27] Y. Xia, Q. Li, J. Kim, W. Bao, C. Gong, S. Yang, Y. Wang, and X. Zhang, *Room-Temperature Giant Stark Effect of Single Photon Emitter in van Der Waals Material*, Nano Lett. **19**, 7100 (2019).

[28] G. Noh, D. Choi, J. Kim, D. Im, Y. Kim, H. Seo, and J. Lee, *Stark Tuning of Single-Photon Emitters in Hexagonal Boron Nitride*, Nano Lett. **18**, 4710 (2018).

[29] A. W. Elshaari, A. Skalli, S. Gyger, M. Nurizzo, L. Schweickert, I. Esmaeil Zadeh, M. Svedendahl, S. Steinhauer, and V. Zwiller, *Deterministic Integration of HBN Emitter in Silicon Nitride Photonic Waveguide*, Adv. Quantum Technol. **4**, 1 (2021).

[30] G. Moody, V. J. Sorger, P. W. Juodawlkis, W. Loh, C. Sorace-Agaskar, M. Davanco, L. Chang, J. E. Bowers, N. Quack, C. Galland, I. Aharonovich, M. A. Wolff, C. Schuck, N. Sinclair, M. Lončar, T. Komljenovic, D. Weld, S. Mookherjea, S. Buckley, M. Radulaski, S. Reitzenstein, B. Pingault, B. Machielse, D. Mukhopadhyay, A. Akimov, A. Zheltikov, G. S. Agarwal, K. Srinivasan, J. Lu, H. X. Tang, W. Jiang, T. P. McKenna, A. H. Safavi-Naeini, S. Steinhauer, A. W. Elshaari, V. Zwiller, P. S. Davids, N. Martinez, M. Gehl, J. Chiaverini, K. K. Mehta, J. Romero, N. B. Lingaraju, A. M. Weiner, D. Peace, R. Cernansky, M. Lobino, E. Diamanti, L. T. Vidarte, and R. M. Camacho, *Roadmap on Integrated Quantum Photonics*, J. Phys. Photonics **4**, 012501 (2021).

[31] H. J. Kimble, *The Quantum Internet*, Nature **453**, 1023 (2008).

[32] J. L. O'Brien, A. Furusawa, and J. Vučković, *Photonic Quantum Technologies*, Nat. Photonics **3**, 687 (2009).

[33] N. Somaschi, V. Giesz, L. De Santis, J. C. Loredo, M. P. Almeida, G. Hornecker, S. L. Portalupi, T. Grange, C. Antón, J. Demory, C. Gómez, I. Sagnes, N. D. Lanzillotti-Kimura, A. Lemaítre, A. Auffeves, A. G. White, L. Lanco, and P. Senellart, *Near-Optimal Single-Photon Sources in the Solid State*, Nat. Photonics **10**, 340 (2016).

[34] L. J. Rogers, K. D. Jahnke, M. H. Metsch, A. Sipahigil, J. M. Binder, T. Teraji, H. Sumiya, J. Isoya, M. D. Lukin, P. Hemmer, and F. Jelezko, *All-Optical Initialization, Readout, and Coherent Preparation of Single Silicon-Vacancy Spins in Diamond*, Phys. Rev. Lett. **113**, 1 (2014).

[35] M. D. Eisaman, J. Fan, A. Migdall, and S. V. Polyakov, *Single-Photon Sources and Detectors*, Rev. Sci. Instrum. **82**, 071101 (2011).

[36] I. Aharonovich, S. Castelletto, D. A. Simpson, C. H. Su, A. D. Greentree, and S. Prawer, *Diamond-Based Single-Photon Emitters*, Reports Prog. Phys. **74**, 076501 (2011).

[37] M. Holmes, S. Kako, K. Choi, M. Arita, and Y. Arakawa, *Spectral Diffusion and Its Influence on the Emission Linewidths of Site-Controlled GaN Nanowire Quantum Dots*, Phys. Rev. B **92**, 115447 (2015).

[38] E. Neu, C. Hepp, M. Hauschild, S. Gsell, M. Fischer, H. Sternschulte, D. Steinmüller-Nethl, M. Schreck, and C. Becher, *Low-Temperature Investigations of Single Silicon Vacancy Colour Centres in Diamond*, New J. Phys. **15**, 043005 (2013).

[39] I. Aharonovich, D. Englund, and M. Toth, *Solid-State Single-Photon Emitters*, Nat. Photonics **10**, 631 (2016).

[40] I. Aharonovich and M. Toth, *Quantum Emitters in Two Dimensions*, Science (80-.). **358**, 170 (2017).

[41] J. D. Caldwell, I. Aharonovich, G. Cassabois, J. H. Edgar, B. Gil, and D. N. Basov, *Photonics with Hexagonal Boron Nitride*, Nat. Rev. Mater. **4**, 552 (2019).

[42] L. J. Martínez, T. Pelini, V. Waselowski, J. R. Maze, B. Gil, G. Cassabois, and V. Jacques, *Efficient Single Photon Emission from a High-Purity Hexagonal Boron Nitride Crystal*, Phys. Rev. B **94**, 121405(R) (2016).

[43] A. L. Exarhos, D. A. Hopper, R. R. Grote, A. Alkauskas, and L. C. Bassett, *Optical Signatures of Quantum Emitters in Suspended Hexagonal Boron Nitride*, ACS Nano **11**, 3328 (2017).

[44] N. Chejanovsky, M. Rezai, F. Paolucci, Y. Kim, T. Rendler, W. Rouabeh, F. Fávaro De Oliveira, P. Herlinger, A. Denisenko, S. Yang, I. Gerhardt, A. Finkler, J. H. Smet, and J. Wrachtrup, *Structural Attributes and Photodynamics of Visible Spectrum Quantum Emitters in Hexagonal Boron Nitride*, Nano Lett. **16**, 7037 (2016).

[45] G. Grosso, H. Moon, B. Lienhard, S. Ali, D. K. Efetov, M. M. Furchi, P. Jarillo-Herrero, M. J. Ford, I. Aharonovich, and D. Englund, *Tunable and High-Purity Room Temperature Single-Photon Emission from Atomic Defects in Hexagonal Boron Nitride*, Nat. Commun. **8**, 705 (2017).

[46] F. Hayee, L. Yu, J. L. Zhang, C. J. Ciccarino, M. Nguyen, A. F. Marshall, I. Aharonovich, J. Vučković, P. Narang, T. F. Heinz, and J. A. Dionne, *Revealing Multiple Classes of Stable Quantum Emitters in Hexagonal Boron Nitride with Correlated Optical and Electron Microscopy*, Nat. Mater. **19**, 534 (2020).

[47] S. Choi, T. T. Tran, C. Elbadawi, C. Lobo, X. Wang, S. Juodkazis, G. Seniutinas, M. Toth, and I. Aharonovich, *Engineering and Localization of Quantum Emitters in Large Hexagonal Boron Nitride Layers*, ACS Appl. Mater. Interfaces **8**, 29642 (2016).

[48] Z. Xu, C. Elbadawi, T. T. Tran, M. Kianinia, X. Li, D. Liu, T. Hoffman, M. A. Nguyen, S. Kim, J. Edgar, X. Wu, L. Song, S. ALI, M. Ford, M. Toth, and igor aharonovich, *Single Photon Emission from Plasma Treated 2D Hexagonal Boron Nitride*, Nanoscale 7957 (2018).

[49] X. Li, G. D. Shepard, A. Cupo, N. Camporeale, K. Shayan, Y. Luo, V. Meunier, and S. Strauf, *Nonmagnetic Quantum Emitters in Boron Nitride with Ultranarrow and Sideband-Free Emission Spectra*, ACS Nano **11**, 6652 (2017).

[50] A. Gottscholl, M. Kianinia, V. Soltamov, S. Orlinskii, G. Mamin, C. Bradac, C. Kasper, K. Krambrock, A. Sperlich, M. Toth, I. Aharonovich, and V. Dyakonov, *Initialization and Read-out of Intrinsic Spin Defects in a van Der Waals Crystal at Room Temperature*, Nat. Mater. **19**, 540 (2020).

[51] J. Ziegler, R. Klaiss, A. Blaikie, D. Miller, V. R. Horowitz, and B. Alemán, *Deterministic Quantum Emitter Formation in Hexagonal Boron Nitride via Controlled Edge Creation*, Nano Lett. **19**, 2121 (2019).

[52] N. V. Proscia, Z. Shotan, H. Jayakumar, P. Reddy, C. Cohen, M. Dollar, A. Alkauskas, M. W. Doherty, C. A. Meriles, and V. M. Menon, *Near-Deterministic Activation of Room-Temperature Quantum Emitters in Hexagonal Boron Nitride*, Optica **5**, 1128 (2018).

[53] T. T. Tran, D. Wang, Z. Q. Xu, A. Yang, M. Toth, T. W. Odom, and I. Aharonovich, *Deterministic Coupling of Quantum Emitters in 2D Materials to Plasmonic Nanocavity Arrays*, Nano Lett. **17**, 2634 (2017).

[54] T. T. Tran, M. Kianinia, M. Nguyen, S. Kim, Z. Q. Xu, A. Kubanek, M. Toth, and I. Aharonovich, *Resonant Excitation of Quantum Emitters in Hexagonal Boron Nitride*, ACS Photonics **5**, 295 (2018).

[55] H. L. Stern, R. Wang, Y. Fan, R. Mizuta, J. C. Stewart, L. M. Needham, T. D. Roberts, R. Wai, N. S. Ginsberg, D. Klenerman, S. Hofmann, and S. F. Lee, *Spectrally Resolved Photodynamics of Individual Emitters in Large-Area Monolayers of Hexagonal Boron Nitride*, ACS Nano **13**, 4538 (2019).

[56] Z. Shotan, H. Jayakumar, C. R. Considine, M. Mackoit, H. Fedder, J. Wrachtrup, A. Alkauskas, M. W. Doherty, V. M. Menon, and C. A. Meriles, *Photoinduced Modification of Single-Photon Emitters in Hexagonal Boron Nitride*, ACS Photonics **3**, 2490 (2016).

[57] B. Spokoyny, H. Utzat, H. Moon, G. Grosso, D. Englund, and M. G. Bawendi, *Effect of Spectral Diffusion on the Coherence Properties of a Single Quantum Emitter in Hexagonal Boron Nitride*, J. Phys. Chem. Lett. 1330 (2020).

[58] J. Wolters, N. Sadzak, A. W. Schell, T. Schroder, and O. Benson, *Measurement of the Ultrafast Spectral Diffusion of the Optical Transition of Nitrogen Vacancy Centers in Nano-Size Diamond Using Correlation Interferometry*, Phys. Rev. Lett. **110**, 027401 (2013).

[59] A. Dietrich, M. Bürk, E. S. Steiger, L. Antoniuk, T. T. Tran, M. Nguyen, I. Aharonovich, F. Jelezko, and A. Kubanek, *Observation of Fourier Transform Limited Lines in Hexagonal Boron Nitride*, Phys. Rev. B **98**, 081414(R) (2018).

[60] B. Sontheimer, M. Braun, N. Nikolay, N. Sadzak, I. Aharonovich, and O. Benson, *Photodynamics of Quantum Emitters in Hexagonal Boron Nitride Revealed by Low-Temperature Spectroscopy*, Phys. Rev. B **96**, 121202(R) (2017).

[61] S. V. Novoselov, K. S. Geim, A. K. Morozov, S. V. Jiang, D. Zhang, Y. Dubonos, I. V. Grigorieva, and A. A. Firsov, *Electric Field Effect in Atomically Thin Carbon Films*, Science (80-.). **306**, 666 (2004).

[62] X. F. Fan, W. T. Zheng, V. Chihaia, Z. X. Shen, and J. Kuo, *Interaction between Graphene and the Surface of Interaction between Graphene and the Surface of SiO 2*, J. Phys. Condens. Matter **24**, 305004 (2012).

[63] A. Sipahigil, K. D. Jahnke, L. J. Rogers, T. Teraji, J. Isoya, A. S. Zibrov, F. Jelezko, and M. D. Lukin, *Indistinguishable Photons from Separated Silicon-Vacancy Centers in Diamond*, Phys. Rev. Lett. **113**, 113602 (2014).

[64] W. H. Lin, V. W. Brar, D. Jariwala, M. C. Sherrott, W. S. Tseng, C. I. Wu, N. C. Yeh, and H. A. Atwater, *Atomic-Scale Structural and Chemical Characterization of Hexagonal Boron Nitride Layers Synthesized at the Wafer-Scale with Monolayer Thickness Control*, Chem. Mater. **29**, 4700 (2017).

[65] A. A. Maradudin, *Theoretical and Experimental Aspects of the Effects of Point Defects and Disorder on the Vibrations of Crystals*, Solid State Phys. **49**, (1968).

[66] V. Hizhnyakov, H. Kaasik, and I. Sildos, *Zero-Phonon Lines: The Effect of a Strong Softening of Elastic Springs in the Excited State*, Phys. Status Solidi Basic Res. **234**, 644 (2002).

[67] N. R. Jungwirth, B. Calderon, Y. Ji, M. G. Spencer, M. E. Flatté, and G. D. Fuchs, *Temperature Dependence of Wavelength Selectable Zero-Phonon Emission from Single Defects in Hexagonal Boron Nitride*, Nano Lett. **16**, 6052 (2016).

[68] D. Wigger, R. Schmidt, O. Del Pozo-Zamudio, J. A. Preuß, P. Tonndorf, R. Schneider, P. Steeger, J. Kern, Y. Khodaei, J. Sperling, S. M. De Vasconcellos, R. Bratschitsch, and T. Kuhn, *Phonon-Assisted Emission and Absorption of Individual Color Centers in Hexagonal Boron Nitride*, 2D Mater. **6**, 035006 (2019).

[69] F. Cadiz, E. Courtade, C. Robert, G. Wang, Y. Shen, H. Cai, T. Taniguchi, K. Watanabe, H. Carrere, D. Lagarde, M. Manca, T. Amand, P. Renucci, S. Tongay, X. Marie, and B. Urbaszek, *Excitonic Linewidth Approaching the Homogeneous Limit in MoS2-Based van Der Waals Heterostructures*, Phys. Rev. X **7**, 021026 (2017).

[70] P. Dey, J. Paul, Z. Wang, C. E. Stevens, C. Liu, A. H. Romero, J. Shan, D. J. Hilton, and D. Karaiskaj, *Optical Coherence in Atomic-Monolayer Transition-Metal Dichalcogenides Limited by Electron-Phonon Interactions*, Phys. Rev. Lett. **116**, 127402 (2016).

[71] L. Vina, S. I. Ogothetidis, and M. Cardona, *Temperature Dependence of the Dielectric Function of Germanium*, Phys. Rev. B **30**, 1979 (1984).

[72] H. Y. Chen, D. Sangalli, and M. Bernardi, *Exciton-Phonon Interaction and Relaxation Times from First Principles*, Phys. Rev. Lett. **125**, 107401 (2020).

[73] J. H. Crawford and L. M. Slifkin, *Point Defects in Solids* (Springer, New York, NY, 1972).

[74] M. A. Nielsen and I. L. Chuang, *Quantum Computation and Quantum Information* (Cambridge University Press, Cambridge, 2010).

[75] J. R. Weber, W. F. Koehl, J. B. Varley, A. Janotti, B. B. Buckley, C. G. Van De Walle, and D. D. Awschalom, *Quantum Computing with Defects*, Proc. Natl. Acad. Sci. U. S. A. **107**, 8513 (2010).

[76] A. Beveratos, R. Brouri, T. Gacoin, A. Villing, J. P. Poizat, and P. Grangier, *Single Photon Quantum Cryptography*, Phys. Rev. Lett. **89**, 4 (2002).

[77] M. W. Doherty, N. B. Manson, P. Delaney, F. Jelezko, J. Wrachtrup, and L. C. L. Hollenberg, *The Nitrogen-Vacancy Colour Centre in Diamond,* Phys. Rep. **528**, 1 (2013).

[78] D. D. Awschalom, R. Hanson, J. Wrachtrup, and B. B. Zhou, *Quantum Technologies with Optically Interfaced Solid-State Spins*, Nat. Photonics **12**, 516 (2018).

[79] S. Kako, C. Santori, K. Hoshino, S. Götzinger, Y. Yamamoto, and Y. Arakawa, *A Gallium Nitride Single-Photon Source Operating at 200K*, Nat. Mater. **5**, 887 (2006).

[80] A. J. Morfa, B. C. Gibson, M. Karg, T. J. Karle, A. D. Greentree, P. Mulvaney, and S. Tomljenovic-Hanic, *Single-Photon Emission and Quantum Characterization of Zinc Oxide Defects*, Nano Lett. **12**, 949 (2012).

[81] M. Atatüre, D. Englund, N. Vamivakas, S. Y. Lee, and J. Wrachtrup, *Material Platforms for Spin-Based Photonic Quantum Technologies*, Nat. Rev. Mater. **3**, 38 (2018).

[82] A. Srivastava, M. Sidler, A. V. Allain, D. S. Lembke, A. Kis, and A. Imamoglu, *Optically Active Quantum Dots in Monolayer WSe2*, Nat. Nanotechnol. **10**, 491 (2015).

[83] Y. M. He, G. Clark, J. R. Schaibley, Y. He, M. C. Chen, Y. J. Wei, X. Ding, Q. Zhang, W. Yao, X. Xu, C. Y. Lu, and J. W. Pan, *Single Quantum Emitters in Monolayer Semiconductors*, Nat. Nanotechnol. **10**, 497 (2015).

[84] M. Koperski, K. Nogajewski, A. Arora, V. Cherkez, P. Mallet, J. Y. Veuillen, J. Marcus, P. Kossacki, and M. Potemski, *Single Photon Emitters in Exfoliated WSe2structures*, Nat. Nanotechnol. **10**, 503 (2015).

[85] C. Chakraborty, L. Kinnischtzke, K. M. Goodfellow, R. Beams, and A. N. Vamivakas, *Voltage-Controlled Quantum Light from an Atomically Thin Semiconductor*, Nat. Nanotechnol. **10**, 507 (2015).

[86] P. Tonndorf, R. Schmidt, R. Schneider, J. Kern, M. Buscema, G. A. Steele, A. Castellanos-Gomez, H. S. J. van der Zant, S. Michaelis de Vasconcellos, and R. Bratschitsch, *Single-Photon Emission from Localized Excitons in an Atomically Thin Semiconductor*, Optica **2**, 347 (2015).

[87] A. L. Exarhos, D. A. Hopper, R. N. Patel, M. W. Doherty, and L. C. Bassett, *Magnetic-Field-Dependent Quantum Emission in Hexagonal Boron Nitride at Room Temperature*, Nat. Commun. **10**, 1 (2019).

[88] H. Akbari, W. H. Lin, B. Vest, P. K. Jha, and H. A. Atwater, *Temperature-Dependent Spectral Emission of Hexagonal Boron Nitride Quantum Emitters on Conductive and Dielectric Substrates*, Phys. Rev. Appl. **15**, 1 (2021).

[89] K. Kang, K. H. Lee, Y. Han, H. Gao, S. Xie, D. A. Muller, and J. Park, *Layer-by-Layer Assembly of Two-Dimensional Materials into Wafer-Scale Heterostructures*, Nature **550**, 229 (2017).

[90] C. M. Went, J. Wong, P. R. Jahelka, M. Kelzenberg, S. Biswas, M. S. Hunt, A. Carbone, and H. A. Atwater, *A New Metal Transfer Process for van Der Waals Contacts to Vertical Schottky-Junction Transition Metal Dichalcogenide Photovoltaics*, Sci. Adv. **5**, (2019).

[91] J. Cai, A. Retzker, F. Jelezko, and M. B. Plenio, *A Large-Scale Quantum Simulator on a Diamond Surface at Room Temperature*, Nat. Phys. **9**, 168 (2013).

[92] S. Wehner, D. Elkouss, and R. Hanson, *Quantum Internet: A Vision for the Road Ahead*, Science (80-.). **362**, (2018).

[93] W. L. Barnes, S. A. R. Horsley, and W. L. Vos, *Classical Antennas, Quantum Emitters, and Densities of Optical States*, J. Opt. (United Kingdom) **22**, (2020).

[94] P. K. Jha, M. Mrejen, J. Kim, C. Wu, Y. Wang, Y. V. Rostovtsev, and X. Zhang, *Coherence-Driven Topological Transition in Quantum Metamaterials*, Phys. Rev. Lett. **116**, 1 (2016).

[95] M. Nalabothula, P. K. Jha, T. Low, and A. Kumar, *Engineering Valley Quantum Interference in Anisotropic van Der Waals Heterostructures*, Phys. Rev. B **102**, 1 (2020).

[96] A. Ghosh, A. Sharma, A. I. Chizhik, S. Isbaner, D. Ruhlandt, R. Tsukanov, I. Gregor, N. Karedla, and J. Enderlein, *Graphene-Based Metal-Induced Energy Transfer for Sub-Nanometre Optical Localization*, Nat. Photonics **13**, 860 (2019).

[97] M. M. Qazilbash, M. Brehm, B.-G. Chae, P.-C. Ho, G. O. Andreev, B.-J. Kim, S. J. Yun, A. V Balatsky, M. B. Maple, F. Keilmann, H.-T. Kim, and D. N. Basov, *Mott Transition in VO2 Revealed by Infrared Spectroscopy and Nano-Imaging*, Science (80-.). **318**, 1750 (2007).

[98] N. Nikolay, N. Mendelson, E. Özelci, B. Sontheimer, F. Bohm, G. Kewes, M. Toth, I. Aharonovich, and O. Benson, *Direct Measurement of Quantum Efficiency of Single-Photon Emitters in Hexagonal Boron Nitride*, Optica **6**, 1084 (2019).

[99] Y. Kim, P. C. Wu, R. Sokhoyan, K. Mauser, R. Glaudell, G. Kafaie Shirmanesh, and H. A. Atwater, *Phase Modulation with Electrically Tunable Vanadium Dioxide Phase-Change Metasurfaces*, Nano Lett. **19**, 3961 (2019).

[100] E. Wu, V. Jacques, H. Zeng, P. Grangier, F. Treussart, and J.-F. Roch, *Narrow-Band Single-Photon Emission in the near Infrared for Quantum Key Distribution*, Opt. Express **14**, 1296 (2006).

[101] M. K. Boll, I. P. Radko, A. Huck, and U. L. Andersen, *Photophysics of Quantum Emitters in Hexagonal Boron-Nitride Nano-Flakes*, Opt. Express **28**, 7475 (2020).

[102] C. Lethiec, J. Laverdant, H. Vallon, C. Javaux, B. Dubertret, J. M. Frigerio, C. Schwob, L. Coolen, and A. Maître, *Measurement of Three-Dimensional Dipole Orientation of a Single Fluorescent Nanoemitter by Emission Polarization Analysis*, Phys. Rev. X **4**, 1 (2014).

[103] P. K. Jha, X. Ni, C. Wu, Y. Wang, and X. Zhang, *Metasurface-Enabled Remote Quantum Interference*, Phys. Rev. Lett. **115**, 1 (2015).

[104] P. K. Jha, N. Shitrit, J. Kim, X. Ren, Y. Wang, and X. Zhang, *Metasurface-Mediated Quantum Entanglement,* ACS Photonics **5**, 971 (2018).

[105] P. K. Jha, N. Shitrit, X. Ren, Y. Wang, and X. Zhang, *Spontaneous Exciton Valley Coherence in Transition Metal Dichalcogenide Monolayers Interfaced with an Anisotropic Metasurface*, Phys. Rev. Lett. **121**, 116102 (2018).

[106] X. Ren, P. K. Jha, Y. Wang, and X. Zhang, *Nonconventional Metasurfaces: From Non-Hermitian Coupling, Quantum Interactions, to Skin Cloak*, Nanophotonics **7**, 1233 (2018).

[107] T. Vogl, G. Campbell, B. C. Buchler, Y. Lu, and P. K. Lam, *Fabrication and Deterministic Transfer of High-Quality Quantum Emitters in Hexagonal Boron Nitride*, ACS Photonics **5**, 2305 (2018).

[108] F. Pizzocchero, L. Gammelgaard, B. S. Jessen, J. M. Caridad, L. Wang, J. Hone, P. Bøggild, and T. J. Booth, *The Hot Pick-up Technique for Batch Assembly of van Der Waals Heterostructures*, Nat. Commun. **7**, (2016).

[109] D. G. Purdie, N. M. Pugno, T. Taniguchi, K. Watanabe, A. C. Ferrari, and A. Lombardo, *Cleaning Interfaces in Layered Materials Heterostructures*, Nat. Commun. **9**, 1 (2018).

[110] N. Kharche and S. K. Nayak, *Quasiparticle Band Gap Engineering of Graphene and Graphone on Hexagonal Boron Nitride Substrate*, Nano Lett. **11**, 5274 (2011).

[111] C. R. Dean, A. F. Young, I. Meric, C. Lee, L. Wang, S. Sorgenfrei, K. Watanabe, T. Taniguchi, P. Kim, K. L. Shepard, and J. Hone, *Boron Nitride Substrates for High-Quality Graphene Electronics*, Nat. Nanotechnol. **5**, 722 (2010).

[112] T. T. Tran, C. Zachreson, A. M. Berhane, K. Bray, R. G. Sandstrom, L. H. Li, T. Taniguchi, K. Watanabe, I. Aharonovich, and M. Toth, *Quantum Emission from Defects in Single-Crystalline Hexagonal Boron Nitride*, Phys. Rev. Appl. **5**, 2 (2016).

[113] A. L. Exarhos, D. A. Hopper, R. R. Grote, A. Alkauskas, and L. C. Bassett, *Optical Signatures of Quantum Emitters in Suspended Hexagonal Boron Nitride*, ACS Nano **11**, 3328 (2017).

[114] M. Hoese, P. Reddy, A. Dietrich, M. K. Koch, K. G. Fehler, M. W. Doherty, and A. Kubanek, *Mechanical Decoupling of Quantum Emitters in Hexagonal Boron Nitride from Low-Energy Phonon Modes*, Sci. Adv. **6**, 1 (2020).

[115] A. Gottscholl, M. Diez, V. Soltamov, C. Kasper, D. Krauße, A. Sperlich, M. Kianinia, C. Bradac, I. Aharonovich, and V. Dyakonov, *Spin Defects in HBN as Promising Temperature, Pressure and Magnetic Field Quantum Sensors*, Nat. Commun. **12**, 6 (2021).

[116] H. L. Stern, Q. Gu, J. Jarman, S. Eizagirre Barker, N. Mendelson, D. Chugh, S. Schott, H. H. Tan, H. Sirringhaus, I. Aharonovich, and M. Atatüre, *Room-Temperature Optically Detected Magnetic Resonance of Single Defects in Hexagonal Boron Nitride*, Nat. Commun. **13**, 1 (2022).

[117] S. White, C. Stewart, A. S. Solntsev, C. Li, M. Toth, M. Kianinia, and I. Aharonovich, *Phonon Dephasing and Spectral Diffusion of Quantum Emitters in Hexagonal Boron Nitride*, Optica **8**, (2021).

[118] T. T. Tran, C. Bradac, A. S. Solntsev, M. Toth, and I. Aharonovich, *Suppression of Spectral Diffusion by Anti-Stokes Excitation of Quantum Emitters in Hexagonal Boron Nitride*, Appl. Phys. Lett. **115**, (2019).

[119] S. J. U. White, T. Yang, N. Dontschuk, C. Li, Z.-Q. Xu, M. Kianinia, A. Stacey, M. Toth, and I. Aharonovich, *Electrical Control of Quantum Emitters in a Van Der Waals Heterostructure*, ArXiv:2111.02754 (2021).

[120] M. Yu, D. Yim, H. Seo, and J. Lee, *Electrical Charge Control of h -BN Single Photon Sources*, ArXiv:2202.09037 (2022).

[121] P. K. Jha, H. Akbari, Y. Kim, S. Biswas, and H. A. Atwater, *Nanoscale Axial Position and Orientation Measurement of Hexagonal Boron Nitride Quantum Emitters Using a Tunable Nanophotonic Environment*, Nanotechnology **33**, (2022).

[122] V. Hizhnyakov and P. Reineker, *Optical Dephasing in Defect-Rich Crystals*, J. Chem. Phys. **111**, 8131 (1999).

[123] H. Akbari, S. Biswas, P. K. Jha, J. Wong, B. Vest, and H. A. Atwater, *Lifetime-Limited and Tunable Quantum Light Emission in h-BN via Electric Field Modulation*, Nano Lett. **22**, 7798 (2022).

[124] L. Mandel, *Sub-Poissonian Photon Statistics in Resonance Fluorescence*, Opt. Lett. **4**, 205 (1979).

[125] C. K. Hong, Z. Y. Ou, and L. Mandel, *Measurement of Subpicosecond Time Intervals between Two Photons by Interference*, Phys. Rev. Lett. **59**, (1987).

[126] R. Alléaume, F. Treussart, J. M. Courty, and J. F. Roch, *Photon Statistics Characterization of a Single-Photon Source*, New J. Phys. **6**, 1 (2004).

[127] F. Treussart, R. Alléaume, V. Le Floc'h, L. T. Xiao, J. M. Courty, and J. F. Roch, *Direct Measurement of the Photon Statistics of a Triggered Single Photon Source*, Phys. Rev. Lett. **89**, 2 (2002).

[128] C. Jones, J. Xavier, S. Vartabi Kashanian, M. Nguyen, I. Aharonovich, and F. Vollmer, *Time-Dependent Mandel Q Parameter Analysis for a Hexagonal Boron Nitride Single Photon Source*, Opt. Express **31**, 10794 (2023).

[129] N. R. Jungwirth and G. D. Fuchs, *Optical Absorption and Emission Mechanisms of Single Defects in Hexagonal Boron Nitride*, Phys. Rev. Lett. **119**, 1 (2017).

[130] S. J. U. White, F. Klauck, T. Trong Tran, N. Schmitt, M. Kianinia, A. Steinfurth, M. Heinrich, M. Toth, A. Szameit, I. Aharonovich, and A. S. Solntsev, *Quantum Random Number Generation Using a Hexagonal Boron Nitride Single Photon Emitter*, J. Opt. (United Kingdom) **23**, (2021).

[131] M. Hoese, M. K. Koch, F. Breuning, N. Lettner, K. G. Fehler, and A. Kubanek, *Single Photon Randomness Originating from the Symmetric Dipole Emission Pattern of Quantum Emitters*, Appl. Phys. Lett. **120**, (2022).

[132] L. E. Bassham, A. Rukhin, J. Soto, J. Nechvatal, M. Smid, E. Barker, S. Leigh, M. Levenson, M. Vangel, D. Banks, A. Heckert, J. Dray, and S. Vo, *A Statistical Test Suite for Random and Pseudorandom Number Generators for Cryptographic Applications*, NIST Spec. Publ. **800**, (2010).

[133] B. Schaefer, E. Collett, R. Smyth, D. Barrett, and B. Fraher, *Measuring the Stokes Polarization Parameters*, Am. J. Phys. **75**, 163 (2007).

[134] F. Yang, P. K. Jha, H. Akbari, H. C. Bauser, and H. A. Atwater, *A Hybrid Coupler for Directing Quantum Light Emission with High Radiative Purcell Enhancement to a Dielectric Metasurface Lens*, J. Appl. Phys. **130**, (2021).

[135] C. G. Parazzoli, B. A. Capron, B. Koltenbah, D. Gerwe, P. Idell, J. Dowling, C. Gerry, and R. W. Boyd, *Enhanced Thermal Images of Faint Objects via Photon Addition / Subtraction*, 2016 Conf. Lasers Electro-Optics, CLEO 2016 2 (2016).

Appendices

Appendix A: Efforts on TEM imaging of h-BN defects

In the course of my PhD, we tried to perform an atomic resolution transmission electron microscopy (TEM) on h-BN emitters to determine their atomic structure. This project had several fabrication and measurement challenges and at the end we could not successfully image a defect. Here I explain some of our efforts on this project. For this project we needed the h-BN to be atomically thin for an ideal defect imaging (1-3 atomic layers thick) we soon realized that the emitters hosted in the atomically thin h-BN samples exhibit very unstable and faint emission and are prone to bleaching. After identifying samples with the right thickness that showed the emission, we also tried multiple choices for the TEM grid and the results are shown below.

We started by using CVD grown h-BN and performed a wet transfer technique to transfer the h-BN onto a holey carbon TEM grid (QUANTIFOIL). We performed PL spectroscopy on the sample, and we realized that the carbon-based TEM grid also exhibits a wide luminescence signature. In the TEM spectroscopy we noticed that the sample is too thick for the atomic resolution. As a result, we decided to work with exfoliated samples and moved on to other TEM grids based on SiN.

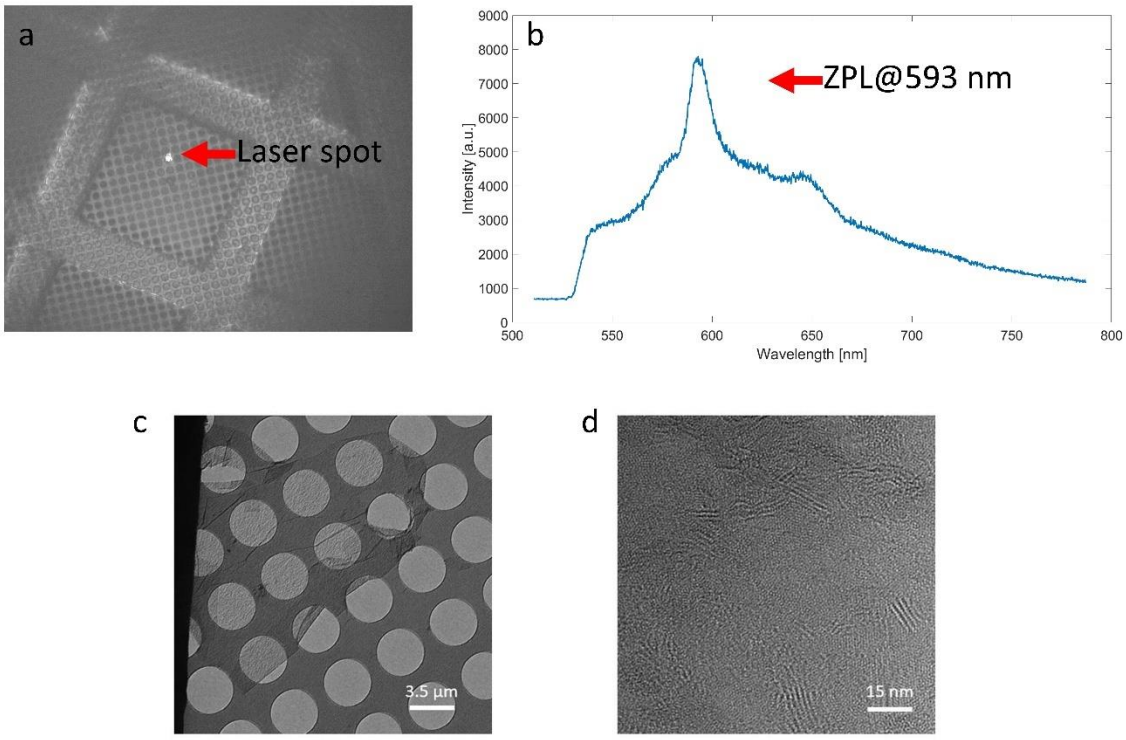

Figure A. 1. The result of the experiment with CVD h-BN on the holey carbon TEM grid. (a) Shows an optical microscope image of the sample. (b) PL spectra of the emitter identified in the sample. The wide background is due to the luminescence from the grid. (c-d) TEM microscope image of the sample.

We needed to develop a new transfer technique to transfer exfoliated h-BN onto the TEM grids and we tried two different methods. In the first method we exfoliated the h-BN onto a SiO_2-Si substrate and then picked up the h-BN with a Polycarbonate (PC) on PDMS. Then the h-BN was transferred onto the grid and the PDMS was removed and finally the PC was dissolved in a solvent. In the second method we exfoliated directly onto the PDMS substrate and then transferred the flake onto a TEM grid. The second method yielded more pristine samples due to being a fully dry method.

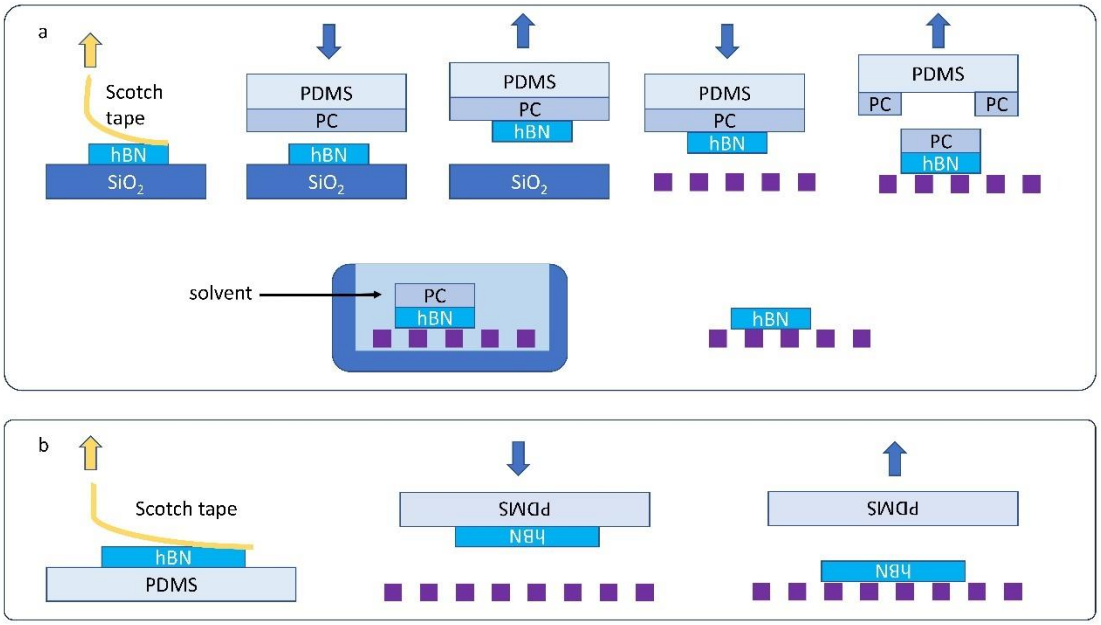

Figure A. 2. Schematic of the two transfer techniques we used to transfer h-BN flakes onto the TEM grids.

We also shifted towards a single hole SiN TEM grid (Norcada) due to better transfer yield. After the transfer we were able to collect cathodoluminescence signal with a peak around 700nm However we were not able to perform atomic resolution images. Our hypothesis as for why we could not perform the microscopy is that the electron beam with the energy required to perform the imaging is too high and destroys the crystal structure around the focused electron beam.

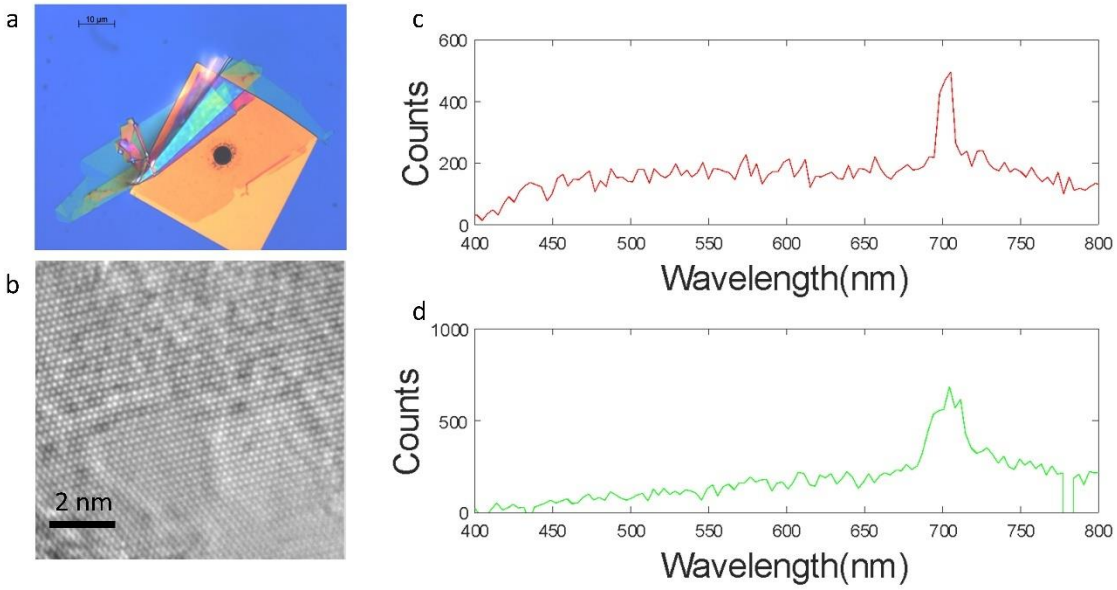

Figure A. 3. TEM microscopy of h-BN. (a) Microscope image of the sample. (b) Wide TEM image of the h-BN crystal. (c-d) the CL signal form the sample.

To gain some insight into the atomic structure of the defects we performed energy dispersive X-ray spectroscopy (EDS) on our samples, and we could find traces of silicon and oxygen atoms in our samples.

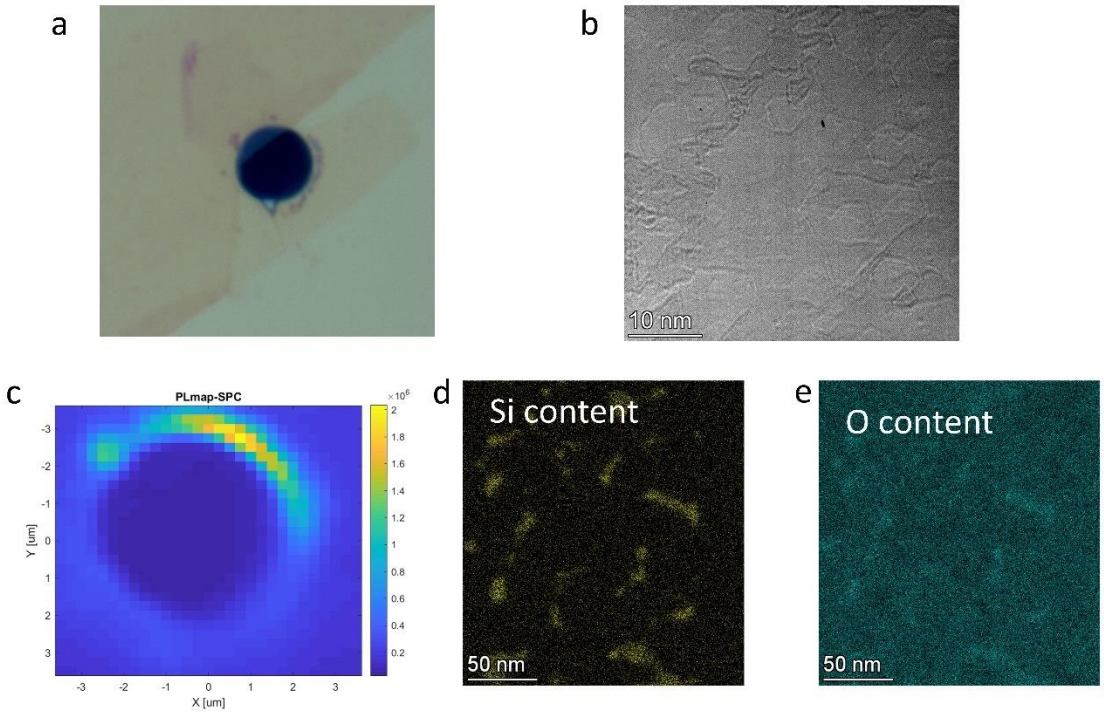

Figure A. 4. Result of EDS measurement on the h-BN samples. (a) Microscope image of the sample. (b) TEM image of the sample. (c) PL spectroscopy result. (d) EDS result showing silicon content. (e) EDS result showing oxygen content.

We also performed electron energy loss spectroscopy and identified carbon to be present in our samples. We expected carbon as we used carbon-adjacent annealing as a method to induce defect in our h-BN samples.

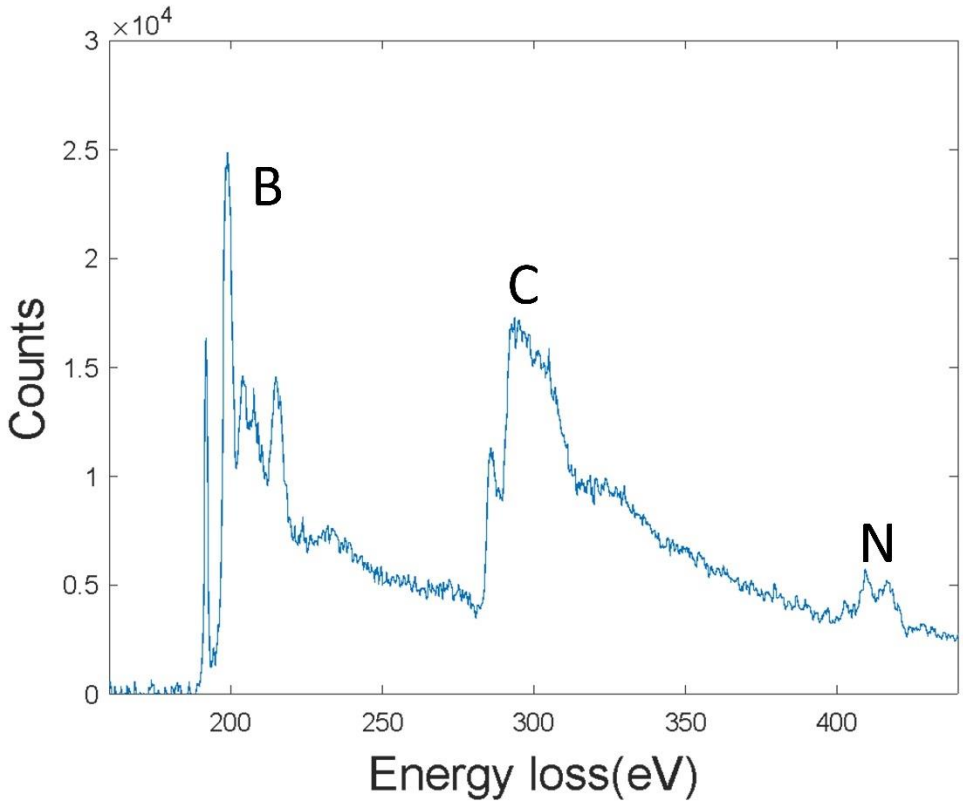

Figure A. 5. EELS spectroscopy identifies boron, nitrogen and carbon in our h-BN sample.

Appendix B: Polarization and dipole orientation analysis

We developed a code to extract the out-of-plane dipole component of emitter dipoles based on the result of polarization measurement. In this analysis we assume our emitter is a perfect dipole, emitting light in a dipole pattern, and based on the objective lens's numerical aperture (NA) we can estimate whether the dipole is oriented exactly in the plane normal to the objective lens's axis or it has angle θ with respect to the axis of the objective lens. Here we explain our method and provide the code used for this analysis.

The method is based on the concepts of ray optics combined with polarization vector. Here we assume the objective lens to effectively act as a flat lens located exactly one focal length away from the emitter, that converts each beam directed at it to a beam normal to the lens and maintains the polarization based on the Snell's law of diffraction. Then the beam enters a linear polarizer and the component of polarization aligned with the polarizer is passing through the polarizer and the rest of the light is absorbed. We assume the extinction ratio of the polarizer to be infinity. (In reality the extinction ratio is on the order of 10000) then the amplitude of the final beam is converted to intensity and the output intensity is calculated and integrated over the cross section of the beam. The schematic of this method is depicted in Figure B. 1.

Finally, we calculate the visibility based on the dipole polarization pattern:

$$visibility = \frac{\max(Intensity) - \min\,(Intensity)}{\max(Intensity) + \min\,(Intensity)}.$$

For an in-plane dipole this value should approach 1, and for a completely out-of-plane dipole this value should approach zero.

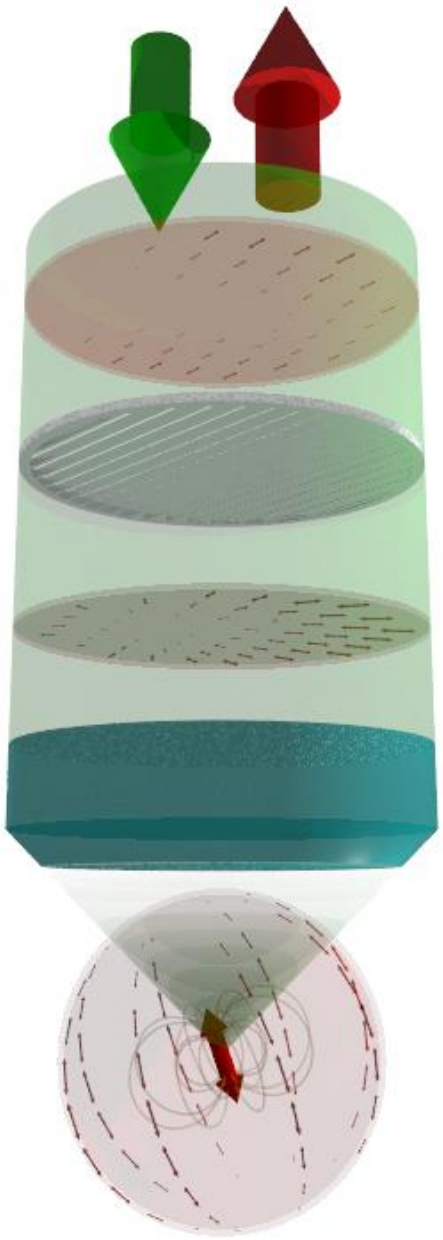

Figure B. 1. Schematic of the experimental setup. Here the dipole emission pattern, the transformation done by the objective lens, and the transformation done by the linear polarizer is shown.

The result of this simulation is demonstrated in the following figures.

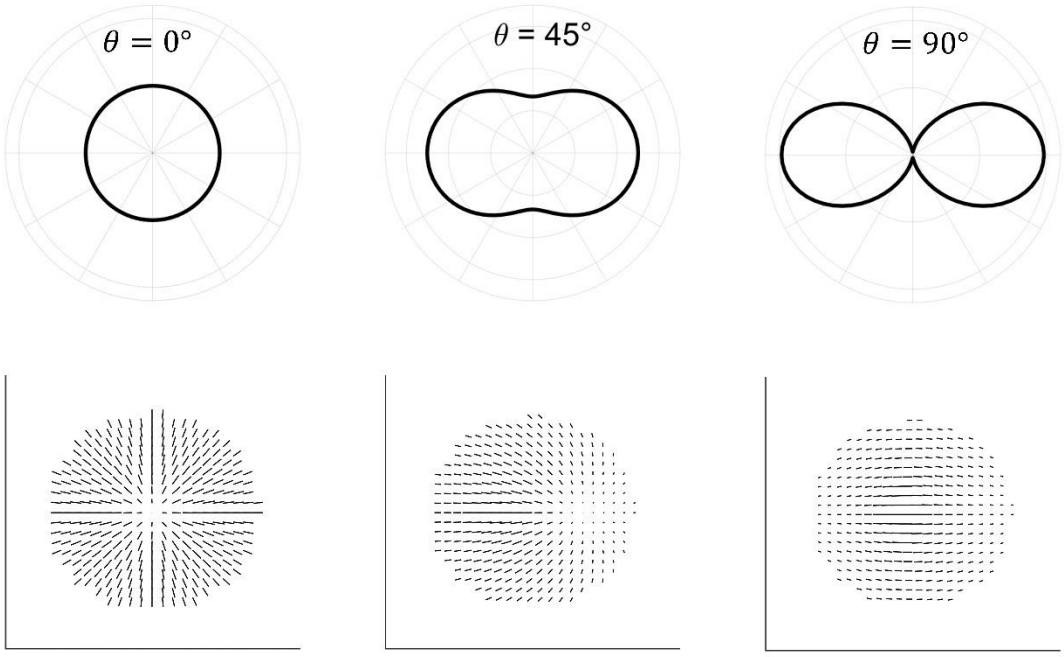

Figure B. 2. Some examples of our simulation. Top row shows the result of polarization measurement by rotating the linear polarizer, and the Bottom row shows the polarization of the electric field at the cross section of the beam.

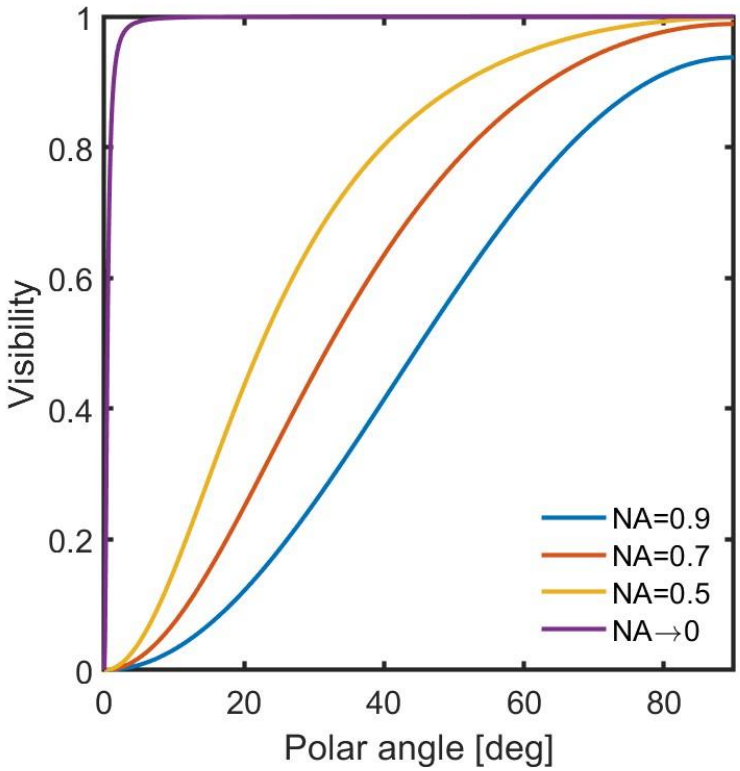

Figure B. 3. The visibility of the polarization as a function of angle (θ) for different values of the numerical aperture.

The MATLAB code is also provided:

The code consists of two parts, we have a function `VisOfPol(theta,NA)` which returns the visibility as a function of θ and the NA, this function is as follows:

```
function f=VisOfPol(angle,NA)

tt0=asin(NA);
RR=tan(tt0);
theta0=angle*(pi/180);
N=100;
R=RR/(2*N):RR/N:RR-RR/(2*N);
```

```
beta=(2*pi)/(2*N):2*pi/N:2*pi-(2*pi)/(2*N);
xx=zeros(N,N);
yy=zeros(N,N);

dR=RR/N;
dbeta=2*pi/N;

dA=zeros(N,N);
EEx=zeros(N,N);
EEy=zeros(N,N);
for i=1:N
    for j=1:N

        z0=1;
        x0=R(i)*cos(beta(j));
        y0=R(i)*sin(beta(j));
        r0=[x0 y0 z0];
        xx(i,j)=x0;
        yy(i,j)=y0;
        if sqrt(x0^2+y0^2)<RR

            absr0=sqrt((x0)^2+(y0)^2+(z0)^2);
            dA(i,j)=sqrt((x0)^2+(y0)^2)*dR*dbeta;
            theta=acos(z0/(sqrt(x0^2+y0^2+z0^2)));
            if y0>0
                phi=acos(x0/sqrt(x0^2+y0^2));
            else
                phi=2*pi-1*acos(x0/sqrt(x0^2+y0^2));
            end
            phat=[sin(theta0) 0 cos(theta0)];
            ttt1=cross(r0,cross(r0,phat));

tt1=ttt1/sqrt((ttt1(1))^2+(ttt1(2))^2+(ttt1(3))^2);
            rhat=r0/absr0;
            theta00=acos(dot(rhat,phat));
            E=(sin(theta00)/absr0)*tt1;

            Ex=E(1); Ey=E(2); Ez=E(3);

            absE=sqrt(Ex^2+Ey^2+Ez^2);
```

```
            zhat=[0 0 1];

tthat=cross(r0,zhat);that=tthat/sqrt(tthat(1)^2+tthat(2)^2+
tthat(3)^2);
            E1=dot(E,that);
            E2=dot(E,cross(rhat,that));
            E11=E1*that;
            E22=E2*cross(zhat,that);
            EE=(E11+E22)*dA(i,j);
            EEx(i,j)=EE(1);
            EEy(i,j)=EE(2);
        else
            EEx(i,j)=0;
            EEy(i,j)=0;
            dA(i,j)=0;
        end
    end
end

alpha=0:2*pi/100:2*pi;
pol=zeros(1,101);
for i=1:101
    Eproj=0;
    for j=1:N
        for k=1:N

Eproj=Eproj+(EEy(j,k)*sin(alpha(i))+EEx(j,k)*cos(alpha(i)))
^2;
        end
    end
    pol(i)=Eproj;
end

xxx=zeros(20,20);
yyy=zeros(20,20);
EEEx=zeros(20,20);
EEEu=zeros(20,20);
```

```
for i=1:N
    for j=1:N
        I=mod(i,N/20);
        J=mod(j,N/20);
        if I==0
            if J==0
                xxx(i/(N/20),j/(N/20))=xx(i,j);
                yyy(i/(N/20),j/(N/20))=yy(i,j);
                EEEx(i/(N/20),j/(N/20))=EEx(i,j);
                EEEy(i/(N/20),j/(N/20))=EEy(i,j);
            end
        end
    end
end
f=(max(pol)-min(pol))/(max(pol)+min(pol));
```

Then the other part of the code is written to set the value of NA and sweep different orientations of dipole (by changing θ) and plots visibility as a function of θ:

```
theta=0:0.1:90;
NA=0.6;
vis=zeros(1,max(size(theta)));
for i=1:max(size(theta))
    vis(i)=VisOfPol(theta(i),NA);
end


figure(1)
plot(theta,vis,'linewidth',2)
xlim([0,90])
ylim([0,1])
ylabel('Visibility','Fontsize',20)
xlabel('Polar angle [deg]','Fontsize',20)
%yticks([])
set(gca,'FontSize',20)
box on
ax = gca;
ax.LineWidth=2;
```

```
x0=10;
y0=10;
width=500;
height=500;
set(gcf,'position',[x0,y0,width,height])
```